



UNIVERSITÀ
DEGLI STUDI
FIRENZE

DOCTORAL PROGRAMME IN INDUSTRIAL
ENGINEERING
DOTTORATO DI RICERCA IN INGEGNERIA
INDUSTRIALE

XXX

**Analysis and optimization of hybrid
WAAM-milling process**

ING/IND-16

Doctoral Candidate

Filippo Montevacchi

Supervisors

Dott. Ing. Gianni Campatelli

Dott. Ing. Antonio Scippa

External Referees

Prof. Hiroyuki Sasahara

Prof. Michele Lanzetta

Dean of the Doctoral Programme

Prof. Maurizio De Lucia

Years 2014/2017

© Università degli Studi di Firenze – School of Engineering
Via di Santa Marta, 3, 50139 Firenze, Italy

Tutti i diritti riservati. Nessuna parte del testo può essere riprodotta o trasmessa in qualsiasi forma o con qualsiasi mezzo, elettronico o meccanico, incluso le fotocopie, la trasmissione fac simile, la registrazione, il riadattamento o l'uso di qualsiasi sistema di immagazzinamento e recupero di informazioni, senza il permesso scritto dell'editore.

All rights reserved. No part of the publication may be reproduced in any form by print, photoprint, microfilm, electronic or any other means without written permission from the publisher.

To my girlfriend, my friends, my family and my tutors.

Summary

The hybrid additive-subtractive manufacturing processes combine the advantages provided by the metal additive manufacturing with the high accuracy of the machining processes. Among these technologies the combination of WAAM (Wire-Arc-Additive-Manufacturing) and milling is an attractive option. The WAAM process is a metal additive manufacturing technology that uses arc welding to create metal components. It provides a high deposition rate and enables to manufacture large components. It requires a reduced investment compared laser based technologies both in terms of installation and operation. Moreover, WAAM operations can be performed on existing machine tools by a simple retrofitting to provide them arc welding capability.

Despite its advantages, the hybrid WAAM-milling process has several drawbacks which limit its diffusion among the manufacturing companies. The goal of the Ph.D. work presented in this thesis is to analyze such criticalities, proposing solutions to overcome or mitigate the process issues. Since the considered technology is a hybrid process, the overall performance depends on both the involved technologies. Hence, part of this thesis is strictly related to the WAAM process, while a further one is related to the milling of WAAM manufactured parts.

For what concerns the WAAM process, this thesis is focused on the thermal issues induced by the arc welding. The heat input of the process can cause large distortions, residual stresses and even lead to the structural collapse of the workpiece. This thesis pinpoints the process simulation as an efficient and effective approach to overcome the WAAM thermal issues. The current simulation techniques are analyzed, proposing improvements that aim at increasing the simulation time efficiency without losing accuracy. The proposed modelling techniques are validated comparing simulations with the actual process, both in terms of temperature field and workpiece distortions, confirming their accuracy. The proposed simulation techniques are applied to tackle the heat accumulation issues, responsible for the structural collapse of WAAM workpieces. To overcome this issue, two different approaches are proposed: i) an innovative cooling system, developed by using the proposed simulation technique ii) a simulation-based algorithm to schedule inter-layer idle times for workpiece cooling. These techniques are validated by simulation and experiments, showing their effectiveness in preventing the detrimental effect of the heat accumulation phenomenon.

For what concerns the milling of WAAM components, this thesis pinpoints two main criticalities: the poor machinability of WAAM material and the issues related to machining the thin walled features of the WAAM workpieces. The machinability aspect is tackled by a comparative cutting force analysis on a reference material. This analysis highlights an increase of specific milling cutting forces on an AM processed material with respect to the traditional material. To overcome the issues related to thin walled features, the thesis

proposes a spindle speed optimization algorithm based on FE modelling of the workpiece. The algorithm is experimentally validated, highlighting its accuracy in predicting the workpiece dynamics and comparing the results achieved by different optimization strategies.

In summary, the aim of the thesis is to contribute to the development of the hybrid WAAM-milling, providing tools to support the process planning of such operations.

Preface

Parts of this thesis have been published in peer reviewed journals and conference proceedings. The publications reported work carried out during my Ph.D. research under the supervision of Dr. Gianni Campatelli and Dr. Antonio Scippa.

The heat source model, presented in subsection 4.3.1 is published in the proceedings of the 5th CIRP Global Web Conference Research and Innovation for Future Production as: [1] F. Montevocchi, G. Venturini, A. Scippa, G. Campatelli, Finite Element Modelling of Wire-arc-additive-manufacturing Process, in: Procedia CIRP, 2016. I developed the heat source model, implemented it in the FE code, performed the experiments and wrote the manuscript. The mesh coarsening technique presented in subsection 4.3.3 was presented in the following journal paper: [2] F. Montevocchi, G. Venturini, N. Grossi, A. Scippa, G. Campatelli, Finite Element mesh coarsening for effective distortion prediction in Wire Arc Additive Manufacturing, Additive Manufacturing 18 (2017). I developed the model, implemented it on the FE code, performed the experiments and wrote the manuscript. This paper described also the latent heat model presented in subsection 4.3.2.

For what concerns the content of chapter 5, the work on the jet impingement cooling system was presented at an Italian conference: [3] F. Montevocchi, A. Scippa, G. Campatelli, Analysis of air jet impingement cooling applied to wire arc additive manufacturing process, in: XIII Convegno dell'Associazione Ital. Di Tecnol. Mecc., 2017. I developed the model of jet impingement to be included in the finite element code, performed both the simulation and the experiments and wrote the manuscript.

The machinability analysis of the AISI H13 (section 6.1) was presented at an international conference as: [4] F. Montevocchi, N. Grossi, H. Takagi, A. Scippa, H. Sasahara, G. Campatelli, Cutting forces analysis in additive manufactured AISI H13 alloy, in: Procedia CIRP, 2016. This work was a collaboration between the University of Firenze and the Tokyo University of Agriculture and Technology. I performed the cutting test on the LENS and wrought samples, carried out the cutting force coefficients calculation and wrote the manuscript.

The activity presented in section 6.2 was presented in the MTTRF annual meeting of 2017 as: F. Montevocchi, A. Scippa, N. Grossi, G. Campatelli, Thin Walled Machining Optimization for Additive Manufactured Components, in: Proc. MTTRF 2017 Annu. Meet., 2017. I performed the experiments, worked on the optimization strategies and wrote part of the manuscript.

The idle time selection technique presented in section 5.3 is considered for publication in a peer review journal.

The activities presented in this thesis have been carried out both in Machine Tool

Research Laboratory of the Department of Industrial Engineering of the University of Firenze.

Table of contents

Summary	7
Preface	9
Table of contents.....	11
List of figures	13
List of tables	17
Acronyms List.....	19
Introduction	21
1. Thesis structure and goals.....	23
2. Hybrid additive subtractive manufacturing processes	27
2.1. Review of metal additive manufacturing processes	29
2.2. Review of the hybrid processes	34
3. The WAAM process.....	41
3.1. Arc welding processes for WAAM applications	41
3.2. WAAM machine implementation	51
4. WAAM process simulation	55
4.1. Overview of WAAM simulation	56
4.2. Macro scale simulation.....	60
4.3. Proposed model	65
4.3.1. Proposed heat source model.....	71
4.3.2. Proposed latent heat modelling technique.....	81
4.3.3. Substrate mesh coarsening technique.....	88
4.4. Conclusions and remarks.....	102

5. Application of WAAM simulation	103
5.1. Heat accumulation issue in WAAM	104
5.2. Jet impingement application to the WAAM process	108
5.3. Idle times selection technique.....	119
5.4. Conclusions and remarks	129
6. Milling of WAAM parts.....	131
6.1. Machinability of WAAM processed material	132
6.2. Machining of thin-walled components	139
6.3. Conclusions and remarks	154
7. Conclusions and final remarks	155
Acknowledgements	159
Bibliography	161

List of figures

Figure 1.1: Structure of the technical chapters of the thesis.	24
Figure 2.1: Examples of AM parts: impeller (a) [21] and fuel nozzle (b) [22].	28
Figure 2.2: Description of a generic PB (a) and DED (b) process.	29
Figure 2.3: Laser-powder deposition: Coaxial DMLD process (a) [35]; LENS process (b) [36].	30
Figure 2.4: Example of a WLAM process [16]. COAXwire equipment for WLAM deposition[30].	31
Figure 2.5: Scheme of the EBAM technology [31].	31
Figure 2.6: Example of WAAM process [16].	32
Figure 2.7: Deposition and milling end effectors of the DMG Mori Lasertec 65 [54].	35
Figure 2.8: Deposition and milling end effectors of the Mazak Integrex I 400 AM [55].	35
Figure 2.9: Deposition and milling end effectors of the Mazak Variaxis J 600 AM [57].	36
Figure 2.10: ArchHLM hybrid solution [43].	37
Figure 2.11: Hybrid WAAM-milling machine implemented at the Cranfield university: overall view of the machine (a) [15] and high pressure rolling system (b) [58].	37
Figure 2.12: The retrofit system provided by Hybrid Manufacturing Technologies [60]: the system installed on a turn-milling machine (a) and the deposition tool (b).	38
Figure 2.13: Hybrid WAAM-milling concept proposed in the LASIMM project [62].	39
Figure 3.1: Scheme of the GTAW (a) and GMAW (b) processes.	41
Figure 3.2: Scheme of the PAW process [16].	42
Figure 3.3: Interconnection between the step of WAAM process planning and the most common process issues.	44
Figure 3.4: GMAW process parameters.	45
Figure 3.5: Weld bead dimensional parameters.	45
Figure 3.6: Example of WAAM part with layers crossing.	46
Figure 3.7: Example of arc striking and extinguishing defects [79].	47
Figure 3.8: WAAM workpiece affected by distortion (a); Temperature-stress history [84], outlining the residual stresses formation principle (b); WAAM workpiece undergoing overheating (c).	48
Figure 3.9: Roland Modela MDX-40A [97].	51
Figure 3.10: Relevant components of motors driving and control chain.	52
Figure 3.11: Assembled WAAM machine prototype	53
Figure 3.12: Examples of demonstrators manufactured by the implemented machine: blade-like part (a); box-like part after the deposition (b); box-like part after milling finish.	54
Figure 4.1: Overview of the transfer phenomena in a WAAM process	56

Figure 4.2: Interactions between the electric arc, the molten pool and the surrounding material.....	57
Figure 4.3: Interaction between the heat transfer and the mechanical domain in macro scale models.	61
Figure 4.4: WAAM simulation model highlighting active and inactive elements (b) pattern of the generic γ function used for element activation.....	66
Figure 4.5: Thermal properties used in the WAAM simulation	68
Figure 4.6: Mechanical properties used in the WAAM simulation.	69
Figure 4.7: Local coordinate system used for the heat source definition.	70
Figure 4.8: Scheme of the procedure used to evaluate the heat source function.....	70
Figure 4.9: Goldak double ellipsoid model.....	72
Figure 4.10: Proposed heat source model.	73
Figure 4.11: Filler mesh interaction with proposed heat source model.	74
Figure 4.12: Test cases dimensions and actual bead on plate.	76
Figure 4.13: FE model of the test case.....	77
Figure 4.14: Procedure used to estimate the heat source parameters.	77
Figure 4.15: Midline displacements for the bead on plate.	78
Figure 4.16: Bead on plate models temperature field [K] a) Goldak b) Proposed model.	79
Figure 4.17: Thermocouples positions in the temperature measurement test.	79
Figure 4.18: Comparison of the thermocouple data with the simulations performed using both the proposed and the Goldak heat source model.	79
Figure 4.19: Example of a modified heat capacity curve, including the latent heat effect. ...	82
Figure 4.20: Temperature rise due to the heat source passage drawn from a WAAM simulation.	83
Figure 4.21: General pattern of the liquid phase fraction function.	84
Figure 4.22: The FE model used to test the heat source effectiveness.....	85
Figure 4.23: Result of the FE simulation in terms of contour plot at two different steps.	86
Figure 4.24: Comparison of the model performances at different time steps in terms of: elapsed simulation time (a); error on the control node peak temperature with respect to the reference simulation.	86
Figure 4.25: Comparison of thermocouples data with FE simulations with and without latent heat model.	87
Figure 4.26: Comparison of the proposed coarsening technique (a) and mesh biasing (b). ..	90
Figure 4.27: Rosenthal model outline.....	92
Figure 4.28: Simple bead on plate geometry (a) modelled using the proposed technique (b).	93
Figure 4.29: Temperature profile interpolation through mesh zoning (a) and stepwise algorithm outline (b).....	94
Figure 4.30: Geometry of numerical validation models.	96
Figure 4.31: Comparison of mesh biasing, mesh zoning and reference models.	97
Figure 4.32: Reference model temperature profile (a); biased and proposed models error (b).	98
Figure 4.33: Test case dimensions and actual appearance.	99
Figure 4.34: Mesh size pattern for the wall model.	100
Figure 4.35: Predicted and experimental top surface deformed geometry.....	100
Figure 4.36: Predicted and experimental comparison lines at: $Y=5\text{mm}$ (a) and $Y=145\text{mm}$ (b).	101
Figure 5.1: Modes of evacuation of the molten pool heat.....	104

Figure 5.2: A WAAM component affected by structural collapse, highlighted by the non-vertical pattern of the cylindrical surface.....	105
Figure 5.3: Different microhardness and phase content along the workpiece height in WAAM processed ER70S-6 [153].....	106
Figure 5.4.: Archetype of proposed cooling system.	109
Figure 5.5: Geometric parameters of a generic jet impingement system.....	110
Figure 5.6: The curves used to calculate non-dimensional adiabatic wall temperature.....	111
Figure 5.7: Testing equipment (a) and IR image of the target after 900 s of cooling (b).	113
Figure 5.8: FE model: initial state of the warm up simulation (a); final state of the cooling simulation (b);	114
Figure 5.9: Comparison of tests and modelling results: time history during the warm up test (a); temperature profile at the end of the cooling test (b).	114
Figure 5.10: Example of a wall produced by WAAM process(a); FE element model used for the numerical test (b).....	116
Figure 5.11: Comparison of temperature field of reference and jet impingement simulations during the deposition of 4th and 10th layers	117
Figure 5.12: Comparison of temperature time histories at two different distances from the base plate.....	118
Figure 5.13: Control points location strategy.	120
Figure 5.14: FE simulation strategy used for the idle times calculation	121
Figure 5.15: Idle times calculation procedure.	122
Figure 5.16: The airfoil used as test case: dimensions and thermocouple arrangement (a); actual manufactured part	123
Figure 5.17: FE model of the test case.	124
Figure 5.18: Results of the idle time calculation procedure: idle times values (a) and molten pool volume for each layer.	125
Figure 5.19: Comparison of simulation and thermocouple data.	127
Figure 5.20: Comparison of the measured blade surface and the reference CAD model.	128
Figure 6.1: Wrought (a), WAAM (b) and LENS (c) material specimens.....	133
Figure 6.2: LENS (a) and WAAM (b) specimen test set-up.....	133
Figure 6.3: Cutting parameters in a peripheral milling operation.....	134
Figure 6.4: Average force per tooth revolution (a); linear relation between average force and feed per tooth (b).....	136
Figure 6.5: Hot chip during LENS specimen slot milling.	137
Figure 6.6: Comparison of average values of feed (a) and normal (b) forces.	138
Figure 6.7: Geometry of the test case selected for the verification of the proposed technique.	141
Figure 6.8: a) Roughing cycle, b) finished part	142
Figure 6.9: Test case discretized by shell elements: traditional (a) and 3D (b) representations.	143
Figure 6.10: Association between FE model nodes and G-code points.....	143
Figure 6.11: Stock geometry updating: calculation of the engagement (a) updated FE model (b).....	144
Figure 6.12: Workpiece FRFs evaluated at the leading edge at different distances from the base.	144
Figure 6.13: Comparison between the workpiece, tooltip and combined FRF.....	145
Figure 6.14: Results of the comparison between impact testing FRFs and the calculated ones.	146

Figure 6.15: Frequency content of the cutting forces for a peripheral milling operation with a ball nose tool.	147
Figure 6.16: Outline of the optimization strategy A.	148
Figure 6.17: Weights assigned to the cutting force harmonics for optimization.	148
Figure 6.18: Modulated spindle speed pattern calculated by the optimization strategy B... ..	149
Figure 6.19: The first two modes of the airfoil during the finishing step	150
Figure 6.20: Comparison of measured camber lines and airfoil thickness with the reference one.	151
Figure 6.21: Thickness error along chordal distance and blade height for the three specimens.	151
Figure 6.22: Comparison of the roughness achieved by using the three optimization strategies.	152
Figure 6.23: Applicability ranges of the different optimization strategies.	153

List of tables

Table 2.1: Comparison of metal AM and milling accuracy.....	28
Table 2.2: Overview of the available DED processes	30
Table 2.3: Comparison of DED processes in terms of deposition rate and part size	32
Table 2.4: Commercial hybrid machines currently available	34
Table 3.1: Summary of the main WAAM researches and examples of relevant works in the respective fields.....	50
Table 4.1: Goals of the micro [108] (a) and macro (b) scale simulation of the WAAM process.....	58
Table 4.2: Strategies used in macro-scale simulation to model energy and material input. ...	63
Table 4.3: Solidus temperature, liquidus temperature and latent heat of fusion of the selected materials	68
Table 4.4: Summary of the state of the art solution regarding the heat source models.	71
Table 4.5: Heat source parameters.	77
Table 4.6: State of the art techniques to increase the simulation time step	81
Table 4.7: State of the art techniques to reduce the model DOFs.....	89
Table 4.8: Heat source dimensional parameters used for the numerical validation.....	97
Table 4.9: Elapsed simulation time for the different substrate discretization.	98
Table 4.10: Process parameters used to manufacture the test case.	99
Table 4.11: Summary of the thesis contributions to the WAAM simulation SoA.	102
Table 5.1: Summary of the state of the art techniques to mitigate the heat accumulation issue.	107
Table 5.2: Process parameters used for the test case manufacturing.	123
Table 5.3: Summary of the thesis contributions to the heat accumulation SoA.	129
Table 6.1: Rockwell C hardness measuring results.	134
Table 6.2: Tests cutting parameters	136
Table 6.3: Cutting coefficients identification results.....	138
Table 6.4: Summary of the state of the art works related to milling of thin walled pars.	140
Table 6.5: Process parameters used for the test cases manufacturing.	141
Table 6.6: Summary of the thesis contributions to the machining of WAAM components.	154
Table 7.1: Summary of the thesis contribution to the state of the art	157

Acronyms List

AM	Additive Manufacturing
BC	Boundary Condition
CFD	Computational Fluid Dynamics
DC	Direct Current
DED	Direct Energy Deposition
DMLD	Direct Metal Laser Deposition
DOF	Degree Of Freedom
EBAM	Electron Beam Additive Manufacturing
FE	Finite Element
FEM	Finite Element Method
FRF	Frequency Response Function
GMAW	Gas Metal Arc Welding
GTAW	Gas Tungsten Arc Welding
IR	Infrared
LENS	Laser Engineered Net Shaping
NC	Numerical Control
OEM	Original Equipment Manufacturer
PAW	Plasma Arc Welding
PB	Powder bed
SLS	Selective Laser Sintering
SoA	State of the Art
WAAM	Wire Arc Additive Manufacturing

Introduction

Among the recent innovations in the manufacturing sector, metal AM (Additive-Manufacturing) is one of the most significant. These technologies create fully functional components by progressive addition of metal layers. Compared to tradition approached, this enable to achieve significant advantages [5]: increased design freedom, possibility to integrate different components, reduction of material waste, reduction of machines set-up time and cost, reduction of the feedstock procurement time. For this reason, many industrial sectors are attracted by the potential of the metal AM processes. The biomedical industry is widely experimenting metal AM processes to manufacture prosthetic bones [6]. Using metal AM allows to manufacture tailored components at a reduced production cost. The aerospace industry is widely experimenting metal AM to test innovative light-weight design of both engine and structural components [7]. The energy sector is using metal AM technologies to simplify the manufacturing and assembly workflow of its products [8]. These applications are just an example to outline the great interest of the industry around metal AM.

Currently, many different metal AM processes are available as market solution. These technologies exploit different principles to create the components, namely different heat sources and feedstock. Currently, the most widespread and consolidated metal AM technologies are the ones based on powder feedstock and laser heat sources [9]. These technologies experienced a faster development and a wider diffusion mainly due to their higher accuracy and feature resolution [10,11]. However, introducing such technologies in the process chain requires a relevant investment. The power source is demanding as cost and energy consumption [12]. Moreover, metal powder is an expensive feedstock compared to other forms such as wire. An example is the AISI 316 stainless steel: while the wire feedstock is about 2.5 €/kg, the metal powder can be up to 90 €/kg [13]. Furthermore, the companies willing to adopt metal AM must invest to set up the process to meet their specific requirements and needs. These factors limit the diffusion of metal AM processes among small and medium companies with reduced investment capabilities. However, many small companies operating in strategic sectors could take advantage of the metal AM potential as the largest enterprises. This can be achieved by using less demanding metal AM technologies.

The hybridization approach enables to combine AM processes with traditional machining. This reduces the importance of dimensional accuracy and surface finish achievable by the metal AM process, since the functional requirements can be achieved by machining the workpiece [14]. This enables to use AM processes providing a lower accuracy but that requires lower investments. The most representative one is the WAAM

(Wire-Arc-Additive-Manufacturing) process. This process uses an electric arc to melt the feedstock, provided as metal wire. Compared to laser based technologies, WAAM has a lower accuracy and produces components with wavy surfaces. However, such issues are not relevant in a hybrid process, where the workpiece undergoes a finishing operation by machining. Moreover WAAM has different higher deposition rate and is capable to manufacture much larger components [15]. Due to the type of heat source and feedstock used by WAAM, it is much more demanding than the laser based processes in terms of investments. Hence it represents an interesting process for small manufacturing companies willing to exploit the benefits provided by the AM processes.

Despite its positive features, the hybrid WAAM-milling process has still drawbacks which limit its diffusion among the manufacturing companies. Most of them are related to the thermal aspect of the WAAM process [16]. The high amount of heat introduced in the workpiece can cause residual stresses, distortions, part collapse and material properties modifications. Moreover, even the machining step can be a critical operations [17]. Indeed, despite machining is a consolidated technology, processing WAAM components present issues related to the WAAM material machinability and to the typical geometries of WAAM components.

Despite its criticalities, the hybrid WAAM-milling process has the potential to become an alternative approach to laser based AM technologies among the small manufacturing companies. However, the process requires further researches to address better understand its criticalities and to identify possible solutions improving the technology readiness.

The aim of this thesis is to contribute to the development of the hybrid WAAM milling process. The hybrid technology is analyzed considering both the WAAM and the milling process. On the WAAM side, the thesis considers the thermal issues of the process, focusing on specific prediction and mitigation strategies. On the milling side, the thesis analyzes both the issues related to workpiece material and geometry.

1. Thesis structure and goals

The aim of this thesis is to provide useful tools and methods to increase the knowledge and the insight on the hybrid WAAM-milling process with the final objective of increasing its performances both in terms of productivity and parts quality.

The AM processes dedicated to metals provide great potential advantages compared to the traditional technologies, such as an increased design freedom, the reduction of material waste and an increased operational flexibility. Nevertheless, such processes cannot cope with the common functional requirements of the industrial parts in terms of dimensional accuracy and surface finish. The hybrid approach overcomes these limitations combining AM with traditional machining: the AM is used as a primary process to create the overall geometry of the component, while machining is used to finish the component, achieving the functional requirements.

Currently the hybridization can be achieved using different AM processes. This thesis focuses on the combination of the Wire-Arc-Additive-Manufacturing (WAAM) technology with the traditional milling process. WAAM is an AM technology based on the consolidated arc welding process. It enables to manufacture large components with a high deposition rate. Its main drawback is the reduced dimensional accuracy. However, it can be easily tackled by combining it with the milling process, making WAAM an ideal technology for the hybrid approach.

Despite the attractive features of the hybrid WAAM-milling process, several drawbacks are still limiting its diffusion among the manufacturing companies. Despite the WAAM issues concerning the accuracy are not relevant in the hybrid approach, the process has further drawbacks, not eliminable with post process milling. Such issues can be categorized in two main groups: the ones directly related to the WAAM process and the ones related to the post process milling of WAAM components. This thesis aims at addressing both, with the final goal of increasing the performances of this hybrid process. Despite this, most of the work is related to the WAAM process, since milling is a consolidated technology and its issues are only related to the specific application. On the opposite, WAAM is an innovative process, requiring larger research efforts to overcome its current limitations.

An initial analysis of the scientific literature related to WAAM outlined that it is affected by thermal issues. The welding process introduces a large amount of heat into the workpiece, inducing a non-uniform temperature field. This results workpiece distortions, residual stresses and even in the structural collapse of the workpiece. The FEM is an effective tool to tackle the WAAM thermal issues: the process simulation provides a deep insight of the workpiece thermal behavior, allowing to analyze the effect of the process parameters and to investigate possible mitigation strategies with a reduced number of

experiments. Nevertheless, the current process models are highly demanding in terms of calculation time.

The first part of this thesis aims at developing innovative modelling techniques to reduce the simulation time. Three main innovations are proposed: a heat source model, a new technique to include the latent heat of fusion and a technique to reduce the number of elements required for the analysis. These techniques are validated through experiments.

The second part of the work on the WAAM process aims at applying the developed modelling techniques to tackle the heat accumulation issue, namely the overheating of the workpiece that can cause its structural collapse, poor dimensional accuracy and uneven material properties. The FE model was used to develop and test two different strategies to tackle this problem: the workpiece cooling through impinging air jets and an algorithm to schedule interlayer idle times to allow the workpiece to cool down.

For what concerns the milling of WAAM components, an analysis of such process identified its main criticality as the machinability of WAAM processed material. Due to the thermal cycles occurring in the workpiece, the material undergoes significant phase transformations and microstructure modification. Hence the WAAM processed material is likely to have a different machinability with respect to the raw one, requiring preliminary investigations to assess suitable cutting parameters. In this thesis, this topic is treated by carrying out an analysis of the cutting forces in milling operation of a WAAM processed material. Besides the machinability, a further criticality was identified: WAAM is a convenient alternative to traditional processes for thin walled parts rather than for bulk ones. Hence, post process milling is performed on thin walled parts, usually prone to vibration issues. This requires a careful assessment of cutting parameters. This thesis proposes an innovative algorithm to optimize the spindle speed with the aim of mitigating the machining errors related to workpiece vibrations.

Figure 1.1 outlines the organization of the thesis and the main contribution with respect to the state of the art.

PROCESS		TOPICS	CONTRIBUTIONS	RESULTS	GOAL
HYBRID WAAM-MILLING	WAAM	CHAPTER 4 WAAM FE MODEL	<ul style="list-style-type: none"> HEAT SOURCE MODEL LATENT HEAT MODEL MESH COARSENING 	TOOLS AND METHODS TO TACKLE THE WAAM ISSUE OF HEAT ACCUMULATION	INCREASE THE PERFORMANCES OF THE HYBRID WAAM-MILLING PROCESS
		CHAPTER 5 FE MODEL APPLICATION	<ul style="list-style-type: none"> JET IMPINGEMENT IDLE TIMES SELECTION 		
	MILLING	CHAPTER 6 MACHINABILITY	<ul style="list-style-type: none"> CUTTING FORCE ANALYSIS 	INCREASED KNOWLEDGE OF THE ISSUES RELATED TO WAAM PARTS MACHINING	
			THIN-WALLED PARTS MILLING		

Figure 1.1: Structure of the technical chapters of the thesis.

Chapter 2 and 3 introduce the framework of the thesis, while chapters from 4 to 6 describe the research activities and the contributions to the state of art. Chapter 2 is dedicated to the of hybrid AM-machining concept, reviewing the state of the art solutions, both from an industrial and a research perspective. Chapter 3 is dedicated specifically to the WAAM process, describing its key aspects and reviewing the most relevant researches. The final part

of chapter 3 describes the WAAM machine prototype created to carry out the experimental activities of the research. Chapters 4 and 5 present the activities related to the WAAM process. Chapter 4 presents the WAAM model, introducing the state of the art and describing the proposed techniques. Chapter 5 deals with the application of the FE simulation to the heat accumulation issue, detailing both the jet impingement cooling technique and the idle time selection algorithm. Chapter 6 is related to the post process machining with a section related to the machinability issue and a further one presenting the spindle speed selection algorithm.

2. Hybrid additive subtractive manufacturing processes

The ASTM defined AM as: “a process of joining materials to make objects from 3D model data, usually layer upon layer, as opposed to subtractive manufacturing methodologies” [18]. These processes were initially introduced for rapid prototyping applications [19]. The early processes allowed only to manufacture polymer components, not suitable for many functional applications. The introduction of AM processes dedicated to metals [20] enabled the production of functional components suitable for harsh operational conditions (e.g. high stresses, high temperatures).

Using AM processes for metal parts (namely: metal AM) is an attractive technology for the manufacturing companies since it has the potential to provide significant advantages compared to the traditional processes [5]:

- **Increased design freedom:** manufacturing components layer by layer enables to introduce complex features, such as embedded voids, impossible to be manufactured by other technologies. An example of a component design exploiting AM potential is shown in Figure 2.1 (a) [21]: a pump impeller is manufactured embedding void volumes in the hub to reduce its mass.
- **Components integration:** the larger compliance of AM technological constraints provides the possibility of integrating multiple components, reducing the number of assembly and joining operations. General Electric exploited this advantage of AM to simplify the manufacturing process of the fuel nozzle shown in Figure 2.1 (b). The nozzle, initially made out of more than 20 components, is manufactured as a single part through a metal AM process [8].
- **Material savings:** traditional processes such as forging or casting requires intensive post process machining to achieve the final geometry of the component. AM components require only finishing operations to meet dimensional tolerances and surface finish, providing a significant reduction of the removed material volume.
- **Flexibility:** unlike casting or forming processes, AM does not require tailored tools for each part (e.g.: moulds or dies). This significantly increases the flexibility of the production, resulting in a reduction of the production costs for small batches of complex parts.

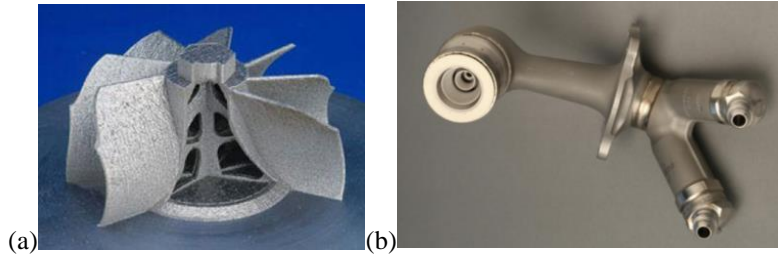


Figure 2.1: Examples of AM parts: impeller (a) [21] and fuel nozzle (b) [22].

Despite their advantages, metal AM processes cannot provide the same accuracy and surface finish of the traditional machining. Table 2.1 compares the dimensional accuracy and the surface finish achievable by a milling operation (finishing) and an AM process (average values obtained considering different processes) [8]:

Table 2.1: Comparison of metal AM and milling accuracy

Dimensional Accuracy [mm]	
<i>Metal AM</i>	<i>Milling</i>
0.07÷0.2	0.02
Surface finish [μm]	
<i>Metal AM</i>	<i>Milling</i>
10÷40	0.8÷6

As highlighted by these data, the main difference between metal AM and machining occurs in terms of achievable surface finish. This is expected since metal AM involves the total or partial fusion of the material, resulting in poor surface finish.

Due to the aforementioned limitations, the AM components require a post-processing phase by means of machining operations. This need led to the introduction of the hybridization concept: integrating an AM and a machining process on a single machine [23]. Besides increasing the metal AM accuracy, this approach has the following advantages:

- **Elimination of workpiece repositioning:** this operation usually results in time inefficiencies and loss of accuracy. Integrating the AM and the machining process is a potential solution to such issues.
- **Increased productivity:** metal AM processes lack of productivity, compared to the machining ones [24]. The hybrid approach provides the possibility of increasing the overall productivity, allowing to select whether a feature should be manufactured by AM or machined.

Many different hybrid solutions can be created, starting from different metal AM processes. The performance and field of application of the resulting hybridizations depend on the features of the involved processes. The aim of this chapter is to discuss the reasons that led to the choice of the hybrid WAAM-milling technology. Section 2.1 reviews the available metal AM processes, highlighting their advantages and criticalities in relation with their application on a hybrid machine. Section 2.2 is dedicated to hybrid solutions currently available on the market.

2.1. Review of metal additive manufacturing processes

Metal AM processes create the component by stacking subsequent layers of material along the building direction. Most of them create the component layers by using a heat source to melt the feedstock. Some exceptions exist, such as the laminated object manufacturing [25] or the cold spray [26] technologies. However, due to their limited application to specific niches, they were not considered as suitable technologies for this thesis.

The processes based on material fusion can be classified in two main categories [9]: PB (Powder Bed) and DED (Direct Energy Deposition processes). Figure 2.2 outlines the distinctive features of the two process categories.

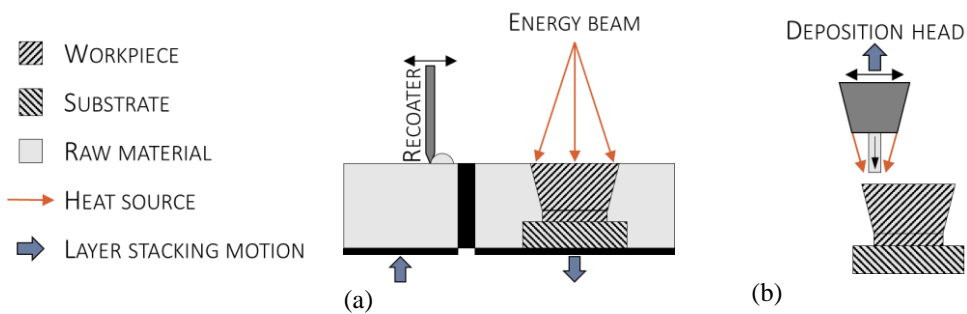


Figure 2.2: Description of a generic PB (a) and DED (b) process.

In PB processes (Figure 2.2 (a)) the layers of the component are created by selectively melting the raw material, provided in form of powder. A recoater lays a powder bed on the top of a building platform. A high energy beam is focused on the powder bed surface, melting the raw material. A beam guidance system moves the focus point according to the layer geometry, achieving a selective melting of the powder bed. The building platform is then lowered (layer stacking motion in Figure 2.2 (a)) and the process starts back for a new layer.

In opposition to the PB processes, the DED ones (Figure 2.2 (b)) create the layers of the component by selective deposition, rather than selective melting. Both the feedstock and the energy required to melt it are delivered by a deposition head, which is moved according to geometry of the layer. Hence the component is created by selectively depositing the molten raw material. It must be pointed out that both the DED and the PB processes require a substrate, that is a solid metal base to create the first layer.

The main differences between the DED and PB processes are the achievable feature resolution and components size [9]. The PB processes can produce relatively small parts but with high features resolution and accuracy. On the opposite, the DED processes have lower feature resolution and accuracy but can produce larger components. An example of this difference is given by the comparison of the SLS (Selective-Laser-Melting) and the DMLD (Direct-Metal-Laser-Deposition). Both these processes use a laser beam as heat source and metal powder as raw material. However, Zhu et al. reported a dimensional accuracy of ± 0.05 mm [10] for the SLS process, while Milewski et al reported an accuracy of ± 0.13 mm for the DMLD process [11]. On the opposite, laser based DED processes allow to fabricate parts up to 1 m of maximum length, while the SLS process is limited to 300 mm. For this

reason, the DED processes are more suited for the hybridization, while the PB ones are more likely to be used as near net shape processes. Hence, due to the purpose of this review, the analysis of the available technologies is focused on the DED processes. First the available DED alternatives are presented, outlining their working principles. Then the processes are compared in relation with their suitability to a hybrid process.

The DED processes can be classified according to the type of raw material and heat source. Table 2.2 presents the most relevant DED processes and their OEMs (Original Equipment Manufacturer).

Table 2.2: Overview of the available DED processes

Powder feedstock		
<i>Heat source</i>	<i>Process</i>	<i>OEMs</i>
Laser	DMLD	Trumpf[27], BeAM[28]
	LENS	OPTOMECH[29]
Wire feedstock		
<i>Heat source</i>	<i>Process</i>	<i>OEMs</i>
Laser	WLAM	Fraunhofer IWU[30]
Electron beam	EBAM®	Sciaky [31]
Electric arc	WAAM	Gefertec [32], MUTOH [33]

It must be pointed out that Table 2.2 considered only the commercial processes. Different combination (e.g. electric arc and powder [34]) were tested only as research applications.

The DMLD (also referred to as laser cladding) and the LENS processes exploit the energy of a laser source to melt the metal powder feedstock. Figure 2.3 presents a scheme of the two technologies.

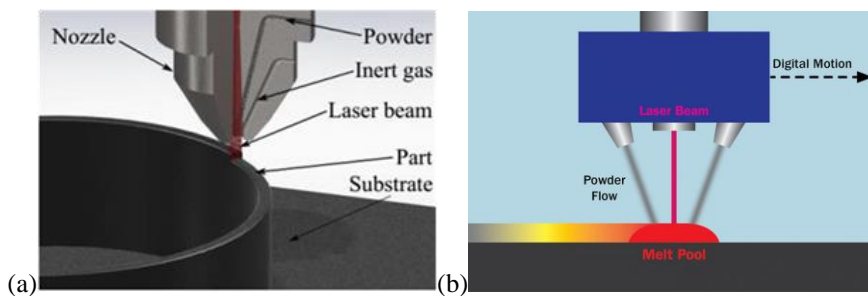


Figure 2.3: Laser-powder deposition: Coaxial DMLD process (a) [35]; LENS process (b) [36].

The laser beam, guided by a lenses system, heats the base material creating the molten pool, namely a region of molten material onto the workpiece. The powder is conveyed on the molten pool by means of a carrier gas and molten by the laser before hitting the pool. The main difference between the DMLD and the LENS processes is the powder feeding direction [20]: in DMLD the powder flow is coaxial to the laser (Figure 2.3 (a)) while in the LENS

process the powder is fed by external nozzles, tilted with respect to the beam aiming direction.

The WLAM is a further laser based DED technology. In this process, the feedstock is fed in the molten pool as a solid metal wire, as shown in Figure 2.4

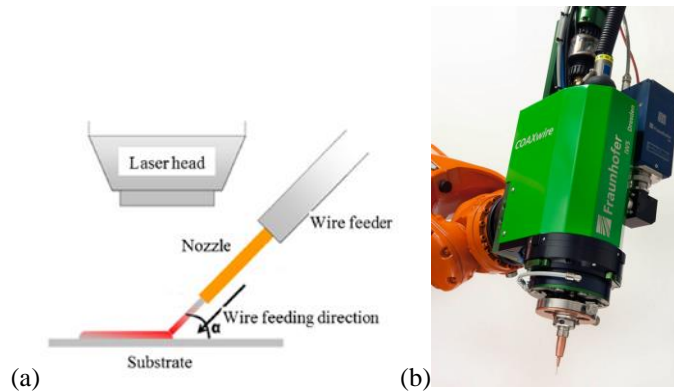


Figure 2.4: Example of a WLAM process [16]. COAXwire equipment for WLAM deposition[30].

In this process, the wire is usually fed by an external nozzle (Figure 2.4 (a)), tilted with respect to the laser aiming axis. This can be a potential source of issues in manufacturing complex parts since the feeding angle should be kept fixed due to its high influence on the bead quality [37]. For this reason, in the commercial version of WLAM (COAXwire, released by Fraunhofer IWU) the wire is fed coaxially to the laser beam [38]. This equipment is distributed as a deposition head to be used as an end-effector for robot arms (Figure 2.4 (b)).

The EBAM process, also referred to as EBF³, is a wire based technology that uses an electron beam as heat source. A basic scheme of the process is shown in Figure 2.5.

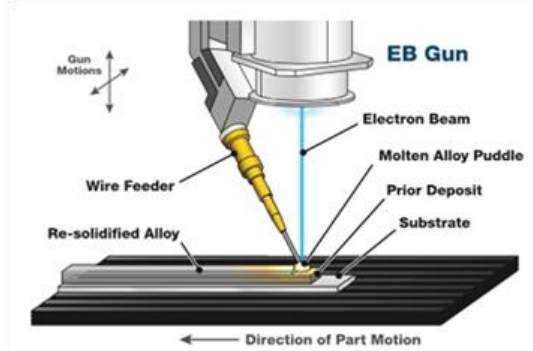


Figure 2.5: Scheme of the EBAM technology [31].

The working principle of the heat source is the same used in the electron beam welding process [39]: a stream of electrons is generated by thermionic emission at a cathode and it is focused on the workpiece surface by an electric field. The interaction between the electrons and the workpiece material generates the heat required to form the molten pool and to melt the filler metal. The all process is carried out in a hard-vacuum environment to

prevent the ignition of an electric arc. As in the WLAM process, the wire is not fed coaxially with the electron beam but is provided by an external feeder (Figure 2.5).

The WAAM process is a wire based technology using an electric arc as a heat source. Figure 2.6 shows an example of a such technology.

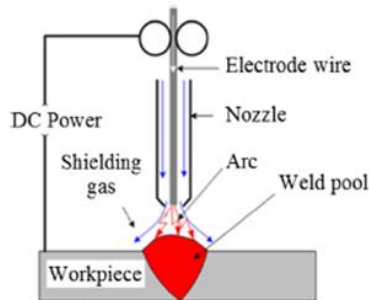


Figure 2.6: Example of WAAM process [16].

Basically, WAAM uses the traditional arc welding technologies, such as GMAW (Gas Metal Arc Welding) or GTAW (Gas Tungsten Arc Welding) as a DED technology. A voltage drop is created between an anode and a cathode, ionizing a shielding gas and creating an electric arc. The heat generated from the electric arc provides the energy required to melt both the filler and the base material. The layout of the deposition head is different, depending on specific arc welding process. However, the general features of the WAAM process can be assessed and compared with the other DED technologies, independently of the specific arc welding technique. It must be pointed out that, despite a company delivers a commercial WAAM machine (Table 2.2), WAAM operations are often performed using standard equipment for automated arc welding operations, such as welding robot arms [40].

As earlier mentioned, the comparison of the DED processes was carried out analyzing their suitability to a hybrid process. Table 2.3 outlines some relevant features of the presented DED processes: the achievable deposition rate, i.e. the deposited mass per unit time, and the maximum part size.

Table 2.3: Comparison of DED processes in terms of deposition rate and part size

Comparison of DED processes		
<i>Process</i>	<i>Deposition rate [kg/h]</i>	<i>Max. part size [m]</i>
DMLD, LENS	0.6 [41]	Around 1.5 [9]
WLAM	2.9 [16]	Related to equipment
EBAM	Up to 19.5 [42]	5.8 [31]
WAAM	6.0 [43]	Related to equipment. Max. achieved 10.0 [44]

It must be pointed out that advantages and drawbacks of the different DED processes are related both to the feedstock and to the heat source. Hence comparing the different processes means comparing both these aspects. The first point highlighted by the data presented in Table 2.3 is related to the feedstock type, since the powder based processes

significantly lack both in terms of deposition rate and maximum component size. The low deposition rate is due to the poor efficiency in material usage of these processes: the powder is blown over the molten pool but not all of it is molten. This results in a large waste of powder. This was observed by Syed et al. [45], while comparing the performances of powder and laser based deposition. It was stated that the powder based process significantly lacked in material usage efficiency, requiring larger laser power and material delivery rate to achieve the same deposition rate of the wire based process. For what concerns the maximum component size, it is currently limited by the powder feeding systems. Laser-powder machines use a gas stream to deliver the feedstock. An increase in machine size would result in an excessive increase of the head losses in the pneumatic circuit. Besides the drawbacks outlined in Table 2.3, powder is a potential source of defects in the workpiece, such as porosity or inclusion of unmolten powder grains. These defects are not present in wire based processes ([45],[46]). Despite their issues, the powder based processes are widely tested and used by the OEMs due to their higher feature resolution with respect to the wire based technologies that enables to manufacture components with higher complexity. As stated by Demir [47], the minimum bead size, namely the feature resolution, achievable by the wire processes is limited from 5 to 15 times the wire diameter. This limitation can be overcome by decreasing the wire diameter, but this results in a reduction of the deposition rate. Hence, a trade-off exists between achievable deposition rate and complexity: wire based processes are suited to manufacture large parts, with limited features complexity at a high build rate; powder based technologies are more suited to produce small parts with a higher features complexity. Since DED technologies cannot be competitive with the PB ones in terms of achievable complexity, this thesis focused on the technologies dedicated to large components, hence on wire based processes.

According to the presented review, three different heat sources can be used in wire-feed DED, namely laser, electron beam and electric arc. These can be categorized in two groups: high and low energy density sources. Laser and electron beam belongs to the high energy density group [48], i.e. these processes enable a high focus of the beam energy, reducing the overall amount of thermal power required to melt the filler metal. This results in a reduction of the process heat input, defined as:

$$H = \frac{\dot{Q}}{v_f} \left[\frac{J}{m} \right] \quad \text{Eq. 1}$$

Where \dot{Q} is the heat source power and v_f is the travelling speed during the deposition. This quantity represents the amount of heat introduced in the workpiece per unit of deposited length. A low heat input allows to mitigate the AM thermal issues, such as residual stresses and distortions [49]. Hence, laser and electron beam processes exhibit reduced thermal issues compared to the electric arc ones. The main drawbacks of such processes concern the cost related to their installation and application to large hybrid machines. First, they require a high initial investment due to their higher complexity with respect to the electric arc sources [43]. Moreover, laser has a poor conversion efficiency (about 10% against 95% of the electron beam [50]). This makes inconvenient the usage of high laser power required to achieve a high deposition rate, important to achieve a time efficient AM production of large components. Electron beam sources have a far higher energy efficiency that the laser ones. On the other hand, the electron beam sources require a hard-vacuum environment. This increases the cost required to implement such sources on large machines. Moreover, both

WAAM and WLAM operations can be performed using existing machine tools or robots [43]. This reduces the overall technology installation cost. The requirement of a hard-vacuum environment makes this approach unpracticable for electron beam sources.

The WAAM process represents a promising solution for hybrid machines, dedicated to the production of large metal components. This technology combines the possibility of achieving high deposition rates with a reduced installation cost, enabling to exploit existing machines by the installation of a deposition head as an additional end effector.

2.2. Review of the hybrid processes

Table 2.4: Commercial hybrid machines currently available

OEM	Process	Machine
		Lasertec [51]
DMG Mori	DMLD	
		Integrex I 400 AM [51]
Mazak	DMLD	
		Lumex Advance-25 [52]
Matsuura	SLS	
		Variaxis J 600 AM [53]
Mazak	WAAM	

In last years, the interest grown around hybrid machines led the main machine tool OEMs to include such products in their commercial offer. Currently there are two possible solutions to achieve an AM-machining hybridization: acquiring a brand-new hybrid machine or retrofitting an existing traditional machine tool. This section reviews the most relevant solutions, presenting and discussing their advantages and drawbacks. First the commercial offer of brand-new hybrid machines is presented. Then the retrofitting solutions are reviewed.

The commercial brand-new hybrid machines are listed in Table 2.4. As for the standalone AM machines, powder-based DMLD is the technology most used by the machine tools OEMs. Both DMG Mori and Mazak delivers hybrid solutions based on this process. Figure 2.7 shows the layout of the DMG Mori hybrid machine, the Lasertec 65 AM.



Figure 2.7: Deposition and milling end effectors of the DMG Mori Lasertec 65 [54].

This machine is based on the architecture of a 5-axis vertical milling center, with the rotary axes located on the table side. The operating mode can be switched from AM to machining by means of an automated system that that works as an automatic tool changer. The system withdraws both the milling spindle and the deposition head from a dedicated magazine and clamp them to the machine. The connection is designed to supply all the required utilities to both the deposition head and the spindle, such as the gas-powder mixture, the electrical power and the spindle coolant. The Mazak DMLD solution (Integrex I 400 AM) is similar to the DMG one. Figure 2.8 shows the end-effectors of this machine.

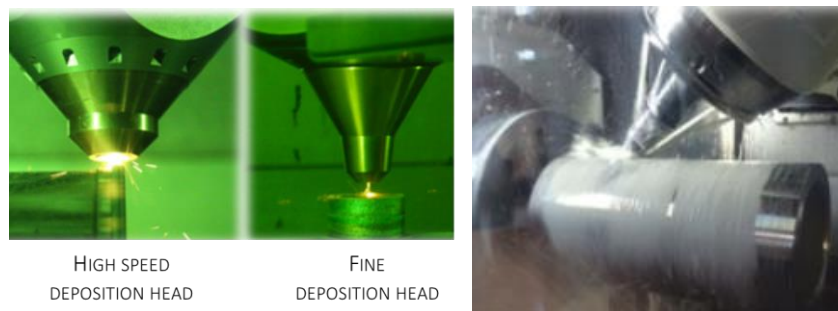


Figure 2.8: Deposition and milling end effectors of the Mazak Integrex I 400 AM [55].

The main difference between this machine and the DMG Mori one, is its architecture. The Integrex I 400 AM is configured as a 5-axis turn-milling center, whit a rotary axis (C

axis) provided by the turning spindle and a further one on the milling-deposition gimbal head (Figure 2.8). This machine is equipped with two deposition heads, fitted with different nozzles to achieve high productivity or high feature resolution (high speed deposition head and fine deposition head in Figure 2.8). The different nozzles design enable a different focus of the carrier gas stream [56], allowing to achieve high gas flow rate for high productivity or a high focus, for the deposition of small features that requires small beads.

It must be pointed out that despite the different architecture both the Mazak and the DMG Mori machines use a 5-axis kinematic. This solution avoids the introduction of supports to manufacture components with overhanging parts, since the gravity action can be counteracted by re-orienting the workpiece. This is a relevant advantage of the DED processes, since the supports must be removed after the deposition. This is a time consuming and complicated operation in complex components.

As previously stated, the most suitable AM processes for an integration in a hybrid machine are the DED ones. However, Matsuura provides a hybrid solution that integrates a PB process (SLS) and milling (Table 2.4). In this machine, the workpiece is created by SLS and the milling process is used to finish the workpiece edges, improving its accuracy and surface finish [20]. This operation is carried out every 5 layers. This is a different concept of hybrid machine since the subtractive process is used to improve the performances of the AM one but the end-user is not allowed to create complete features by machining (e.g.: pinholes). Besides this process has all the limitations of PB technologies, both in terms of productivity and achievable part size.

Currently, the only OEM releasing a WAAM based hybrid machine is Mazak Table 2.4. The Variaxis J 600 AM is a 5-axis vertical milling center allowing to perform WAAM operations. Figure 2.9 shows a detail of this machine.

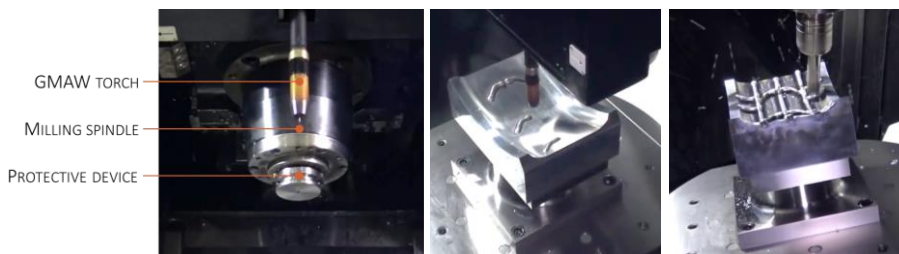


Figure 2.9: Deposition and milling end effectors of the Mazak Variaxis J 600 AM [57].

This machine uses GMAW as arc welding technology for the WAAM operations. Unlike in the Integrex I 400 AM and in the Lasertec, the deposition head is not located in a dedicated magazine. The welding torch is located on the side of the milling spindle (Figure 2.9) and it can be retracted during milling operations. Besides, a protective device can be clamped on by the milling spindle, to protect it from the intrusion of metal particles projected during the deposition, named spatter.

So far, the review of hybrid machines focused on the brand-new machines. The alternative hybridization approach is to retrofit existing machine tools. This consists in installing AM end effectors and all the required auxiliary systems on the existing machine. This approach is more economically convenient for the end-user, since exploiting an existing machine significantly reduces the investment required to acquire a hybrid technology. This approach is widely used for research purposes, such as the ArchLM hybrid machine created by Karunakaran et al. [43]. As shown in Figure 2.10, this machine fits a GMAW welding

unit on an existing milling machine. this enables to perform hybrid WAAM-milling operations without requiring a brand-new hybrid machine.

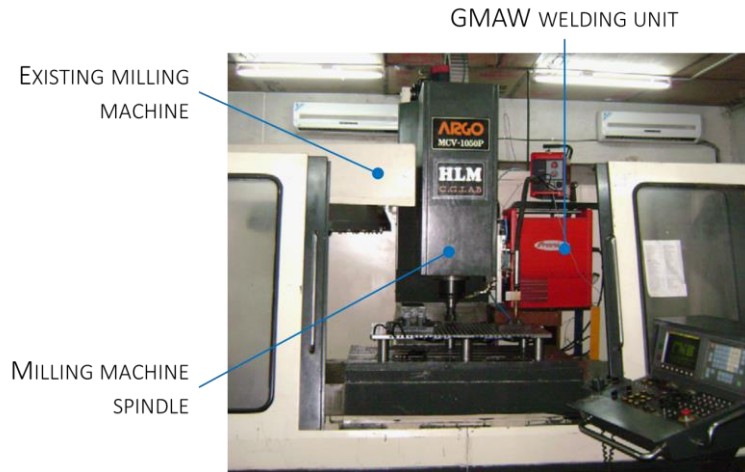


Figure 2.10: ArcHLM hybrid solution [43].

A further example of the retrofitting approach to create a hybrid machine for research purposes was shown by the Cranfield university [15]. A former friction stir welding machine is equipped with a welding unit to carry out WAAM operations, as shown in Figure 2.12 (a).

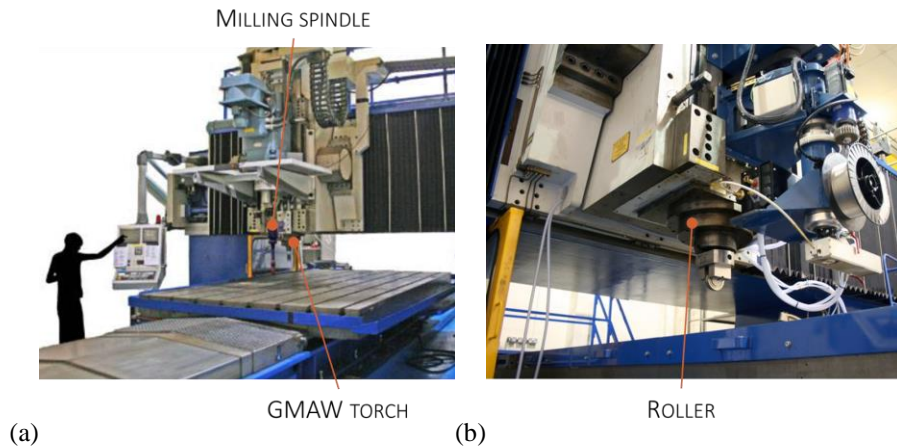


Figure 2.11: Hybrid WAAM-milling machine implemented at the Cranfield university: overall view of the machine (a) [15] and high pressure rolling system (b) [58].

Moreover the machine was fitted with a rolling system, as shown in Figure 2.12 (b). This device is used to apply a pressure load on the deposited material. This modifies its microstructure and reduces the tensile residual stresses [59] improving workpiece quality.

The retrofit approach is used also in commercial application. The company Hybrid Manufacturing Technology provides a solution in which the machine is modified to perform DMLD operations. The machine is fitted with an external laser source and powder feeding

system. Besides a software interface is created, to control the deposition process from the pre-existing milling machine NC (Numerical Control). Figure 2.13 (a) shows an example of this solution, installed on a turn-milling machine. The deposition head (AMBIT tool [60]), provided during the retrofitting, is shown in Figure 2.13 (b).

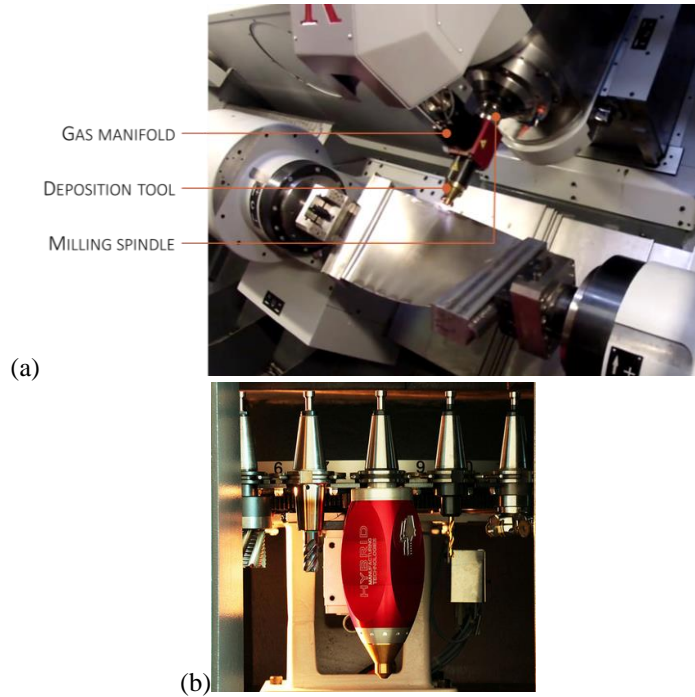


Figure 2.12: The retrofit system provided by Hybrid Manufacturing Technologies [60]: the system installed on a turn-milling machine (a) and the deposition tool (b).

This solution significantly reduces the investment required to access a hybrid DMLD-milling machine compared to the Mazak and DMG solutions. However, this solution is still not competitive with the hybrid WAAM-milling process, due to the high cost of the laser sources.

A further hybrid solution that must be mentioned is the one under development in the EU funded research project LASIMM [61]. This project proposes a different concept of hybridization: combining AM and machining in a robot cell rather than in a machine tool. The proposed layout is shown in Figure 2.13.

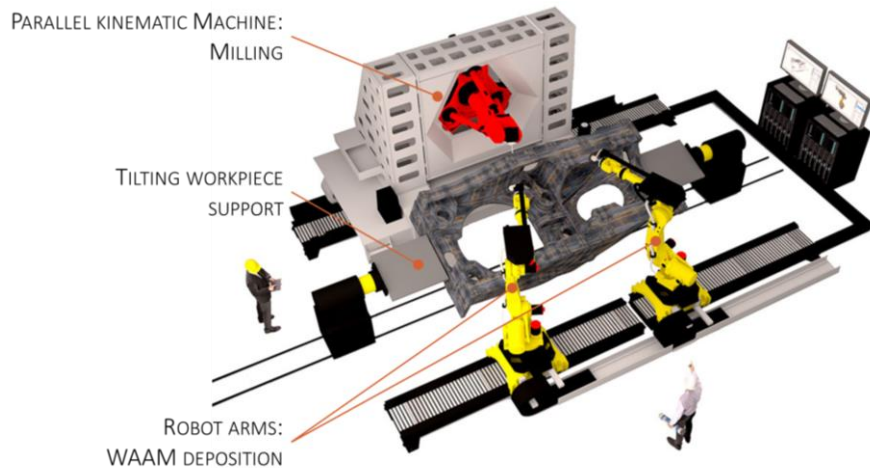


Figure 2.13: Hybrid WAAM-milling concept proposed in the LASIMM project [62].

The WAAM operations are carried out by robot arms fitted with welding equipment. The workpiece is finished by a parallel kinematic milling machine. The workpiece is fixtured on a tilting support which provides the accessibility required to perform all the deposition and milling operations without repositioning. This alternative hybridization layout is conceived to manufacture large components, not requiring a high level of dimensional accuracy. Indeed, as claimed by Bandari et al [62], the usage of robot arms is convenient when manufacturing a large components that needs to be tilted during the process. For components requiring high dimensional accuracy, the machine-tool layout is to be preferred.

This review highlights that the market of hybrid machine is taking up, with different solutions in terms of machines layout and processes. Despite DMLD process is still the most widespread one at a commercial level, WAAM is emerging as a promising alternative for hybrid machines due to its potential as a low-cost process for large metal components. Hence, further research efforts are worth to improve the performances of hybrid WAAM-milling process.

3. The WAAM process

This chapter introduces the WAAM process. It is organized in two sections:

3.1 Arc welding processes for WAAM applications: The arc welding processes used for WAAM operations are presented, discussing their advantages, drawbacks and performances. Then the main issues of this process are introduced, highlighting the most relevant researches aiming at addressing them

3.2 WAAM machine implementation: This section presents the WAAM machine used to carry out the experimental activities presented in this thesis, describing its main components and the adopted solutions.

3.1. Arc welding processes for WAAM applications

The basic principle of the arc welding process is to generate the heat required to melt both the filler and the base material by means of an electrical discharge in a gas medium [63]. The welding machine provides the power required to overcome the breakdown potential of the gas medium, igniting the arc between the workpiece and an electrode located on the welding torch. Usually, the electrode is the anode of the circuit and the workpiece is the cathode. Many different arc welding processes exist, but the most commonly used for WAAM applications are the following ones: GMAW (Gas Metal Arc Welding), GTAW (Gas Tungsten Arc Welding) and PAW (Plasma Arc Welding). Figure 3.1 presents a scheme outlining the basic working principles of the GTAW and the GMAW.

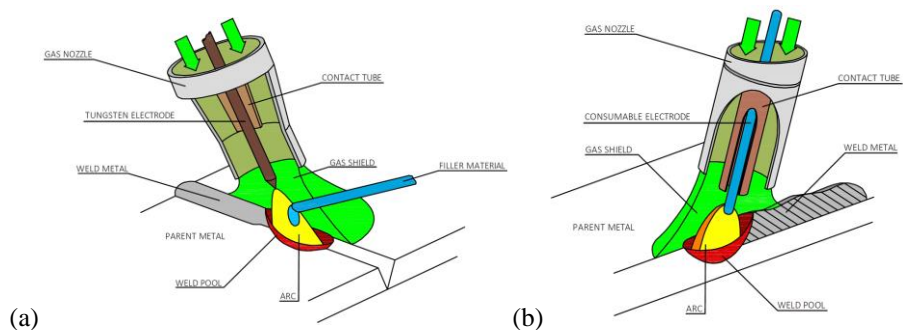


Figure 3.1: Scheme of the GTAW (a) and GMAW (b) processes.

The main difference between these two processes is the type of electrode. In GTAW, the arc current flows between the workpiece and a tungsten electrode (Figure 3.1 (a)) located on the torch. Due to its high melting point, the tungsten works as a non-consumable electrode, i.e. it is not molten during the deposition process. The filler material is supplied separately from the torch by means of a wire feeding system.

In GMAW process (Figure 3.1 (b)), the electrode is the filler material itself. A filler metal wire is conveyed to the welding torch by means of a feeding system. The wire is connected to the anode of the welding machine generator by means of a contact tube. This ignites the arc as the filler metal sticks out the contact tube. Since the electrode is made of filler material, it melts during the process, supplying the feedstock for the deposition process.

Both GTAW and GMAW require the usage of a shielding gas, to prevent an excessive oxidation of the molten pool and to increase the stability of the arc. For this reason, in both GMAW and GTAW, the electrode is surrounded by a coaxial nozzle which supplies the flow of shielding gas.

A further arc welding process suitable for WAAM applications is PAW. The main features of this technology are outlined in Figure 3.2.

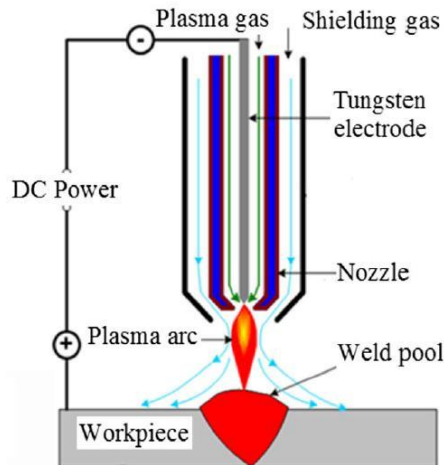


Figure 3.2: Scheme of the PAW process [16].

The PAW torch is made of two coaxial nozzles: the exterior one supplies the shielding gas while the inner one supplies the gas flow required for the plasma generation. A coaxial tungsten cathode is located inside the plasma nozzle. The anode can be the plasma nozzle itself or the workpiece. The voltage drop between the anode and the cathode ionizes the gas, creating a plasma stream which is focused by the nozzle on the workpiece surface, forming the molten pool. The filler material is supplied by an external feeder as in the GTAW process. The formation of a plasma stream occurs in every arc process [63]. However, in PAW such stream is guided and highly focused, achieving a higher energy density compared to GTAW and GMAW processes [64].

The major differences among these welding techniques are related to the stability of the arc: the processes using non-consumable electrode (GTAW and PAW) produce a more stable arc than GMAW [12,65]. This leads to a more stable transfer of the filler metal to the molten pool, reducing the spatter phenomenon and producing a more even bead [66]. A

further consequence of the improved arc stability is that GTAW and PAW allow to process a wider range of materials than GMAW. Above all, GTAW and PAW were proven to be well suited to process Ti-6Al-4V [67–69], a titanium alloy widely used in the aerospace sector for structural applications. Besides, GTAW based WAAM was used to manufacture innovative material, such as iron aluminide alloys [70].

Despite the advantages of the GTAW and PAW processes, the GMAW technique is widely used for WAAM applications [16]. Indeed, despite the reduced stability of the arc, this process has several advantages. First, both GTAW and PAW use external wire feeding, supplying the filler metal at a given orientation with respect to the arc aiming direction. This parameter has a great influence on the process since it affects layers evenness and appearance, as shown by Geng et al. [71]. Hence the wire feed orientation should be kept constant throughout the deposition, resulting in significant process planning issues when dealing with complex parts and 5-axis deposition. This problem is not present in the GMAW process, resulting in a reduced complexity of both the process planning and the machine itself. Another advantage of GMAW is the high arc efficiency compared to GTAW. This parameter is defined as the ratio between the power effectively delivered to the workpiece and to the filler metal over the consumed electrical power. In GMAW the arc efficiency ranges from 75% to 95%, while in GTAW it ranges from 20% to 80%, depending on the metal and on the shielding gas [72]. The higher efficiency of GMAW results in a higher wire melting rate hence in a higher productivity. Besides, the stability of the GMAW arc can be improved using controlled short circuit processes [73], such as STT (Surface Tension Transfer) or CMT (Cold Metal Transfer). These processes modulate the welding current according to specific waveforms capable of mitigating the spatter phenomenon with consequent improvement of the weld bead evenness.

This review of the arc welding processes for WAAM application highlights that GTAW and PAW are more suited for applications on specific materials requiring high arc stability. The GMAW process can be regarded as the most suited for general purpose applications. Based on this, the thesis is focused on the WAAM process based on GMAW welding.

To present the most relevant research fields concerning GMAW based WAAM, it is essential to introduce the general workflow of such a process, introducing the basic relations among the main process parameters. Figure 3.3 shows an example of a generic workflow required to perform a WAAM operation, highlighting the main steps and the main issues related to them.

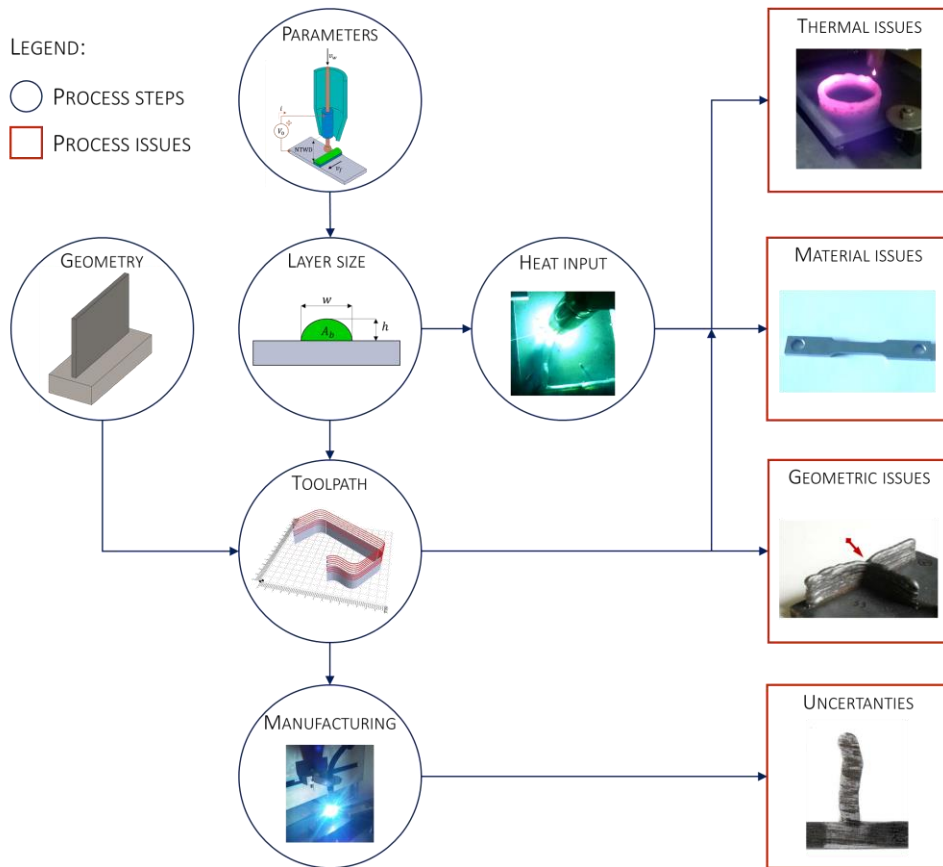


Figure 3.3: Interconnection between the step of WAAM process planning and the most common process issues.

The fundamental input of the process is the workpiece geometry, since it drives the deposition path (named toolpath in Figure 3.3) definition. However, defining the deposition path requires the knowledge of the layer size that is dependent on the process parameters as in every metal AM process. Therefore, achieving a given layers size will require a specific set of process parameters. Figure 3.4 highlights the most relevant process parameters in GMAW.

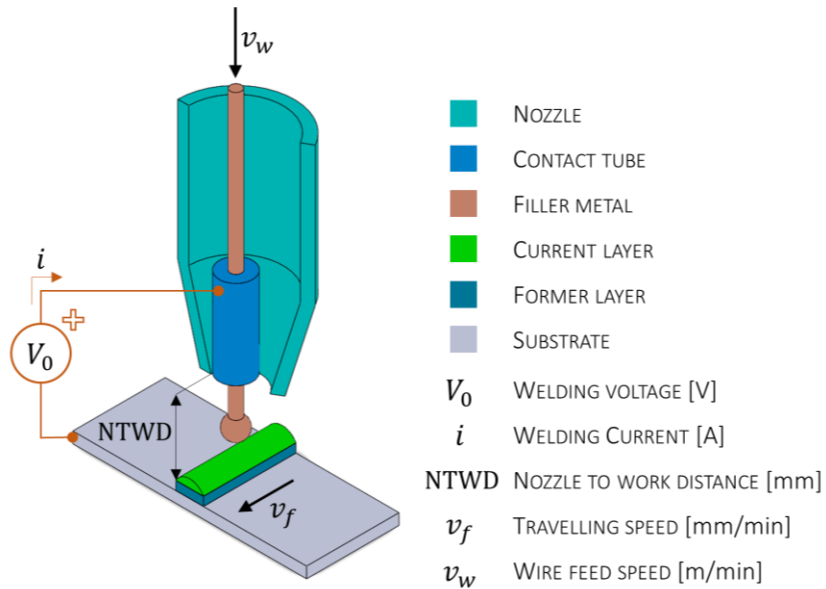


Figure 3.4: GMAW process parameters.

According to this scheme, the most relevant parameters are: the applied voltage V_0 ; the current i flowing through the arc and the workpiece; the wire feed rate v_w , i.e. the velocity at which the wire is fed through the electric contact (contact tube); the travelling speed v_f , i.e. the velocity of the torch motion during the deposition process; the NTWD, i.e. the distance between the mouth of the gas nozzle and the workpiece. As previously mentioned, these parameters determine the layer shape and dimension. Figure 3.5 shows the most relevant dimensions of a generic layer, namely its height h , width w and section A_b .

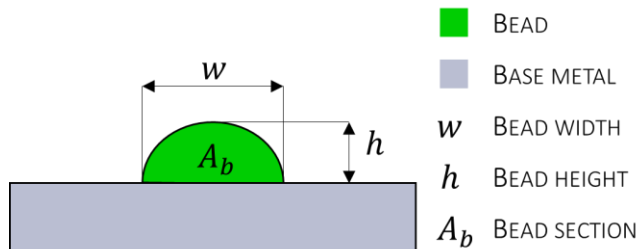


Figure 3.5: Weld bead dimensional parameters.

The area of the layer section is determined by the mass conservation of the filler material [74]. If the mass density of the filler metal is constant throughout the process and the loss of material by spatter is negligible, the volumetric balance of Eq. 2 must be satisfied:

$$A_l v_f = \pi \frac{\phi^2}{4} v_w \tag{Eq. 2}$$

Where A_l is the area of the weld bead, as defined in Figure 3.5, ϕ is the diameter of the wire, v_w is the wire feed speed and v_f is the torch travelling speed. Basically, the layer area is directly controlled by the λ parameter, namely the ratio of wire feed speed and travelling speed, as shown in Eq. 3 :

$$\lambda = \frac{v_w}{v_f} ; A_l = \lambda \frac{\pi \phi^2}{4} ; \quad \text{Eq. 3}$$

Hence given the wire feed rate and the travelling speed, the layer section is determined. To define the toolpath, it is important to predict not only the bead area but also its shape in terms of height and width (Figure 3.5). Hence, investigating the relations between layer dimensions and process parameter is an important topic in WAAM. The goal of these researches is to identify geometrical models that describes the cross-sectional shape of the weld bead, correlating the model parameters to the ones of the process. An example is the work of Xiong et al. [75] investigated the effectiveness of parabola and circle arc models for the bead geometry, finding that their accuracy depended on the value of the λ parameter. Cao et al. [75] and Ding et al. [76] tested additional geometrical models, such as cosine arc and Gaussian curve. Besides they developed techniques to predict the ideal stepover distance to overlap weld beads on the same layers to manufacture thick walls. Despite the large number of studies, a general model of the weld bead was not achieved, since the relations defining the bead shape are dependent on the specific welding machine, on the filler metal and on the shielding gas. However, it is generally accepted that the wire feed speed is directly proportional to the bead height, whilst the arc length is directly proportional to bead width. The specific relations for a given set of welding machine, material and shielding gas must be determined with by dedicated experiments.

Recalling the framework presented in Figure 3.3, the definition of the process parameters provides the layer size, which together with the workpiece geometry allows to define the deposition path. The definition of criteria and algorithms for an automated generation of the deposition path is currently an important research topic. Several works aim at identifying strategies to deal with geometrical issues of the WAAM process, occurring for specific features. An example is the layers overlapping in correspondence of crossing features. Figure 3.6 shows a WAAM component with crossing features, namely T-crossings and direct crossings.

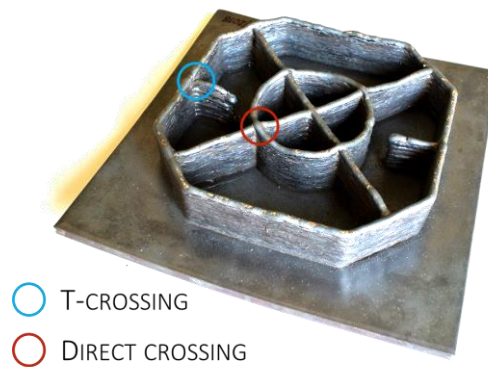


Figure 3.6: Example of WAAM part with layers crossing.

Manufacturing such features requires specific strategies to limit the increase of the layer height. Mehnen et al. [77] developed and tested strategies to deal with direct crossing features. Venturini et al. [78] carried out a similar work for the T-crossing features. A further issue in toolpath definition is the handling of the arc striking and extinguishing areas which cause non-uniformity of the layer height. An example of this issue is shown in Figure 3.7.

- ARC STRIKING: h_s
 - ARC EXTINGUISHING: h_e
 - CENTER OF LAYER: h_c
- $$h_e < h_c < h_s$$



Figure 3.7: Example of arc striking and extinguishing defects [79].

The region of the layer close to the arc ignition exhibits an excessive layer thickness with respect to the central part of the layer, due to the heat sink effect of the base metal. On the opposite, in the arc extinguishing region, the layer exhibits a reduced thickness due to the arc pressure on the molten pool. Xiong et al. [80] dealt with this issue. They investigated different strategies to compensate this effect: introducing a wire feed speed ramp-up in the arc striking and extinguishing regions and locating the arc ignition and extinguishing points in different points for subsequent layers. Besides the toolpath planning strategies aiming at coping with specific issues, several authors proposed general algorithms for an automated generation of the WAAM toolpath, based on different strategies [40,79,81].

As shown in Figure 3.3, the welding parameters determine both the bead shape and dimension and the heat input of the process. Recalling Eq. 1, in DED processes the heat input is determined by the source power and by the travelling speed. Hence GMAW the thermal power input in the workpiece can be calculated as:

$$\dot{Q} = V_a i \eta \quad \text{Eq. 4}$$

Where V_a is the arc voltage drop and η is the arc efficiency, taking into account the energy losses in the welding machine and in the arc itself [82]. It must be pointed out that in general, V_a is not equal to V_0 . The actual arc voltage drop is determined by the machine open circuit voltage V_0 and by the arc length [83]. The heat input, together with the deposition

path determines the temperature time history of the workpiece during the process, that is responsible for the occurrence of thermal issues, presented in Figure 3.8.

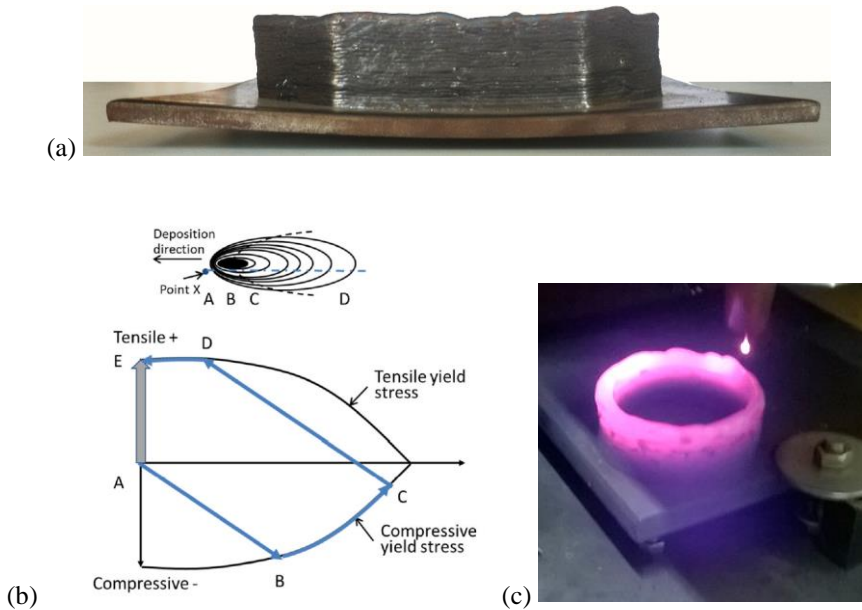


Figure 3.8: WAAM workpiece affected by distortion (a); Temperature-stress history [84], outlining the residual stresses formation principle (b); WAAM workpiece undergoing overheating (c).

During the WAAM process, the workpiece undergoes a local heating, experiencing large non-uniformities in its temperature field. This can induce severe distortions in the component, as shown in Figure 3.8 (a). Besides, these thermal deformations can lead to the occurrence of residual stresses. Figure 3.8 (b) exemplifies the principle of the residual stresses formation in a welding process, analyzing the temperature-stress history of a specific point (marked as x in Figure 3.8 (b)). As the welding torch approaches point x, the temperature increases. This causes a positive strain that results in a compressive stress state due to the presence of the surrounding material. Depending on the distance of the point x from the molten pool, the material could reach its compressive yield stress and undergo a plastic deformation. As the temperature decreases a negative strain occurs, resulting in a tensile stress. As shown in Figure 3.8 (b) this will result in a tensile residual stress. To achieve the internal equilibrium of the workpiece, the areas located further from the molten pool will experience a compressive residual stress. Currently, distortions and residual stresses are one of the most severe issues affecting the WAAM process, since they can severely limit the accuracy of the part and the strength of the material [69]. Nevertheless, these are not the only thermal issues affecting the WAAM process. As shown in Figure 3.8 (c), specific heat input conditions can lead to an overheating of the component, resulting in part structural collapse or in unevenness in the deposited layers [85].

Understanding and addressing the thermal issue is currently a crucial topic. Part of the research aims at analyzing the residual stresses distribution by experiments, assessing their magnitude and distribution for different material, process parameters and deposition path. An

example is the work of Szost et al. [69], which compared the residual stresses of Ti-6Al-4V samples manufactured by WAAM and DMLD. Other works focus on implementing techniques to mitigate the residual stresses, such as the high pressure rolling technique, proposed by Colegrove et al. [59]. An important part of the research related to WAAM thermal issues is focused on the development and application of numerical models. Many authors work on thermo-mechanical simulation techniques, aiming at predicting both distortions, residual stresses and the occurrence of structural collapse phenomenon. An example is the work of Mughal et al. [86], which investigated the effect of process parameters on the residual stresses using a FEM simulation. Zhao et al. [87] used a numerical simulation to introduce inter-layer cooling stages (idle times), analyzing their effect on residual stresses. Besides, the simulation enables to virtually test the effectiveness of residual stresses and distortion mitigation strategies, as shown in the work of Denlinger and Michaleris [88]. It must be pointed out that this is not an extensive review of the WAAM simulation techniques. Since this topic is the core one of the WAAM related research presented in this thesis, it will be extensively discussed in chapter 4.

Since WAAM is a thermal process involving material fusion and solidification, the material behavior is a crucial research topic, as shown in Figure 3.3. It is important to assess which are the process parameters set that enable to produce better results in terms of material properties. Baufeld and Van der Biest [89] investigated the anisotropy of WAAM processed Ti-6Al-4V. This study highlighted that the material has a different ductility along the layer stacking and the deposition direction (about 15% increase of ductility along the layer stacking direction), with a consequent reduction of the ultimate tensile strength in the building direction. Brandl et al. [90] investigated the static and fatigue behavior of WAAM processed Ti-6Al-4V, testing different post process heat treatment aiming at reducing the residual stresses, promoting the diffusion of segregated phases and reducing the anisotropy. It was highlighted that this post processing enables WAAM material to achieve the same performances of the cast and wrought one. Zhang et al. [91] investigated the fracture toughness of WAAM processed materials, an important aspect in several mechanical application. Besides the mechanical properties, the microstructure of the WAAM material is an important topic, in order to understand the effect of the process parameters on the strength of the WAAM processed material. For example, the works of Zhang et al. [46] and Wang et al. [92] highlighted that the workpiece can exhibit an inhomogeneous mechanical behavior (Yield strength and UTS), depending on the distance from the substrate. An analysis of grain size and phase concentration allowed to correlate this phenomenon to the different cooling rates and temperature gradients experienced by the workpiece with the increase of the number of layers. Abe and Sasahara [93] studied the deposition of dissimilar metal. The authors assessed the feasibility of combining stainless steel and a nickel based alloy in the same workpiece. It was found out that the combination did not lead to significant defects and resulted in consistent mechanical properties.

Recalling the framework presented in Figure 3.3, the definition of the toolpath enables to manufacture the selected component. A careful selection of the process parameters enables to achieve the required layer dimension, to mitigate or avoid the occurrence of thermal issues and to achieve the required material properties or to design proper post process heat treatment. However, even using accurate models or performing many pre-manufacturing experiments, the process is prone to uncertainties. Therefore, an important research field concerns the development and application of equipment to monitor the WAAM process. Usually the monitored process variables can be the bead size or the molten pool temperature. For example, Xiong et al. [94] and Doumanidis et al. [95] implemented a

vision based system capable of sensing the bead width. Besides the monitoring, these systems interact with the arc welding machine, modifying process parameters to achieve a feedback control of the layer dimension. Saeed and Zhang [96] developed a molten pool sensing system, capable of monitoring the molten pool size, dimension and temperature profile. This enables to control the solidification process, having a better insight of actual temperature gradients and cooling rate. Despite the important results achieved in these works, these techniques are currently limited to simple geometries.

A summary of the presented research fields concerning GMAW based WAAM process is given in Table 3.1, together with the references listed in this section.

Table 3.1: Summary of the main WAAM researches and examples of relevant works in the respective fields

Research topic	Example relevant works	
<i>Bead Shape modelling</i>		Xiong et al. [75]
		Cao et al. [75]
		Ding et al. [76]
<i>Deposition path generation</i>	<i>Geometrical issues</i>	Mehnen et al. [77]
		Venturini et al. [78]
		Xiong et al. [80]
	<i>Automated path generation</i>	Ding et al. [40] [79], [81]
<i>Thermal issues</i>	<i>Investigation</i>	Szost et al. [58]
	<i>Mitigation</i>	Colegrove et al. [59]
	<i>Simulation</i>	Mughal et al. [86] Zhao et al. [87] Denlinger et al. [88]
<i>Material behavior</i>		Baufeld et al. [89]
		Brandl et al. [90]
		Zhang et al. [91]
		Wang et al. [92]
		Abe and Sasahara [93]
<i>Process monitoring</i>	<i>Bead size monitoring</i>	Xiong et al. [94]
		Doumanidis et al. [95]
	<i>Molten pool monitoring</i>	Saeed et al. [96]

In light of the presented review, the WAAM research of this thesis is focused on using the process simulation to tackle the thermal issues. The final goal is to implement accurate and efficient modelling technique to support the WAAM process planning, enabling

to consider the process physics for the definition of both deposition path and process parameters.

3.2. WAAM machine implementation

This section introduces the WAAM machine prototype used to perform the experiments presented in this thesis. The presented prototype was built in the MTRL (Manufacturing Technologies Research Lab) of the University of Firenze. According to the considerations drawn in section 2.2, the machine was created pursuing the retrofit approach, i.e. modifying an existing machine tool. The machine in question is a Roland Modela MDX-40A, a three-axis milling machine. Despite the advantages of a 5-axis architecture, the purpose of the presented research is to develop, test and apply process simulation techniques. Hence, a three-axis kinematic was considered suitable for this application. Figure 3.9 shows the used milling machine.



Figure 3.9: Roland Modela MDX-40A [97].

The feed drive systems of the Modela MDX-40A are powered by stepper motors in an open loop configuration [98]. It has 300 mm of strokes along the X and Y axes and 105 mm along the Z axis and it can achieve a maximum feed rate of 3000 mm/min, fairly adequate for WAAM. The machine was reconfigured by removing the milling spindle and adding a tailored support for the GMAW welding torch.

The GMAW welding unit used to retrofit the milling machine was a Millermatic 300, manufactured by Miller. It is a traditional constant voltage GMAW machine, capable of generating DC current up to 300 A. In the final stage of this work it was replaced by an Awelco Pulsemig 250.

To enable the machine to control the GMAW unit, the NC and the motors power drives were replaced. The control selected to replace the original one was Mach3 [99], a PC based NC. Figure 3.10 shows the relevant components of the interface between Mach3 and the machine motors.

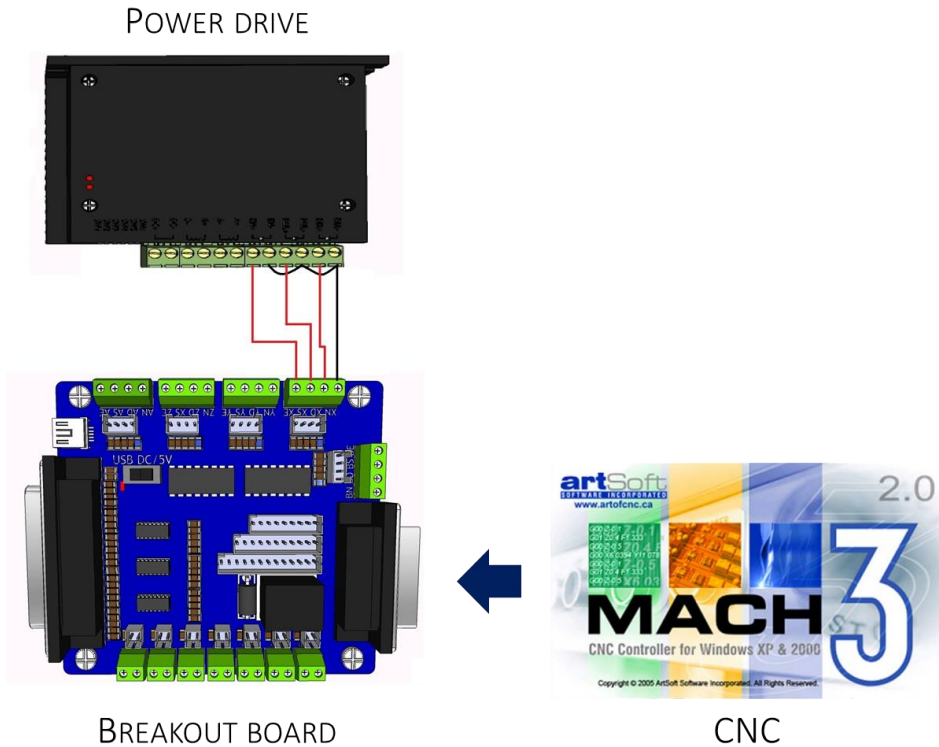


Figure 3.10: Relevant components of motors driving and control chain.

Mach 3 is interfaced with a breakout board, being the bridge between Mach 3 and the power drivers. The breakout board has a set of output pins dedicated to the motors drivers. Besides it has input pins dedicated to the limit and emergency switches. Furthermore, a set of additional input and output pins are available for additional equipment. This functionality was used to include the WAAM process in the machine.

To control the arc welding unit, the trigger switch of the torch was replaced by a relay, triggered by an output pin of the breakout board. A used defined macro was defined in Mach3 to control the welding torch relay. Furthermore, to enable a proper start of the welding process, a light sensor was installed to synchronize the axis movement with the effective arc ignition. This sensor is a photoresistor which drops down its resistivity as it is exposed to a light source. Hence the user macro prevents the axis to move if the resistivity of the light sensor is beyond a selected threshold. This ensure the synchronism between the arc and the axes movement.

The machine was fitted with additional devices to measure welding current and voltage, since measuring these values is crucial to calculate the actual power input in the workpiece. Indeed, conventional GMAW is carried out generating the arc with a DC constant voltage generator, with the electrode connected to the anode and the workpiece to the cathode. The voltage applied to the arc can be modified by controlling the open circuit voltage (V_0) of the generator. Thus the effective arc voltage (V_a) is determined by the intersection of the generator voltage/current characteristic with the electric arc one, which is

related to welding current and arc length [83]. Since the arc voltage is one of the parameters determining the transmitted power (Eq. 4), it is essential to measure it during the process. To achieve this, two wire terminals were connected to the workpiece and to the contact tube, enabling to measure the arc drop with a voltage acquisition system.

For what concerns the welding current, it is the other relevant parameter required for the calculation of the welding power input. Since the GMAW process is carried out with constant voltage generators, the current (i) cannot be directly controlled but it is a function of the applied voltage and of the arc resistance. Besides it is directly related to the wire feed speed [100]. An increase in the wire feed rate must be balanced by an increase in the wire melting rate thus requiring a higher current. To measure the actual welding current, the machine was fitted with a hall probe, returning a voltage proportional to the current intensity in the return cable. It must be pointed out that current DC welding source enable a direct selection of the welding current thanks to integrated feedback controllers [73]. However, an external measurement device provides more accurate values than the sensors embedded in the welding unit.

The full WAAM machine prototype is shown in Figure 3.11.








- | | |
|--|---|
|  1 WELDING TORCH |  2 ROLAND MODELA |
|  3 PC BASED CNC |  4 MOTOR DRIVERS |
|  5 ARC LIGHT SENSOR |  6 VOLTAGE MEASUREMENT TERMINALS |
|  7 HALL PROBE FOR CURRENT MEASUREMENT | |



Figure 3.11: Assembled WAAM machine prototype

Despite the reduced dimensions of the presented equipment, it was proven to be suitable to fit its purpose in this thesis, namely to provide actual case studies to test the process modelling techniques.

Since the WAAM machine was not given milling capabilities, workpiece finishing and the research activities related to the subtractive part of the hybrid process were carried out on a NMV1500-DCG, a 5-axis vertical milling center.

Figure 3.12 shows some demonstrator components manufactured by the developed WAAM machine prototype.

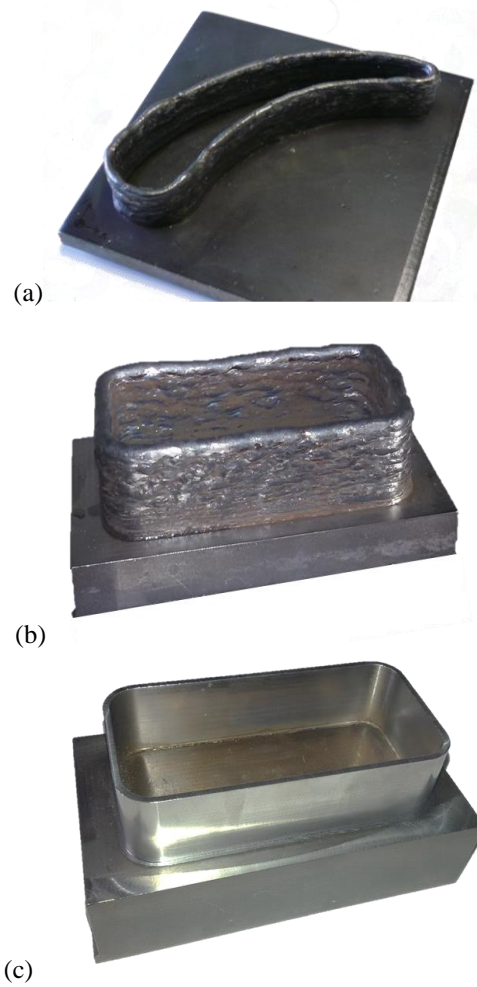


Figure 3.12: Examples of demonstrators manufactured by the implemented machine: blade-like part (a); box-like part after the deposition (b); box-like part after milling finish.

4. WAAM process simulation

The review of the researches related to the WAAM highlighted the process simulation as an effective tool to tackle the process thermal issues. Hence, a large part of the research presented in this thesis is focused on improving the WAAM simulation techniques, in terms of accuracy and of computational efficiency. This chapter is dedicated to the introduction of the developed simulation technique. First, it gives an overview of the issues arising when simulating the GMAW based WAAM process, introducing the multi-scale and multi-physics nature of the process. Then, it provides a better insight on the state of the art of the WAAM process modelling at macro scale level, that is the focus of this thesis. Finally, section 4.3 introduces the main results achieved by this thesis. The heading of this section provides a general overview of the developed modelling technique. Specific subsections provide a detailed description of the most relevant achievements: the improved heat source model, the computationally efficient technique to model the latent heat of fusion and the substrate mesh coarsening technique. These contents are arranged in sections and subsections:

4.1 Overview of WAAM simulation: introduction of the issues related to WAAM simulation.

4.2 Macro scale simulation: this section provides a better insight on the macro scale simulation, the focus of the thesis.

4.3 Proposed model: this section gives an overview of the simulation techniques used in the thesis, focusing on the materials and methods used to implement the proposed models. The innovative contributions are presented in three separated subsections.

4.3.1 Proposed heat source model

4.3.2 Proposed latent heat modelling technique

4.3.3 Substrate mesh coarsening technique

4.4 Conclusions and remarks: this conclusive section summarizes the presented contributions and draws conclusions based on the presented results

4.1. Overview of WAAM simulation

In this thesis, the final goal of the simulation is regarded as the prediction of the overall transient temperature field of the workpiece. That because the thermal history is the fundamental driver of all the relevant phenomena (e.g. material phase transformations, residual stresses, distortions) occurring in the process. To achieve this goal, the model should consider the energy and mass transfer phenomena between the electric arc, the molten pool and the workpiece. From a simulation perspective, this poses many challenges. The different physical domains involved in the process significantly interact between each other, requiring the coupling of different disciplines for a comprehensive modelling. Nevertheless, the greatest complexity is represented by the multi-scale feature of the process. Indeed, the phenomena relevant for the outcome of the process occur at different dimensional and time scales. Figure 4.2 outlines the main transfer phenomena occurring in a GMAW based WAAM operation.

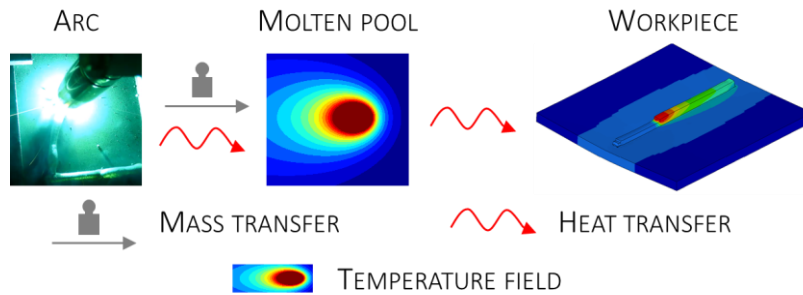


Figure 4.1: Overview of the transfer phenomena in a WAAM process

The heating action of the electric arc melts the filler and the base material, forming the molten pool. Hence, the heat generated by the electric arc is transferred to the molten pool. Moreover, a mass flow is present between the arc and the molten pool, since the filler material is transferred in form of droplets. The molten pool interacts with the surrounding workpiece material, transferring its energy by the liquid-solid interface. This heat flux determines the overall temperature field of the workpiece.

Achieving an accurate description of both the molten pool and the workpiece is a critical task. Indeed, the transfer phenomena occurring in the molten pool occurs at a far lower dimensional and time scales than the ones involving the overall workpiece domain. Figure 4.2 gives an overview of the most relevant phenomena occurring in the molten pool.

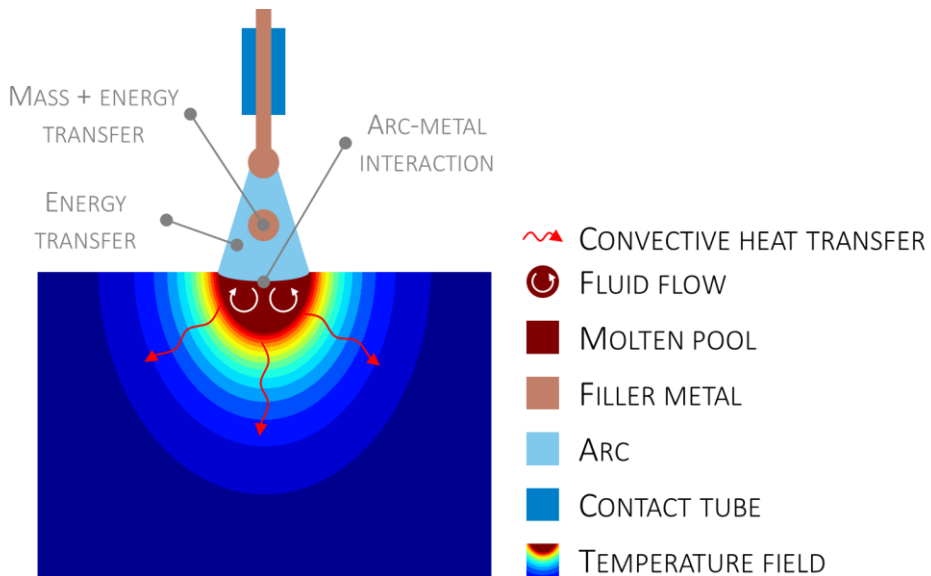


Figure 4.2: Interactions between the electric arc, the molten pool and the surrounding material

The energy generated by the arc is directly transmitted to the molten pool by means of different modes [101]: cathodic electron emission, ohmic heating and interaction of the plasma stream with its free surface. Besides, part of arc energy is not directly transmitted to the molten pool but rather through the energy embodied by the filler metal during the melting process. Indeed, the feedstock is heated by means of Ohm effect and anodic electron condensation [102]. Hence, when the metal is transferred from the wire to the workpiece, its internal energy contributes to the overall balance of the molten pool. This way, the energy embodied by the filler metal is transferred to the molten pool during the mass transfer. Hence, a detailed model of the arc-molten pool heat transfer, should include the mass transfer as well. The main issue is the difference between the time scales of metal transfer phenomena and the evolution of the overall workpiece temperature field. In WAAM applications, the metal transfer occurs according to the short circuit mode [103] that is by a periodic contact between the molten tip of the wire and the molten pool surface, in which the arc extinguish and a droplet flows in to the weld pool as a continuous liquid bridge. The time scale of this phenomenon can be quantified by the short circuit frequency, namely the average amount of droplets transferred per unit time. Usually the order of magnitude of such parameter is $1.0e^{+1} \div 1.0e^{+2}$ Hz [104]. The evolution of the overall workpiece temperature is strongly related with the torch motion in terms of velocity and position [105]. Hence the parameter determining the time scale is the travelling speed that in WAAM usually does not exceed 1000 mm/min [16]. This makes the time scale of the overall thermal history incompatible with the one of the metal transfer. A model including both these aspects should cope with simulating minutes or hours of process with time steps of $1.0e^{-5} \div 1.0e^{-4}$. This would be excessively demanding in terms of computation time.

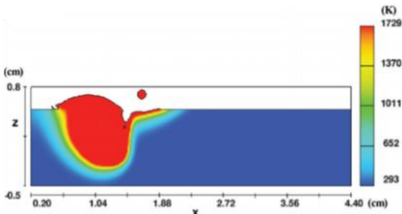
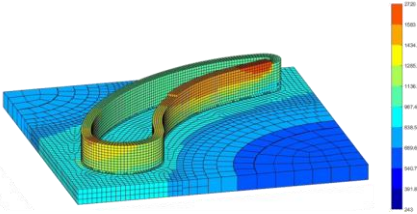
The same issue occurs for the dimensional scale, since the spatial resolution required to achieve a detailed description of the molten pool phenomena is far smaller than the one required for an analysis of the overall workpiece temperature field. As shown by Figure 4.2, the liquid metal in the molten pool is in motion due to the action of the external forces [63]:

the actions exerted by the surrounding material, the electromagnetic forces and the arc pressure [106]. Therefore, the heat transfer between the molten pool and workpiece occurs by convection at the solid-liquid interface. A detailed modelling of the convection requires the solution of the flow field in the molten pool. In common WAAM operations, the size of the molten pool is in the range of $1.0e^{+0} \div 1.0e^{+1}$ mm [107] as order of magnitude. Hence, due to the steep temperature and velocity gradients, a detailed solution of the molten pool requires a spatial discretization at least one order of magnitude smaller than the minimum molten pool size [108]. This makes inconvenient solving the molten pool and the overall workpiece behavior in the same model for computational efficiency issues.

Due to the presented issues, the molten pool and the overall workpiece thermal behavior are usually simulated separately using different modelling strategies. Hence, the process models can be classified in these two categories: micro scale models and macro scale models.

Table 4.1 summarizes the differences between the two modelling categories, highlighting their different applications and providing some example of relevant literature contributions.

Table 4.1: Goals of the micro [108] (a) and macro (b) scale simulation of the WAAM process.

Micro scale models	Macro scale models
	
Equation	
Flow field: mass, momentum, energy Electromagnetics: Maxwell, Ohm, Current	Heat conduction Solid mechanics
Solution techniques	
Multi physics CFD	FEM
Simulation results	
Molten pool temperature field Molten pool field of motion Electromagnetic field	Overall temperature field Residual stresses and deformations
Applications	
Molten pool and bead size prediction [109]	Mitigation of Stresses and distortions [110]
Metal transfer improvement [111]	Avoidance of structural collapse
Prediction of deposition defects [108]	Phases content and distribution [112]

The micro scale models aim at giving a detailed description of the molten pool behavior, limiting the analysis to a small portion of the workpiece. On the opposite, the purpose of macro scale models is to simulate the overall behavior of the workpiece, simplifying the phenomena that occur in the molten pool.

Micro scale models involve the solution of the flow field of the molten pool, of metal transfer and arc dynamics. It must be pointed out that the behavior of the molten pool generated by the GMAW arc is essentially the same, whether dealing with welding or WAAM operations. Therefore, the micro-scale simulation of the WAAM process can be effectively performed using the techniques developed for GMAW welding. Hu and Tsai [109,113] proposed a coupled model of the GMAW arc and molten pool. This model solved the coupled flow field and electromagnetism equations. This provided a detailed description of the metal transfer (droplet size, temperature and detachment frequency) and of the molten pool behavior. The same authors used this model to identify the equilibrium wire feed speed, allowing to achieve a stable GMAW arc [111]. Cho and Na [108] developed a molten pool model of the laser assisted GMAW process with the aim of identifying process parameters sets suitable to avoid the formation of defects. Fan and Kovacevic developed a micro scale model that enables to predict the size and the shape of the weld bead, simplifying the assessment of the process parameters.

The macro scale models neglect the presence of a fluid region in the vicinity of the arc. The heat transfer between the arc and the workpiece is included introducing a heat source model, i.e. a tailored boundary condition to deliver the GMAW heat input. The temperature field is calculated by solving the heat conduction equation in transient regime by means of a FE (Finite Element) solver. Moreover, the heat conduction problem can be coupled with the mechanical equilibrium one, calculating the workpiece displacement, stress and strain fields. The most common application of this type of models is the identification of the workpiece residual stresses and deformations. An example is the work of Ding et al. [110], which developed a coupled thermo-mechanical simulation of the WAAM process tailored for the large multi-layer parts. The aim of this work was to develop a modelling strategy that enabled a significant reduction of the computation time when dealing with this type of components. Denlinger and Michaleris [88] used a coupled FEM thermo-mechanical model to test a strategy to mitigate the distortions of large components. The prediction of the residual stresses and distortions is not the only possible application for the macro-scale simulation. An example is the work of Chiumenti et al. [112], which developed a FEM thermo-mechanical simulation of the WAAM process that included a phase transition model tailored for the Inconel 718 nickel based alloy. This model enabled to calculate the distribution and concentration of the solid phases in the final workpiece, providing a better insight on the expected mechanical properties. Besides, a hot cracking susceptibility criterion was implemented in the FE model. This enabled to assess the risk of the occurrence of such defect, providing a useful support for the definition of the process parameters. Furthermore, by the mere knowledge of the temperature time history it is possible to assess the risk of workpiece collapse due to its overheating.

The micro and macro scale models analyze different aspects of the WAAM process. Hence, such models serve different purposes: micro scale modelling is well suited to investigate the dependency of molten pool dynamics and bead shape on the process parameters, whereas the macro scale model is well suited to simulate the entire manufacturing process, addressing the thermal issues occurring at the dimensional scale of the overall workpiece. However, it is worth to notice that some authors proposed multi scale modelling strategies. Micro and macro scale models of the DMLD process, which has the

same criticalities in terms of dimensional and temporal scales mismatch, were integrated in a single simulation. Nie et al. [114] coupled a micro and macro scale model of the DMLD process of Inconel 718. The different scales were coupled by means of temperature boundary conditions at the solid liquid interface. A similar approach was pursued by Vogel et al. [115].

Despite the scientific and industrial relevance of a comprehensive process simulation, many issues of the WAAM process can be effectively tackled by the sole macro scale models having a higher computational efficiency. Indeed, the literature provides a large number of examples in which the macro scale simulation has been a fundamental tool to simplify the process planning and improving the quality of the WAAM processed parts. Therefore, this thesis focuses on the macro scale simulation of the GMAW based WAAM process.

4.2. Macro scale simulation

This section introduces the macro-scale simulation of the WAAM process. First, the problem is formalized, introducing the fundamental concepts. Then the most common simulation strategies and assumptions will be depicted, highlighting the advantages and disadvantages of the state of the art techniques.

This section requires a premise concerning the state of the art. Most of the techniques used in the simulation of the WAAM process were originally developed for the simulation of the multi-pass welding operations [116] due to the similarities of these processes. Therefore, some works cited in the review are part of the welding literature rather than the AM one. Furthermore, at a macro scale level, the techniques using for the WAAM simulation are much alike the ones used for other DED processes, such as DMLD and EBF. Therefore, some references are works not directly related to WAAM.

As stated in the previous section, the macro scale models look at the overall workpiece dimensional scale, simplifying the transfer phenomena of the molten pool. The goal of the simulation is to determine the evolution of the temperature field during the process, since it controls the magnitude and distribution of residual stresses and distortions. Hence, two main physical domains are involved in the analysis: the heat transfer and the solid mechanics. The heat transfer problem can be formalized according to the heat conduction equation in a solid continuum [117]:

$$\nabla(\lambda(T)\nabla T(x, y, z, t)) + q(x, y, z, t) = \rho C_p(T) \frac{\partial T(x, y, z, t)}{\partial t} \quad \text{Eq. 5}$$

Where: T is the unknown temperature, a function of time t and position x, y, z over the integration domain; $\lambda(T)$ is the workpiece thermal conductivity, which can be introduced as a temperature dependent parameter; $C_p(T)$ is the temperature dependent heat capacity; ρ is the mass density. The term $q(x, y, z, t)$ is the source term of the equation, which can be introduced to model the power input of the process. It is highlighted that this term depends both on the time and on the spatial coordinates. This is because the power input is related to the deposition path. This term of the equation will be further discussed later in this section. Eq. 5 highlights that solving the heat transfer problem in general requires the solution of a non-linear transient differential equation. This must be integrated both over time and the workpiece volume, using the boundary conditions presented in Eq. 6:

$$\begin{cases} -\lambda(T) \frac{\partial T}{\partial \vec{n}} \Big|_{\Omega,t} = h(T - T_\infty) \\ -\lambda(T) \frac{\partial T}{\partial \vec{n}} \Big|_{\Omega,t} = \varepsilon \delta (T^4 - T_\infty^4) \\ T|_{x,y,z,0} = T_0 \end{cases} \quad \text{Eq. 6}$$

The first two relations represent the boundary conditions of convection and radiation to environment respectively. The convection is described by the Newton’s law, where h is the heat transfer coefficient, T_∞ is the far field air temperature \vec{n} is the normal vector of the heat transfer surface Ω . The radiation is described by the Stefan-Boltzmann law where ε is the surface emissivity and δ is the Stefan-Boltzmann constant. The third relation represents the initial condition of uniform temperature T_0 throughout the integration domain.

The second relevant domain involved in WAAM macro-scale simulation is the mechanical one. The problem can be formalized according to the equilibrium equations of deformable continuum [118]:

$$\begin{cases} \nabla \sigma = 0 \\ \sigma = \sigma^T \end{cases} \quad \text{Eq. 7}$$

Where σ is the stress tensor. It must be pointed out that Eq. 7 neglects both the inertial terms. This is because the mechanical problem can be regarded as a quasi-static one without introducing significant errors [119]. Besides, the body force term of the equation is neglected. The equation is solved in terms of displacements by introducing the constitutive laws of the workpiece materials (substrate and filler).

The heat transfer and the mechanical domains interact, leading to a coupled thermo-mechanical problem. Figure 4.3 outlines these interactions [84].

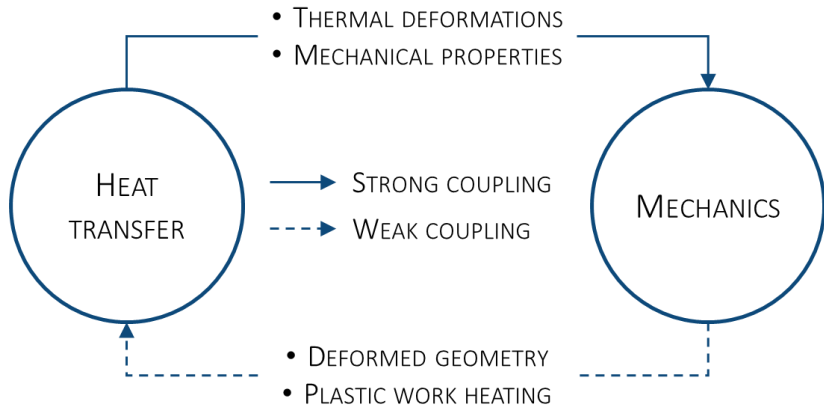


Figure 4.3: Interaction between the heat transfer and the mechanical domain in macro scale models.

As highlighted in Figure 4.3, each domain influences the other. However, the coupling of the heat transfer with the mechanics is stronger than the vice-versa. Namely the

temperature field represents the main input of the mechanical one. The temperature variations result in thermal deformation of the workpiece according to Eq. 8:

$$\varepsilon_T = \alpha(T)dT \quad \text{Eq. 8}$$

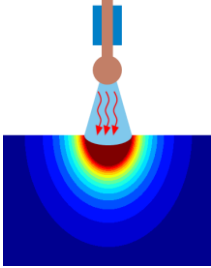
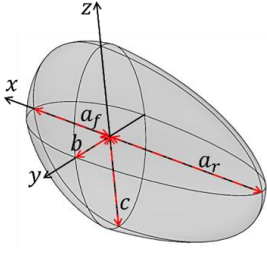
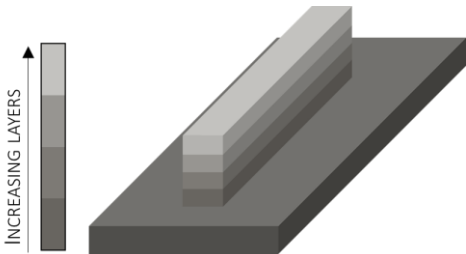
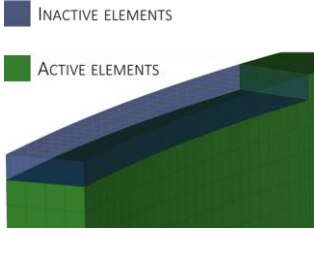
Where ε_T represent the generic term of the strain tensor; $\alpha(T)$ is the temperature dependent thermal expansion coefficient and dT is the temperature variation. Eq. 8 shows that the solution of the heat transfer is mandatory to solve the mechanical problem, since the temperature field represents the main external load. Moreover, the temperature influences the mechanical properties of the material: the elastic modulus, the Yield stress and the plastic flow curve. Due to the large temperature variations experienced by the workpiece, the temperature dependence of the mechanical properties cannot be neglected, as shown by Zhu and Chao [120].

In light of what discussed, the mechanical problem cannot be solved without the heat transfer one. On the opposite, the influence of the mechanical problem on the heat transfer one is weaker (Figure 4.3). The first aspect is the heat generation due to the plastic deformations. This could potentially affect the results of the heat transfer analysis. However, this heat generation is negligible if compared to the heat generated by the GMAW process. The second aspect is that the thermal deformations modify the geometry of the integration domain, with a potential influence on the heat transfer problem. However this aspect is usually neglected in the WAAM simulations [84].

Hence, the solution of the WAAM macro scale problem can be regarded as a weakly coupled thermo-mechanical problem, in which the heat conduction problem can be solved independently of the mechanical one. On the opposite the equilibrium equation requires the input by the heat transfer problem.

The most distinctive aspects of the macro-scale modelling of the WAAM process are the modelling techniques used to the mass and heat input into account. Table 4.2 outlines the solutions commonly used to tackle these issues.

Table 4.2: Strategies used in macro-scale simulation to model energy and material input.

Real process	Macro scale simulation
<p data-bbox="408 305 518 330">Heat input</p> 	<p data-bbox="865 305 1075 330">Heat source models</p> 
<p data-bbox="358 614 568 639">Material deposition</p> 	<p data-bbox="806 614 1134 639">Elements activation algorithms</p> 

As briefly introduced in Eq. 5, the heat input of the welding process is usually included by using a heat source model. This approach consists in introducing a source term in the heat transfer equation or in prescribing a tailored boundary condition to simulate the power input of the welding process. This technique allows to consider the heat input without modelling the complex interaction between the arc and the workpiece, thus treating the problem as the heat conduction in a solid body. Over time different heat source models were proposed, involving different levels of modelling complexity, depending on the functions used to model the heat flux [121]. This aspect will be discussed in detail in section 4.3.1.

The other distinctive aspect of the WAAM simulation is the material deposition modelling (Table 4.2). In every AM process, the workpiece is built by progressively adding material, thus transferring mass to the workpiece. Hence the integration domain modifies its shape and volume along the simulation process. As shown by Chiumenti [112], taking this aspect into account is crucial for simulation accuracy, both in the heat transfer and in the mechanical analysis. Since a detailed modelling of the material deposition physics is out of the scope of macro scale simulations, this aspect is taken into account by means of the elements activation techniques [122]. Basically, an algorithm is used to progressively introduce the finite elements representing the filler material according to the deposition process.

The macro scale simulation of the welding and DED processes is a well-established practice, providing valuable and accurate results, as shown in the beginning of this chapter (Table 4.1). In light of this, the aim of the thesis is not to develop a radically different simulation technique. On the opposite, it proposes enhancements to the existing techniques to improve the accuracy and most of all the time efficiency of the WAAM macro scale simulation. This is a hot topic both for research and industry. Indeed, for all the DED

processes, the long calculation time is still an issue that limits the diffusion of simulation among the manufacturing companies. Thus, the goal is to identify the main computational leverages that enable to reduce the simulation time, without excessive loss in both simulation accuracy and details. To achieve these goal, this thesis proposes three main enhancements to the current simulation techniques, which will be detailed in the following sections:

- A heat source model tailored for GMAW based WAAM process.
- A computationally efficient model to include the latent heat of fusion
- A mesh coarsening technique to reduce the number of element required for the substrate discretization

4.3. Proposed model

This section describes the contribution of the thesis to the state of the art of WAAM macro-scale modelling. The section is arranged as follows: the heading provides a general overview of the modelling technique, describing the aspects drawn from the state of the art. Then, three sub-sections are dedicated to the contributions of this thesis:

Sub-section 4.3.1: describes the proposed heat source model.

Sub-section 4.3.2: describes the proposed latent heat model.

Sub-section 4.3.3: describes the proposed mesh coarsening technique.

WAAM macro scale simulation is essentially a FEM transient thermo-mechanical analysis. It is a non-linear problem both for what concerns the thermal and the mechanical side. The non-linearity is due to the need of considering the temperature dependence of material properties and to the material plastic behavior. Despite the complexity of the problem, current commercial FE solver enable to carry out such calculations. This thesis uses the commercial FE solver LS-DYNA to implement the WAAM model. This software enables to perform fully coupled thermo-mechanical calculations. In this thesis the transient thermal simulations were carried out using a Crank-Nicholson time integration scheme, whereas the mechanical ones were carried out using a fully implicit method. Both thermal-only and coupled thermo-mechanical calculations were undertaken. Since in LS-DYNA the thermal and the mechanical solvers operate independently, in coupled simulations they must be forced to be synchronized. This was achieved by means of the *CONTROL_IMPLICIT_AUTO functionality [123]. Since both the thermal and the mechanical problems are non-linear, each iteration is carried out by means of an iterative solution based on the Newton-Raphson method.

The workpiece is discretize using three dimensional hexahedral elements. The heat transfer problem is solved using elements with a single Gauss integration point. On the opposite, the mechanical solution fully integrated elements with 8 Gauss points. An example of a FE model of a WAAM workpiece is shown in Figure 4.4 (a).

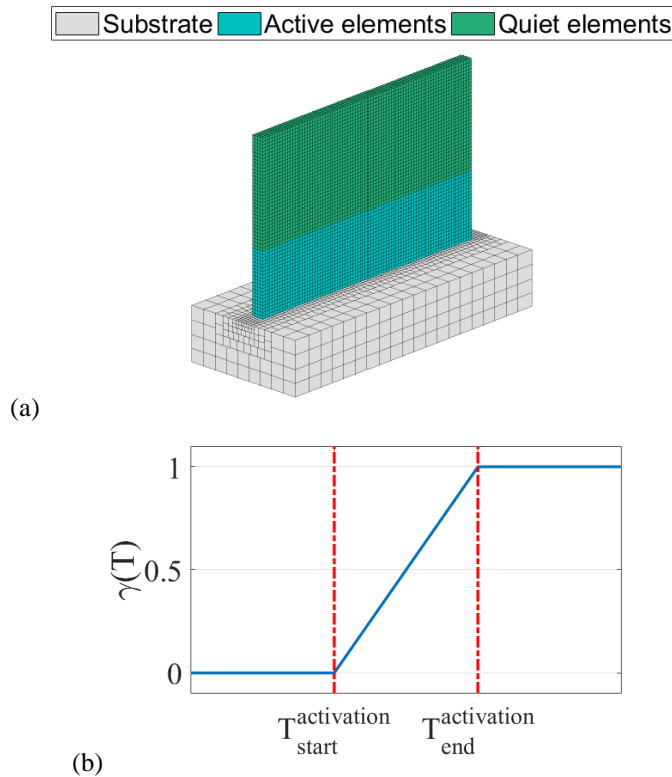


Figure 4.4: WAAM simulation model highlighting active and inactive elements (b) pattern of the generic γ function used for element activation.

As earlier mentioned, an important aspect of the WAAM simulation is modelling the material deposition. According to the state of the art this can be achieved using two different techniques [122]: the inactive element method and the quiet element method. In both techniques all the workpiece is initially discretized, including the deposited material. However, in the inactive element method, the elements representing the filler are not included in the analysis at the simulation start. To emulate the actual deposition process they are progressively introduced according to the torch travelling path. On the opposite, in quiet element method all the elements are present since the beginning of the simulation, but they are assigned quiet material properties (i.e. low thermal conductivity and Young's modulus) to emulate their absence. Their material properties are then switched to their actual values according to the deposition process. Figure 4.4 (a) shows an example of quiet and active elements during the deposition of a wall.

Michaleris [122] compared the two techniques, stating that the quiet element method improves the simulation convergence and returns accurate results, provided that the quiet value of the thermal conductivity is reduced of at least $1.0e^{-5}$ times its room temperature value. Hence this thesis uses a technique borrowed by welding simulation literature [124], based on quiet element strategy. In the thermal analysis, the technique is implemented acting on the material thermal conductivity: at the initial state, an extremely low value is assigned to the thermal conductivity of the elements representing the weld layers; such property is

then raised to its actual value when the elements temperature crosses a threshold value. This is effective since the low thermal conductivity of the quiet elements does not allow any heat transfer between the quiet and the active elements, making the contribution of the former ones negligible to the thermal behavior of the base material. Besides the quiet elements experience a significant temperature increase only when they are directly heated by the heat source, making the activation sequence consistent with the actual deposition process.

The presented technique is implemented in the FE solver using the Eq. 9 to define material thermal conductivity:

$$\lambda(T(\tau)) = \gamma(T_{max})\lambda_{act}(T(\tau)) + (1 - \gamma(T_{max}))\lambda_{quiet} \quad \text{Eq. 9}$$

Where λ is the thermal conductivity, function of the temperature T at the current simulation time τ ; λ_{act} and λ_{quiet} are the active and quiet values of the thermal conductivity; γ is the activation variable, function of T_{max} , i.e. the maximum temperature experienced by the element up to the current simulation time. The pattern of $\gamma(T_{max})$ is shown in Figure 4.4 (b): the activation is performed in a temperature range to avoid convergence issues in the FE simulation. In this thesis the activation start and end temperature are set according to the solidus and liquidus temperatures respectively. It must be pointed out that the element temperature is evaluated at the elements integration points. Hence Eq. 9 is evaluated for every time step at every integration point of the deposited material elements. For this reason, the elements activation routine must be included in the material model. In this thesis this was achieved by means of an LS-DYNA user subroutine (*MAT_THERMAL_USER_DEFINED). This enabled the implementation of both the activation technique and the new latent heat model.

For what concerns the mechanical analysis, the elements activation is simulated by means of the LS-DYNA standard material model dedicated to the welding simulation (*MAT_CWM [123]). This model uses the same activation technique presented for the thermal analysis. The main difference is that it acts on the Young's modulus, the Poisson's ratio and on the thermal expansion coefficients. In this thesis the quiet values of mechanical properties were set using the same threshold of the thermal ones, except for the Poisson's ratio which is set to 0.35 when the material is in the quiet state. This value is selected since reducing the value of the Poisson's ratio for the quiet material does not reduce the influence of the quiet elements on the active ones. Therefore, it is preferable to set its quiet value, close to the active one at high temperature, preventing the convergence issues due to sudden variation of this parameter [125]. For what concerns the activation temperatures, the same values used in the thermal calculation are used for the mechanics.

An important aspect to be depicted is the material behavior. As earlier mentioned, in WAAM the workpiece experiences significant temperature variations during the manufacturing process. Therefore, the temperature dependence of both thermal and mechanical properties cannot be neglected. In this thesis, two materials were considered in WAAM simulation: the S235JR, a mild steel used as substrate material, and the ER70S-6, a standard filler metal dedicated to mild steel welding. Both materials are low carbon content mild steel. Therefore the temperature dependent properties of both S235JR and ER70S-6 are drawn from the technical literature as the properties of a mild steel [126]. Figure 4.5 shows both the heat capacity and the thermal conductivity curves.

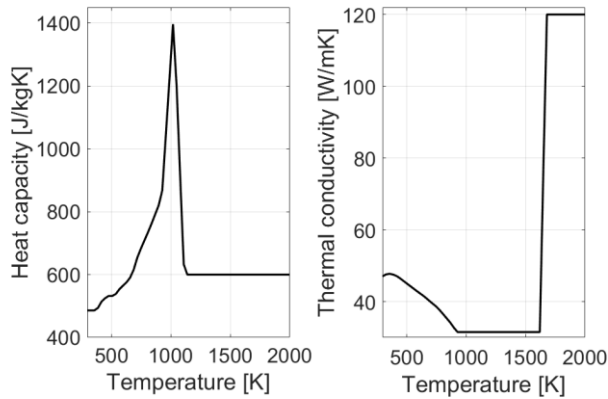


Figure 4.5: Thermal properties used in the WAAM simulation

The high value of the thermal conductivity at high temperature is due to an artificial raise. In welding simulation literature it is a common practice [127], since it allows to emulate the convective heat transfer occurring in the molten pool. Hence the actual conductivity of the liquid metal is set to about 5 times its room temperature value above the liquidus temperature.

Since in WAAM the material undergoes both fusion and solidification, it is important to include the phase transition effect in the thermal model. The material properties that characterize such phenomenon are: the solidus temperature, the liquidus temperature and the latent heat of fusion. For both ER70S-6 and S235JR, these parameters were extracted from literature works [128,129]. Table 4.3 shows their values.

Table 4.3: Solidus temperature, liquidus temperature and latent heat of fusion of the selected materials

	T_{sol} [K]	T_{liq} [K]	h_{lat} [J/kg]
S235JR	1603	1796	$222.1e^{+05}$
ER70S-6	1586	1783	$221.9 e^{+05}$

The mechanical behavior of both material is modelled as homogeneous, isotropic elastic-plastic. For what concerns the plastic behavior, the strain rate effect on the flow stress is neglected, according to a common practice in welding and AM simulation [130]. The work hardening effect is neglected as well, considering an elastic perfectly plastic material. This approximation is reasonable since in WAAM the plastic deformation occurs at high temperature where work hardening is usually negligible. It is worth to notice that several researchers propose more complex model of the material mechanical behavior. For example Chiumenti et al. introduced a viscous behavior at high temperature [112]. Denlinger [131] proposed a model that considers the stress relaxation effect to improve the accuracy of the residual stresses prediction. However, such models require the user to supply a larger number of input parameters. Besides a proper set up requires a fine-tuning of the material parameters. Thus, an accurate material model is meaningful to tailor the simulation for a specific material. The goal of this thesis is to propose improvements to the current simulation

technique independently on the processed material. Hence a simpler material model suitable to achieve the purpose.

As for the thermal properties, the temperature dependent mechanical properties were extracted from literature [126,132]. Figure 4.6 shows the temperature dependent material properties.

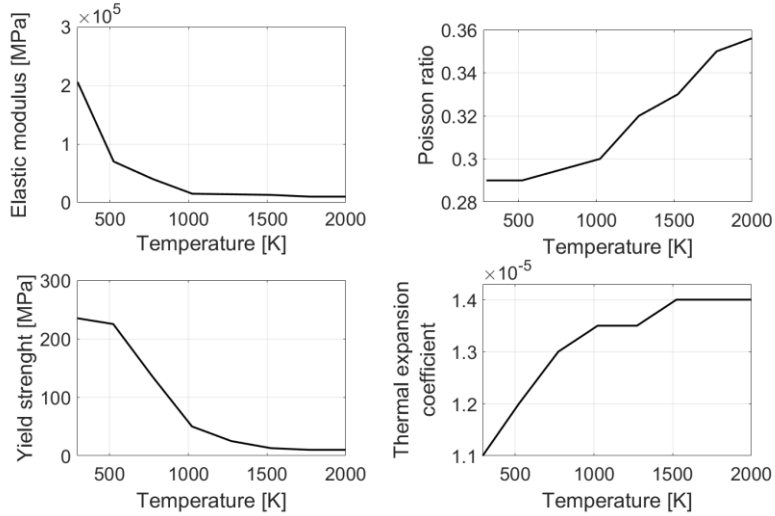


Figure 4.6: Mechanical properties used in the WAAM simulation.

Recalling Table 4.2, a further important aspect of the WAAM macro-scale simulation is the heat source model. This will be discussed in detail in sub-section 4.3.1. However, a short premise is due to introduce the implementation of the different heat source models in the finite element code. As briefly introduced in section 4.2, the heat source is a heat generation or a boundary flux condition, prescribed to simulate the energy transfer from the arc to the workpiece. This is achieved by introducing time and position dependent boundary conditions. The time dependence is introduced since the thermal power is delivered in the current position of the welding torch. Therefore, the generic heat source will be a function defined in a local frame of reference, as shown in Eq. 10

$$H_s = H_s(x(t), y(t), z(t)) \tag{Eq. 10}$$

Where H_s is the generic heat source function and x, y, z are the local axes, defined according to Eq. 11:

$$\begin{Bmatrix} x \\ y \\ z \end{Bmatrix} = R(t) \begin{Bmatrix} X - X_o(t) \\ Y - Y_o(t) \\ Z - Z_o(t) \end{Bmatrix} \tag{Eq. 11}$$

In this relation $R(t)$ is a time dependent rotation matrix; X, Y and Z are the global axes of the model, i.e. the fixed frame of reference where the mesh topology is defined; $X_o(t), Y_o(t)$ and $Z_o(t)$ are the time dependent global coordinates of the local system origin.

The local frame of reference is usually defined based on the deposition path, as shown in Figure 4.7.

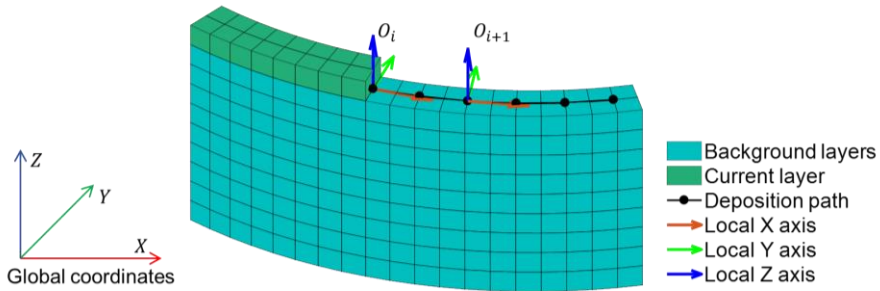


Figure 4.7: Local coordinate system used for the heat source definition.

The local X axis (x) is oriented according to the feed direction. The local Z axis (z) is oriented according to the arc aiming direction. The local Y axis (y) is defined according to the right-hand rule. Based on this, the position of the origin (O_i and O_{i+1} in Figure 4.7) is introduced by means of time dependent functions ($X_o(t)$, $Y_o(t)$, $Z_o(t)$) which are calculated in pre-process from the toolpath using a Matlab script. The same applies to the rotation terms of the rotation matrix. All the time dependent functions are introduced via the *DEFINE_FUNCTION_TABULATED feature of LS-DYNA [123]. Such functions are then called by the heat source function, implemented via the *LOAD_HEAT_GENERATION features, to perform the global to local coordinate transformation when evaluating the heat source at the current simulation time and integration point. This process is summarized in Figure 4.8.

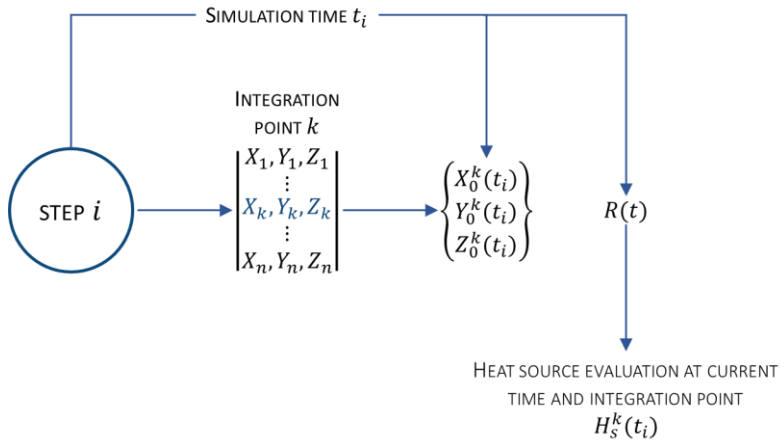


Figure 4.8: Scheme of the procedure used to evaluate the heat source function.

This is a general overview of the modelling techniques used in this thesis. The following sub-sections will depict the specific research contributions to the state of the art of WAAM macro scale modelling.

4.3.1. Proposed heat source model

The first introduction of the moving heat source is own to Rosenthal [133]. This work proposed an analytical solution to the heat conduction problem in a semi-infinite solid, in presence of a point shaped heat source moving at constant velocity along a straight path. Besides the geometrical limitation of the analytical approach, the main issue of this model is that the solution leads to infinite temperature value in correspondence of the heat source. Therefore, it is not accurate in the vicinity of the molten pool. To overcome this issue Pavelic [134] proposed a two dimensional model, i.e. a boundary heat flux distributed according to a Gaussian curve in moving frame of reference. This model is still used today when simulating welding operations of thin plates. The most widespread heat source model is the one proposed by Goldak et al. [135]. This is a three-dimensional model, i.e. the welding heat input is distributed over a volume to better reproduce the interaction of the arc and the molten pool. The heat input is delivered over a moving double ellipsoid region according to a Gaussian distribution. This pattern enables to correctly model the shape of the weld pool. However, this heat source model prescribes an upper bound to the maximum mesh size, requiring a minimum number of elements to discretize the weld bead [121]. To overcome this issue, Chiumenti et al. [112] proposed a three-dimensional heat source model using a constant power distribution. Despite the accurate results presented in this paper, this model requires investigations to be applied in practical WAAM simulations. Table 4.4 summarizes the state of the art of the heat source models.

Table 4.4: Summary of the state of the art solution regarding the heat source models.

Heat source	
<i>State of the art</i>	
	Double ellipsoid heat source model:
Goldak et al.[135]	Increase in simulation accuracy
	Constant power heat source:
Chiumenti et al. [112]	Increased simulation efficiency

Despite the wide applications of the Goldak model it has a significant drawback: it does not consider the correct heat distribution between filler and base material. This is responsible for inaccuracies in the estimation of the temperature field and consequently of the component final distortions.

This thesis proposes a novel definition of the heat source tailored for GMAW based WAAM operations. The proposed model is a modified version of the Goldak one, providing a more realistic distribution of heat input between the filler and the base material. In the following paragraphs, the Goldak model is discussed highlighting its criticalities. Proposed simulation technique and heat source model are then presented. Finally, the measured distortion of a test case component, manufactured by means of WAAM process, are compared with FE results obtained with the proposed and the Goldak heat source models.

Double ellipsoid model

The Goldak model prescribes a Gaussian distributed heat generation per unit volume defined in a moving frame of reference, shown in Figure 4.9: x axis is oriented in the feed direction, z axis in the arc aiming direction and y is defined according to the right-hand rule.

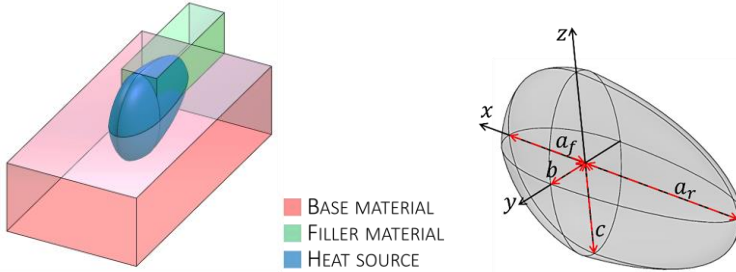


Figure 4.9: Goldak double ellipsoid model

Basically, two different power distribution functions are defined for positive and negative x semi axes, allowing to model asymmetries in heat distribution over the molten pool. Eq. 12 shows the power density distribution functions:

$$\dot{q}_v = \frac{6\sqrt{3}\dot{Q}}{\pi\sqrt{\pi}a_{f,r}bc} \exp\left[-3\left(\frac{x^2}{a_{f,r}^2} + \frac{y^2}{b^2} + \frac{z^2}{c^2}\right)\right] \quad \text{E q. 12}$$

Coefficients $a_{f,r}$, b and c are the semi axes of two ellipsoids centered in the origin of the moving frame of reference, as shown in Figure 4.9. The double subscript for the parameter a means that different values are used depending on x sign (a_f if positive and a_r if negative) leading to two different functions. The ellipsoid surface represents the space region where the power density falls to 5% of its peak value. Usually the value of ellipsoids semi axes is set according to molten pool dimension [136]. The terms $f_{f,r}$ are the distribution factors, having different values for the frontward and backward ellipsoids, provided that the following condition is fulfilled [135]:

$$f_f + f_r = 2 \quad \text{E q. 13}$$

\dot{Q} is the heat input per unit time and it is computed as the product of welding current, welding voltage and arc efficiency, as described by Eq. 14:

$$\dot{Q} = \eta i V_a \quad \text{E q. 14}$$

Integrating the two power density functions in spatial coordinates returns the total energy input per unit time generated by the heat source. According to Goldak, this integration returns the following result [135]:

$$\int_{-\infty}^{+\infty} \int_{-\infty}^{+\infty} \int_{-\infty}^{+\infty} \dot{q}_v(x, y, z) = 2\dot{Q} \quad \text{E q. 15}$$

According to this model, the actual power transmitted to the workpiece depends on the relative position between the heat source frame of reference and the base material. If such origin is positioned on the top surface of the base material, as shown in Figure 4.9, the heat input is transmitted both to the base and filler material. According to Eq. 15 transmitted power will be higher than the actual process heat input \dot{Q} . This might lead to severe overshoots in molten pool temperature. On the contrary, positioning the origin on the top the filler material would be correct for what concerns the transmitted power, but most of the heat will be delivered to the filler metal, resulting in a poor weld penetration. This issue is usually overcome by modifying the ellipsoids semi axes values, resulting in a time-consuming model updating procedure that can lead to values without physical meaning. Therefore, adopting a heat source model that considers the actual power subdivision between filler and base metal would both improve modelling accuracy and speed up the model set up.

Proposed model

As earlier mentioned, the Goldak model does not allow to consider the actual power distribution between filler and base metal. Indeed, in GMAW, there are two ways in which arc power is transferred to the molten pool: direct transfer from electric arc to the base metal and filler metal melting energy transferred by means of droplets enthalpy. According to previous works [82], the power consumed in melting filler metal is about 50% of total arc power. Therefore, an accurate heat source model should take such power distribution into account.

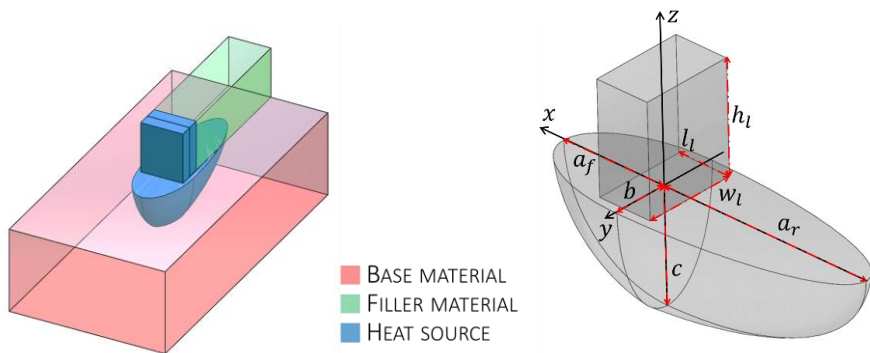


Figure 4.10: Proposed heat source model.

The base concept is to adopt different power distributions for the filler and base material: part of the total power is delivered to the base material by a Goldak Gaussian distribution, while the remaining one is distributed over the filler material with a constant pattern. This allows to capture the steep temperature gradients in the molten pool, accurately described by Goldak heat source [121] and transmit the correct amount of heat to the filler material elements. Figure 4.10 shows the heat source positioning with respect to the substrate, while proposed power density function is presented in Eq. 16.

$$\begin{cases} \dot{q}_b = \frac{6\sqrt{3}\dot{Q}_b f_{f,r}}{\pi\sqrt{\pi}a_{f,r}bc} \exp\left(-3\left(\frac{x^2}{a_{f,r}^2} + \frac{y^2}{b^2} + \frac{z^2}{c^2}\right)\right) \\ \dot{q}_w = \frac{\dot{Q}_w}{V_{el}} \end{cases} \quad \text{Eq. 16}$$

Subscripts f and r are assigned according to the Goldak model notation. \dot{Q}_w and \dot{Q}_b are the total powers delivered respectively to the filler and the base metal. As earlier mentioned, the amount of total power consumed in melting filler material is roughly 50%. Hence, as first approximation \dot{Q}_w and \dot{Q}_b can be set as shown in Eq. 17:

$$\dot{Q}_w = \dot{Q}_b = \frac{\eta i V_a}{2} \quad \text{Eq. 17}$$

As earlier mentioned, the power transmitted to the substrate is included according to the Goldak double ellipsoid model, while for the filler metal a specific model was developed. Basically, an internal heat generation is applied to the filler FE elements whose centroid lies inside a brick shaped control volume, moving according to deposition path, as shown Figure 4.10. The power density value is defined as the ratio between the wire melting power and the volume of the elements currently heated by the power source. Such volume depends on the heat source size along feed direction, l defined in Figure 4.10. The value of such parameter must be defined to transmit the correct amount of energy to filler FE elements. As first approximation the weld bead can be modelled with a rectangular cross section, using hexahedral elements with a drag pattern along the feed direction as shown in Figure 4.11.

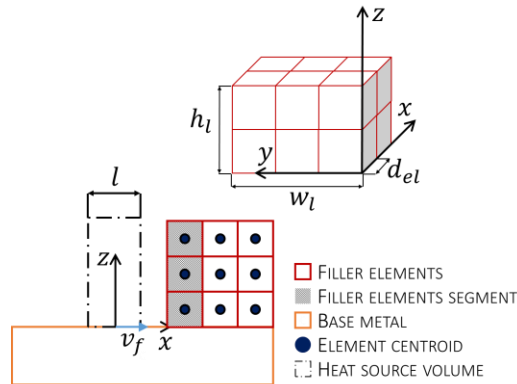


Figure 4.11: Filler mesh interaction with proposed heat source model.

Let d_{el} be the size of filler FE elements along the feed direction. In proposed model the control volume cross section has the same dimensions of the weld bead, i.e w_l and h_l , as

outlined in Figure 4.10. The heat transmitted to the filler material per unit volume can be computed as the ratio between filler power and material flow rate:

$$q_w = \frac{\dot{Q}_w}{\dot{V}} = \frac{\dot{Q}}{v_f w_l h_l} \quad \text{Eq. 18}$$

Where v_f represents the feed speed of the welding head. This value should be equal to the energy per unit volume actually transmitted to the workpiece in the FE model. If power density function is kept constant throughout the element volume V_{el} , the energy per unit volume transmitted to filler in the FE model can be computed according to Eq. 19

$$q_w = \frac{\dot{Q}_w}{V_{el}} \tau = \frac{\dot{Q}_w}{w_l h_l d_{el}} \frac{l}{v_f} \quad \text{Eq. 19}$$

Where τ is the time interval in which the centroids of the FE elements corresponding to a single segment, lies inside the control volume. Since the expressions of q_w given by Eq. 18 and Eq. 19 must be equivalent, the heat source length can be finally identified:

$$l = d_{el} \quad \text{Eq. 20}$$

Therefore, heat source dimension in feed direction must be equal to the correspondent size of filler FE elements, in order to transmit them the correct amount of energy. In summary, proposed heat source model allows to transmit the correct amount of thermal power to the FE model, considering the actual subdivision of the energy between filler and base material.

Model validation: test case definition

The accuracy of proposed model was verified analyzing the correlation of simulated and actual distortions, in a bead on plate test case. Manufacturing of both samples was carried out by WAAM technique using the prototype machine presented in section 3.2. Figure 4.12 shows test case dimensions. The distortions in Z direction (shown in Figure 4.12) were measured by means of a Coordinate-Measurement-Machine (CMM), and experimental results were then compared with FE model results. To compare proposed modelling strategy with the traditional Goldak heat source model the test case was FE modelled using both techniques.

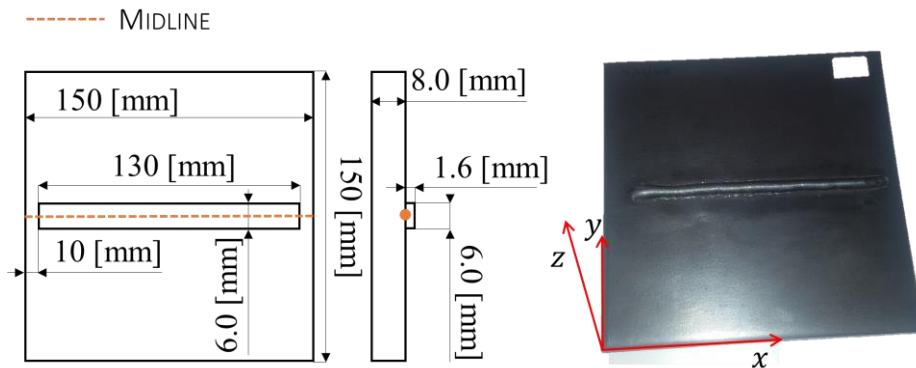


Figure 4.12: Test cases dimensions and actual bead on plate.

Model validation: experiments

The base plate material was S235JR structural steel while the bead was deposited using an ER70S-6 metal wire with 0.8 mm diameter. The deposition was carried out using a Millermatic 300 direct current GMAW welding unit, using the following process parameters: travelling speed 300 mm/min, wire feed speed 4.6 m/min, open circuit voltage 19 V, average welding current 81 A, average welding voltage 18.1 V. Welding current and voltage were measured during the manufacturing process to accurately quantify the average thermal power value to be used in the heat source model. (1480 W). The test case was constrained with an isostatic scheme during the deposition process. This fixture scheme was realized supporting the base plate on three rest points. This strategy was preferred to avoid modeling the boundary conditions and the unclamping simulation that could affect the validation analysis.

The top surface of the base plate, corresponding to $z = 0$ (Figure 4.12), was scanned with a Mitutoyo Euro Apex C776 CMM. The specimen was scanned before and after the WAAM operation, in order to evaluate the Z component of the displacement field, with respect to the frame of reference shown in Figure 4.12. This process allowed to evaluate the correlation between experiments and model results, excluding the influence of top surface unevenness.

Model validation: FE model

The FE model of the test case described in previous section was created using the developed techniques. Analyses were carried out using LS-Dyna commercial finite element code. The overall geometry, including both filler and base metal, was discretized using 35740, 8-nodes brick elements. The FE model of the test case is presented in Figure 4.13. Manufacturing process simulation was carried out using a coupled transient thermo-mechanical solution routine. Such simulation was carried out using a Crank-Nicholson integration scheme for the heat transfer solution and a fully implicit one for the mechanics.

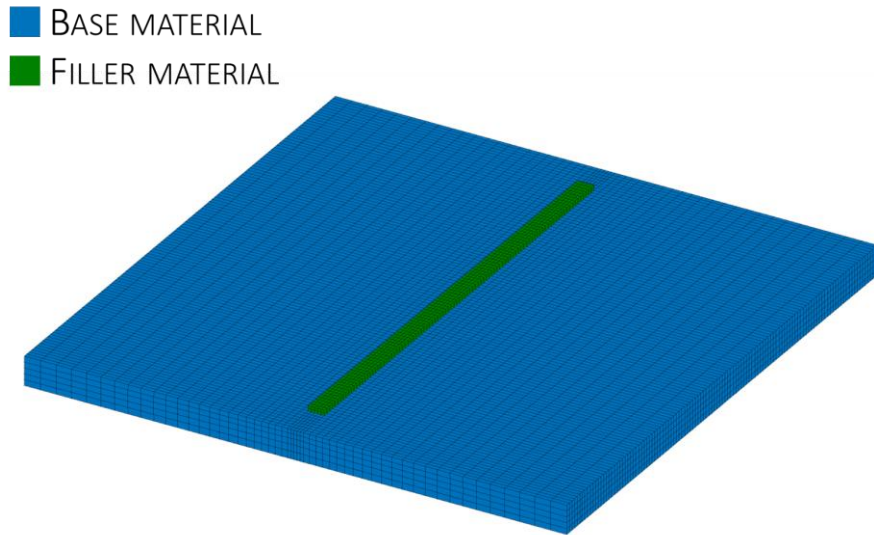


Figure 4.13: FE model of the test case.

The heat source was modelled according to the proposed technique. Heat source parameters used in test case manufacturing simulation are summarized in Table 4.5.

Table 4.5: Heat source parameters.

a_f [mm]	a_r [mm]	b [mm]	c [mm]	f_f [mm]	f_r [mm]	l [mm]
1.4	3.5	3.0	3.0	0.6	1.4	1.4

The ellipsoid parameters were set according to molten pool dimension, as shown in Figure 4.14, while the length of the filler metal heat source was set consistently with proposed procedure.

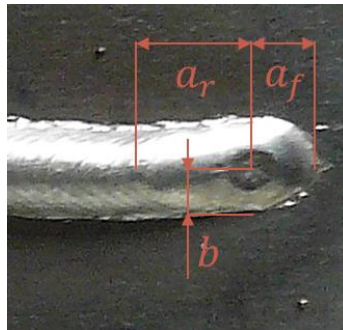


Figure 4.14: Procedure used to estimate the heat source parameters.

Both the thermal and mechanical behavior of the material was modelled using the temperature dependent material properties presented in the beginning of the section. In the same way, the element activation technique was modelled according to the presented quiet element method technique.

Free convection boundary conditions were set up on the base plate top and bottom surfaces. Convection coefficients values, set according to literature correlations [126], were: 8.5 [W/m²K] for the base plate top surface and 4.0 [W/m²K] for the bottom surface. A boundary condition of general radiation to environment was included, setting material emissivity to 0.2. Environment and material initial temperatures were set to 298.16 [K]. Mechanical boundary conditions were included in the model by means of single point constrains.

Model validation: Results and discussion

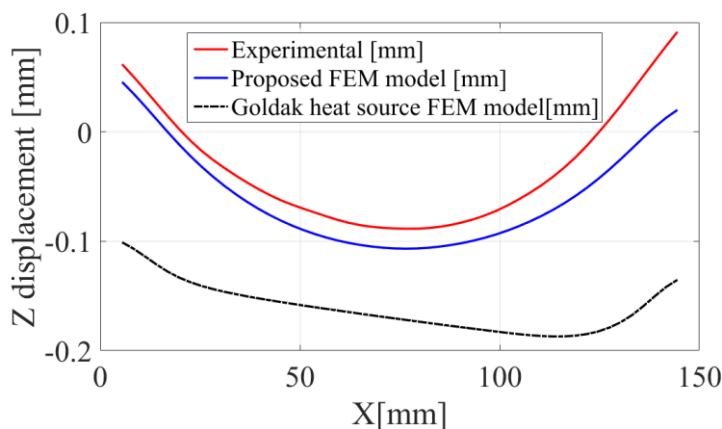


Figure 4.15: Midline displacements for the bead on plate.

FEM and experimental midline displacements were compared. As shown in Figure 4.12 for the wall and bead on plate test cases the mean line is defined as the weld bead axis in correspondence of the base plate, hence at z coordinate 0 value. Figure 4.15 shows the results of such comparison. It is clear that the Goldak model leads to a remarkable overshoot in midline displacement. On the other hand, proposed model allows to achieve a good correlation between simulated and measured displacement field. This result could be explained comparing temperature distributions of the two modelling strategies, shown in Figure 4.16. It is highlighted that the Goldak model (Figure 4.16 (a)) leads to a higher temperature peak in the molten region (orange and red colors) than proposed modelling strategy (Figure 4.16 (b)). This is expected since both simulation were performed setting the same power input and locating the origin of the moving frame of reference in correspondence of the top surface of the base metal. In this condition, the proposed model transmits the correct amount of thermal power to the workpiece, whereas the Goldak model transmits twice the effective welding power.

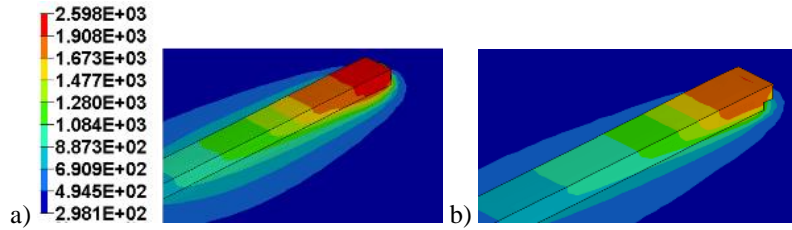


Figure 4.16: Bead on plate models temperature field [K] a) Goldak b) Proposed model.

To confirm this conclusion, the manufacturing test was repeated by measuring the workpiece temperature during the process. To achieve this, two k-type thermocouples were attached to the substrate. The thermocouples positions are presented in Figure 4.17.

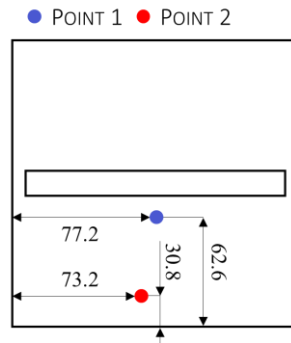


Figure 4.17: Thermocouples positions in the temperature measurement test.

The thermocouples signals were acquired using a National Instruments 9213 data logging system. The data were at a sampling frequency of 10 Hz. The measured temperature data were compared to the time histories of the FE model nodes located in correspondence of the thermocouples positions. The result of this comparison is presented in Figure 4.18.

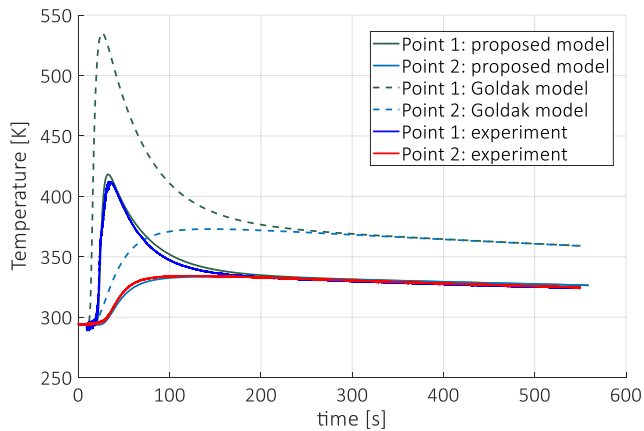


Figure 4.18: Comparison of the thermocouple data with the simulations performed using both the proposed and the Goldak heat source model.

It is highlighted that the proposed model returns an accurate prediction of the workpiece temperature, whereas the Goldak model results in a significant overestimation. This confirms the conclusion drawn by the results presented in Figure 4.16.

The main relevance of the achieved result is that no tuning operation was performed to set the heat source parameters returning an accurate result for the proposed model. On the opposite, achieving the same accuracy with the Goldak model would require time consuming model updating operations. Besides, it should be considered that material data have been derived from literature, hence actual material behavior could be different from the model one. Furthermore, no tuning operation was carried out for what concerns convection coefficients and heat source parameters, as it is usually performed in works dealing with WAAM simulation. Hence the proposed model returns a reliable prediction general pattern of the workpiece displacement field with a good punctual accuracy, that could be improved with a better representation of actual material behavior and boundary conditions.

4.3.2. Proposed latent heat modelling technique

WAAM models are solved by means of transient FEM simulations. Therefore, one of the most effective approaches to reduce the calculation time is to increase the simulation time step. However, this is not a straightforward task, since it could result in a significant reduction of the simulation accuracy. The strictest constraints to the simulation step are prescribed by:

- The heat source dimension
- The latent heat of fusion

The heat source dimension constraints the maximum achievable time step since it must not be larger than the time required to the welding torch to travel along a distance equal to the heat source x semi-axes [84]. Not meeting this constraint could result in a non-continuous heating by the heat source.

The latent heat of fusion prescribes a further constraint to the time step. Indeed, the latent heat of fusion is usually spread among the solidus and liquidus temperatures of the material. The most common approach to introduce it in the WAAM simulation is by the temperature dependent heat capacity [137]. This constant is artificially raised in the phase transition range to simulate the latent heat effect, i.e. an increased thermal inertia. However, this could result in severe convergence issue, forcing to reduce the time step.

An effective approach to increase the simulation time step was proposed by Ding et al. [110,138]. In these works, the authors proposed to solve the transient problem as a succession of steady state solutions, resulting in a significant reduction of the calculation time. Shanghvi and Michaleris [139] proved that this approximation can lead to accurate results when simulating multi-pass welding operations of large components. However, despite its efficiency, this approach is limited to large components.

This thesis proposes to increase the simulation time step by introducing an innovative way of modelling the latent heat of fusion. Rather than including its effect in the heat capacity curve, the proposed model introduces a heat generation function proportional to the time derivative of the liquid phase fraction. This results in an enhanced convergence of the simulation, even using large time steps.

Table 4.6 summarizes the state of the art of the time step increasing techniques.

Table 4.6: State of the art techniques to increase the simulation time step

Increasing of simulation time step	
<i>State of the art</i>	
Ding et al. [110,138]	Simulation approach for large parts: Step-wise steady state solution for large components

Traditional latent heat modelling

In this technique, the heat capacity is modified to accommodate the increased thermal inertia of the material in the phase transition range. The enthalpy variation of a material that experience a phase transition can be expressed by Eq. 21:

$$\Delta h|_{T_0}^{T_1} = \int_{T_0}^{T_{sol}} C_p(T) dT + h_{lat} + \int_{T_{liq}}^{T_1} C_p(T) dT \quad \text{Eq. 21}$$

Where h represents the material enthalpy per unit mass; T_0 is the initial temperature, below the solidus one; T_1 is the final temperature above the liquidus one; T_{sol} and T_{liq} are respectively the solidus and liquidus temperatures; h_{lat} is the latent heat of fusion.

The latent heat effect can be included by modifying the heat capacity curve in the phase transition range according to Eq. 22:

$$C_p^{eq}(T) = \begin{cases} C_p(T) & T_{liq} < T < T_{sol} \\ C_p^{fic}(T) & T \in [T_{sol}, T_{liq}] \end{cases} \quad \text{Eq. 22}$$

Where $C_p^{eq}(T)$ is the new heat capacity curve and $C_p^{fic}(T)$ is a function defined to satisfy Eq. 23:

$$\begin{cases} C_p^{fic}(T_{sol}) = C_p(T_{sol}) \\ C_p^{fic}(T_{liq}) = C_p(T_{liq}) \\ \int_{T_{sol}}^{T_{liq}} C_p^{fic}(T) dT = h_{lat} \end{cases} \quad \text{Eq. 23}$$

The first and the second relations are introduced to have a continuous C_p^{eq} function. The third one represents the equivalence of the latent heat. This equation can be solved, prescribing a fitting function for $C_p^{fic}(T)$, and calculating the function coefficients. Figure 4.19 shows an example of the $C_p^{eq}(T)$ function calculated for the ER70S-6 steel by defining $C_p^{fic}(T)$ as a second-degree polynomial fitting function.

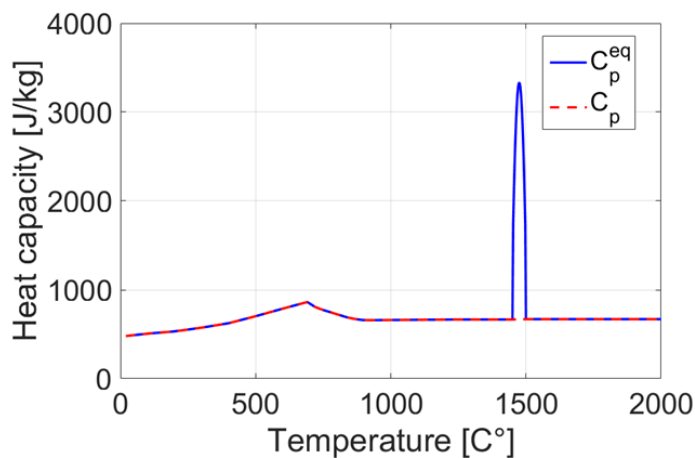


Figure 4.19: Example of a modified heat capacity curve, including the latent heat effect.

Due to the large value of the assumed by the latent heat of fusion, the equivalent heat capacity curve has a steep gradient in the phase transition range. This can lead to convergence issues since this term is included in the tangent matrix [140]. The most effective way of improving the convergence behavior is to reduce the time step. This decreases the temperature variations in the simulation step, improving the convergence behavior. However, due to the steep temperature increase occurring in the WAAM process, an excessively small time-step could be required to significantly reduce the temperature variation in a single simulation step. This would result in significant computational inefficiencies. This issue is exemplified by Figure 4.20, which shows the temperature increase of FE node during a WAAM simulation. It is highlighted that the approach of the heat source leads to an extremely steep increase of the temperature, requiring an excessively small time step have a significant effect on convergence behavior.

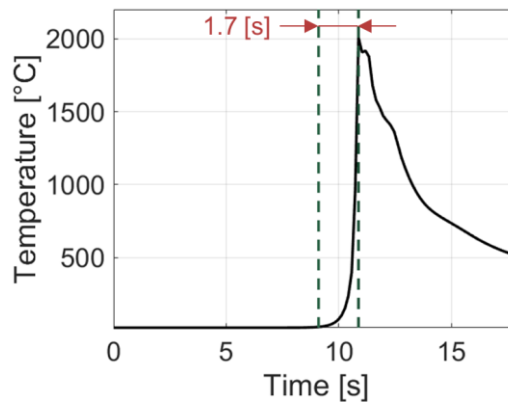


Figure 4.20: Temperature rise due to the heat source passage drawn from a WAAM simulation.

The solution usually pursued is to artificially increase the phase transition range. This reduces the peak value of the equivalent latent heat curve, resulting in a smoother pattern. However, this approach modifies the actual material behavior, resulting in a reduced thermal inertia in the phase transition range.

The proposed technique overcomes the current limitations by introducing the latent heat as a heat generation. This approach allows to increase the time step without convergence issues. The effectiveness of the proposed model is shown by a set of numerical tests. Moreover, this sub-section presents a numerical-experimental comparison which highlights the importance of including a latent heat model in WAAM simulation.

Proposed latent heat model

The proposed approach is to include the latent heat as a heat generation function rather than as an increased heat capacity. Indeed Eq. 21 can be fulfilled by means of a source term that satisfies Eq. 24:

$$\begin{cases} \Delta h|_{T_0}^{T_1} = \int_{T_0}^{T_{sol}} C_p(T) dT + \int_{T_{sol}}^{T_{liq}} \dot{q}_{lat}(T(t)) dT + \int_{T_{liq}}^{T_1} C_p(T) dT \\ \int_{T_{sol}}^{T_{liq}} \dot{q}_{lat}(T(t)) dT = h_{lat} \\ \dot{q}_{lat}(T(t)) = 0 \quad T_{liq} < T < T_{sol} \end{cases} \quad \text{Eq. 24}$$

Where \dot{q}_{lat} is the equivalent source term, namely generated heat per unit time and per unit volume. Eq. 24 prescribes the constraints to define the heat source: it must not generate any heat outside the phase transition range and it must generate an amount of heat equal to the latent heat in the phase transition range. These conditions can be fulfilled by the heat source defined according to Eq. 25

$$\dot{q}_{lat} = -\frac{dx_l}{dt} \left(\frac{\rho h_{lat}}{T_{liq} - T_{sol}} \right) \quad \text{Eq. 25}$$

Where the x_l represents the liquid phase fraction per unit mass that can be computed as a function of temperature according to Eq. 26:

$$x_l = \begin{cases} x_l = 0 & T < T_s \\ x_l = \frac{T - T_s}{T_l - T_s} & T_s \leq T \leq T_l \\ x_l = 1 & T > T_l \end{cases} \quad \text{Eq. 26}$$

Figure 4.21 shows an example of the general pattern of the liquid phase fraction function.

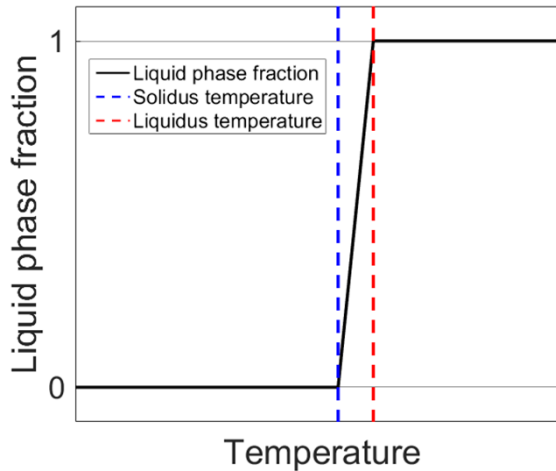


Figure 4.21: General pattern of the liquid phase fraction function.

It must be pointed out that when the time derivative of the liquid phase fraction is positive (i.e., in material melting) the generated heat will be negative (i.e., it will be subtracted by material internal energy). On the opposite, during the solidification the time

derivative of the liquid phase fraction is negative, making the generated heat positive (i.e., added to material internal energy). This results in the same effect of increasing the material heat capacity in the phase transition range.

The proposed model can be implemented in any FE solver by calculating the time derivative of the liquid phase fraction by the backward finite difference technique:

$$\dot{q}_{lat} = -\frac{dx_l}{dt} \left(\frac{\rho h_{lat}}{T_{liq} - T_{sol}} \right) \cong -\frac{x_l^{i+1} - x_l^i}{\Delta t} \left(\frac{\rho h_{lat}}{T_{liq} - T_{sol}} \right) \quad \text{Eq. 27}$$

Where x_l^{i+1} is the liquid phase fraction evaluated at the current temperature; x_l^i is the liquid phase fraction evaluated with the temperature at the previous time step; Δt is the current time step. This strategy results in a generated heat equal to the latent heat of fusion independently on the temperature increase in the current time step. This allows to increase the simulation time step without resulting in an inaccurate description of the material behavior in the phase transition range.

The proposed model was implemented in the LS-DYNA solver by means of the *MAT_THERMAL_USER_DEFINED feature [123], including it in both base and filler materials definition.

Verification of the proposed latent heat model

The effectiveness of the proposed latent heat model is verified by means of a thermal simulation carried out on a single bead. The model presented in Figure 4.22 was used for this test.

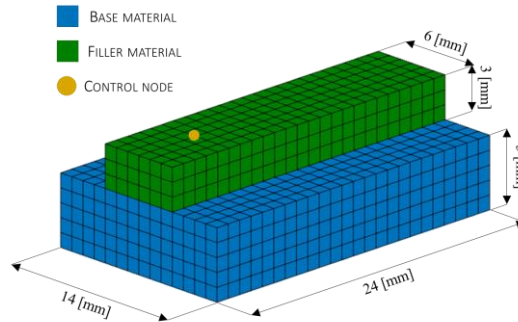


Figure 4.22: The FE model used to test the heat source effectiveness

It is a single ER70S-6 bead deposited on a S235JR substrate. The material properties depicted in the beginning of the section were used in this model exception made for the solidus and liquidus temperature, which were set respectively to 1673 K and 1723 K. This narrowed the phase transition range to 50 K, increasing the harshness of the test for the proposed model. The heat source parameters and the travelling speed set as the ones presented in subsection 4.3.1.

The effectiveness of the proposed model was tested using the adaptive time stepping scheme provided by LS-DYNA [123]. In this algorithm, the user sets the maximum temperature variation allowed in a simulation step ($\Delta T_{allowed}$). The FE solver automatically adjusts the time step to meet this condition. Several simulations were carried out increasing the value of $\Delta T_{allowed}$ resulting in an increase of the time step. This strategy allows to test

the model at different temperature increase in a single time step, assessing its accuracy. A reference simulation was carried out using a fixed time step equal to $1.0e-4$ s, a value far lower than the ones achievable by the variable time stepping. Figure 4.23 shows the results of the reference simulation in terms of contour plot.

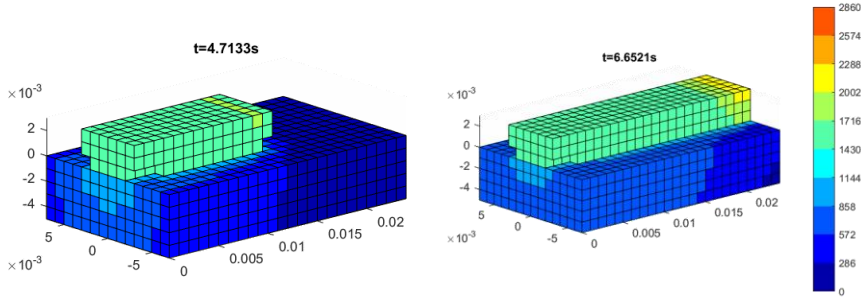


Figure 4.23: Result of the FE simulation in terms of contour plot at two different steps.

The parameter used to show the accuracy of the proposed model is the error on the peak temperature of the control node (Figure 4.22) evaluated with respect to the reference simulation. The efficiency of the model is evaluated by comparing the elapsed simulation time at increasing $\Delta T_{allowed}$. Figure 4.24 shows the results of accuracy and efficiency comparisons.

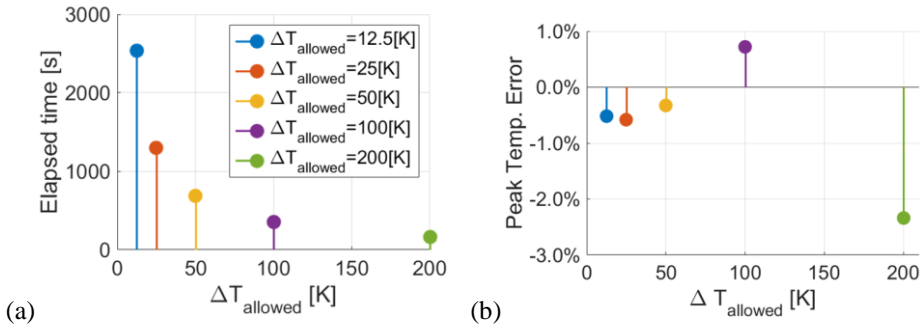


Figure 4.24: Comparison of the model performances at different time steps in terms of: elapsed simulation time (a); error on the control node peak temperature with respect to the reference simulation.

As shown in Figure 4.24 (a), five simulations were carried out using $\Delta T_{allowed}$ values ranging from 12.5 K, i.e. half of the phase transition range (50 K), to 200 K, i.e. four times the phase transition range. Figure 4.24 (a) highlights a significant effect of this parameter on the simulation time, suggesting that its increase is fundamental for the simulation efficiency. Moreover, Figure 4.24 (b) shows that an even for the maximum value of $\Delta T_{allowed}$, the simulation error is below 2%, an acceptable value for such a decrease of the simulation time.

The results of this comparison shows that the proposed latent heat model meets the stated requirements: it returns accurate results even with high value of the simulation step and it does not cause any convergence issues.

Numerical-experimental comparison

The aim of this paragraph is to show the importance of the latent heat contribution to the accuracy of WAAM simulation. To achieve this purpose, the manufacturing of the test-case presented in sub-section 4.3.1 was simulated using the proposed latent heat model and without including any latent heat. The simulations were carried out using the parameters presented in the previous sub-section. The results of the simulation were compared to the thermocouples data presented in Figure 4.18. The results of this comparison are presented in Figure 4.25.

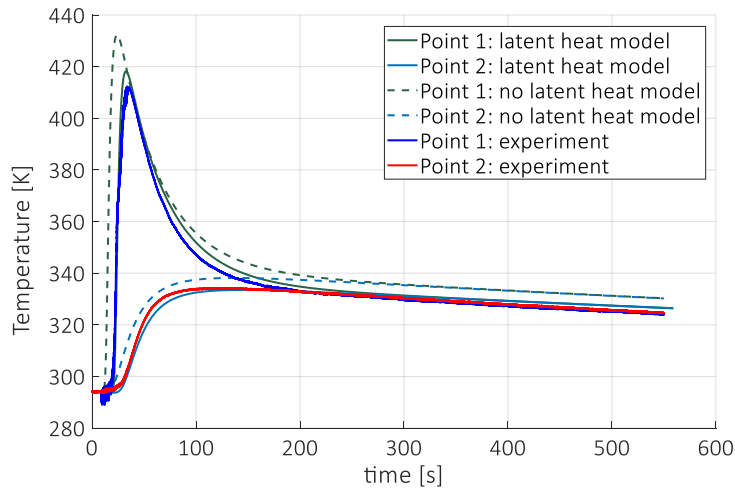


Figure 4.25: Comparison of thermocouples data with FE simulations with and without latent heat model.

It is highlighted that neglecting the latent heat contribution leads to a general overestimation of the workpiece temperature throughout the whole operation. In particular, the model without latent heat predicts the peak temperature of point 1, the one located closer to the weld bead, with an error of 4.9% versus a 1.5% achieved by the proposed model. This is compliant with a reduction of the material thermal inertia due to the neglect of the latent heat contribution. Moreover, the model without latent heat predicts a faster heating than the experimental data, whereas the proposed latent heat model is in line with the thermocouple measurements. As for the temperature overestimation, this difference is compliant with an underestimation of the thermal inertia in the phase transition range introduced by the neglect of the latent heat.

In light of these data it is possible to state that neglecting the latent heat reduces the accuracy of WAAM simulation for what concerns the temperature field. Moreover, this is expected to affect the mechanical simulation as well, since both the distortions and the residual stresses are determined by thermal history of the workpiece material. Finally, it is important to point out that the materials considered in this comparison exhibit a quite broad phase transition range (more than 100K) as shown in Table 4.3. Therefore, the latent heat is reasonably expected to have a greater effect on materials with a narrower phase transition range.

4.3.3. Substrate mesh coarsening technique

The previous section focused on reducing the calculation time by increasing the simulation time step. However, this goal can be achieved by a different approach: to reduce the number of model DOFs (Degrees Of Freedom), namely to reduce the number of elements used for the workpiece discretization.

In an AM simulation, the number of elements (i.e., the number of DOFs), is constrained by the maximum mesh size required by the molten pool. Since metal deposition involves a local heating of the workpiece, to achieve an accurate description of the temperature field, a minimum number of elements per molten pool radius must be used. This aspect was already shown in the simulation of similar processes, such as welding [121] and laser forming [141]. Such requirement leads to a constraint for the elements size of both filler material and substrate. In particular, all the FE elements representing the deposited material should meet the maximum size criterion, because during the simulation they will experience a melting transformation. Nevertheless, one should consider that this requirement needs to be met locally, where the molten pool induces relevant temperature gradients. It is worth noting that, as the simulation progresses, the deposition head and consequently the molten pool move along the workpiece. This leads to filler regions represented by a number of elements, originally defined in accordance with the maximum size criterion, that would result excessive, considering the reduction of temperature gradients over those areas. In addition, the substrate elements size shall be defined in accordance to the one of the filler (to ensure mesh connectivity) even though most of the substrate does not experience any phase change.

Considering these aspects, the techniques to reduce the model DOFs pursue two main strategies: i) reducing the number of elements of the filler metal far from the molten pool and ii) reducing the number of elements of the substrate.

In the first group, an adaptive re-meshing of the deposited material elements is performed. Denlinger et al. [142] presented a re-meshing technique in which a mesh coarsening is performed after the deposition of every layer, extracting solution variables on the coarsened grid by means of an interpolation algorithm. Michaleris [143] proposed to apply the H-adaptivity technique, i.e. to use a coarse mesh that is selectively refined in the vicinity of the heat source. Both these approaches produced accurate results and produced a significant reduction of the simulation time.

The most common technique to reduce the elements of the substrate is mesh-biasing [144]. In this technique, the mesh size of the substrate is increased proportionally to the distance from the filler elements. This technique is adopted in most FEM based AM simulations. Nevertheless it has a significant drawback: an excessive increase in mesh size could affect elements geometry, leading to the generation of elements with excessive aspect ratios [145]. This can lead to severe issues in the mechanical analysis, introducing errors in estimating the base material bending [118]. Reducing the number of elements required to discretize the substrate is an important task mainly considering the hybrid process, where WAAM operations can be used to add features on existing components. Therefore, the development of techniques that allow to increase the substrate mesh size without significant inaccuracies is an important aspect for WAAM simulation.

The state of the art techniques used to reduce the FE model DOFs are listed in Table 4.7.

Table 4.7: State of the art techniques to reduce the model DOFs.

Decreasing of required DOFs	
<i>State of the art: Increase of the filler mesh size</i>	
Michaleris [143]	Application of H-adaptivity to welding: Selective mesh refinement in correspondence of the heat source.
Denrlinger and Michaleris [142]	Selective mesh coarsening: Adaptive coarsening of the layers after their deposition
<i>State of the art: Increase of the substrate mesh size</i>	
e.g.: [142], [144], [146]	Mesh biasing: Continuous mesh coarsening in regions far from the deposited material.

This thesis presents a new method to reduce the number of elements required for the substrate discretization. Unlike the traditional mesh biasing technique, the proposed approach increases the elements size without affecting their quality. This is achieved by splitting the substrate geometry in multiple sections that are individually discretized with different mesh size. The model of the complete substrate is then created by connecting the different sections with a double-sided contact algorithm.

First, this subsection discusses the details of the proposed technique. Then a numerical validation is presented: a simple bead on plate simulation is carried out using the proposed mesh coarsening technique and the traditional mesh biasing. The results in terms of temperature distribution are then compared with a reference model. Finally, the proposed technique is applied to an experimental case study, comparing the actual and simulated distortions. This verification proves the accuracy of the proposed technique, in terms of distortions prediction.

Proposed technique: overview

The residual stresses and distortions of AM parts are related to the non-uniform temperature distribution in the workpiece. For this reason, thermo-mechanical coupled FE models are used to model such effects in AM operations.

Since the outcome of the heat transfer analysis (transient temperature distribution of the workpiece) is used as input load for the mechanical analysis, correctly capturing the temperature gradients in this phase is mandatory to ensure an accurate prediction of the workpiece mechanical response. Hence, the FE mesh pattern and size must be consistent with the temperature gradients experienced by the workpiece, conflicting with the need of reducing the number of elements.

The proposed method reduces the number of FE elements used to discretize the workpiece, without introducing significant errors in estimating the temperature field. The base concept is to replace the mesh biasing technique with a mesh zoning approach, which consists in defining different zones of the workpiece substrate to be separately discretized and then connected in order to achieve a continuous body behavior. Hence, the workpiece is discretized with a discontinuous mesh, achieving a significant reduction of the elements

number without compromising their aspect ratios and consequently the results. The key points of proposed technique are:

1. Mesh zones joining.
2. Mesh zones definition.

Proposed technique: mesh zones joining

Varying the mesh size throughout the substrate geometry is a common practice to reduce the number of elements used for the discretization. This is usually performed with the mesh biasing technique, i.e., the element dimension is progressively increased in a specific direction to reduce the number of elements. This leads to a non-uniform mesh size, increasing with the distance from the filler material. An example of a biased mesh is shown in Figure 4.26 (b).

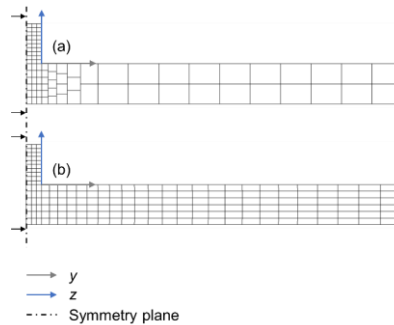


Figure 4.26: Comparison of the proposed coarsening technique (a) and mesh biasing (b).

Despite the straightforward implementation of such technique in commercial FE pre-processors, it has a significant drawback: as the distance from the substrate increases, the element geometry experiences significant distortions, leading to high aspect ratio values, as exemplified in Figure 4.26 (b). It is worth highlighting that this issue gets particularly relevant in hexahedral elements, while tetrahedrons better suite a biased mesh pattern without relevantly affecting the elements aspect ratio. On the other hand, hexahedrons are the most common type of elements used in both AM and welding simulation since they allow to achieve a high accuracy in the mechanical analysis with first order shape functions, unlike tetrahedrons. For this reason, the proposed mesh coarsening technique will be discussed referring to hexahedral elements, but the application to tetrahedral elements is feasible and straightforward.

The proposed mesh zoning technique is based on a non-conformable interfaces approach. Indeed, the criticalities of the mesh biasing technique arise because the workpiece is discretized as a single body. This means that two adjacent zones with different mesh size, are forced to share the interface nodes to provide structural continuity. The solution proposed to overcome such issue is based on discretizing the different zones separately. This avoids the conformable interface constraint, allowing the different zones to have different element size in both x , y and z directions, as exemplified in Figure 4.26 (a). This gives the chance to fully exploit the mesh size identification algorithm, since the mesh size can be arbitrarily increased, without affecting the elements aspect ratios. This technique relies on joining the different zones in correspondence of non-conformable interfaces, to achieve the structural

continuity, for both heat transfer and mechanical solutions. With the current FE solvers capabilities this can be achieved by means of double sided contact algorithms. These algorithms are implemented in most commercial FE solvers and are currently used for research purposes in several fields [130,147,148]. For the mechanical solution these contact algorithms prescribe a set of multi-point-constraints blocking the relative motion of the interface in both normal and tangential directions. For the heat transfer solution, such algorithms enforce the contacting surfaces to have the same temperature and heat flux in normal direction. The mechanical and thermal constraints allow to simulate the behavior of a continuous body without requiring mesh conformity between the adjacent zones. Hence the double-sided contact algorithm represents an effective tool to implement the mesh size distribution identified by the proposed algorithm, without resulting in a relevant increase of the elements aspect ratios over the zones further from the welding bead.

Proposed technique: strategy for mesh zones definition

Having highlighted the double sided contact algorithm as a key tool to balance model DOFs reduction and elements quality, identifying a suitable strategy to define the different mesh zones is mandatory. Indeed, the proposed mesh zoning involves an increase of mesh size, potentially affecting the solution accuracy. For this reason, a systematic tool to define the mesh zones pattern is proposed.

The FE models used for AM simulation can be divided in two main regions, featuring different requirements in terms of mesh size: the deposited material and the base material, that is the focus of this activity. Different phenomena occur in such areas, requiring the adoption of different mesh sizing criteria. For what concerns the deposited material, the mesh size requirement is imposed by the dimension of the molten pool, i.e., to the heat source dimensions ([121],[145]). On the opposite, the base material does not undergo the heat generation, exception made for the region underneath the first layer. Therefore, a different discretization requirement shall be identified for the substrate, to balance simulation accuracy and time efficiency.

The proposed technique allows to identify the mesh size required to effectively cope with the thermal gradients in the substrate and to implement such discretization minimizing FE elements distortion. The underpinning concept is that when using the FE method to solve a heat transfer problem the exact value of the solution can be computed only at nodal points. In the remaining part of the domain, the solution variables are interpolated by means of FE elements shape functions [140]. Hence, the FE mesh should be defined consistently with the expected temperature field to minimize the interpolation error.

In practice, the proposed method starts with the estimation of the temperature distribution pattern by means of an approximated analytical solution of the heat transfer problem in welding. Then, such solution is fitted with a piecewise polynomial function. This interpolation process is similar to a FE solution, in which exact temperature values could be computed only in correspondence of mesh nodes. This allows to identify the largest mesh size, ensuring reduced error values.

The key aspects of the proposed method are:

- Analytical solution to estimate temperature distribution;
- Zones subdivision strategy;
- Zones mesh size definition;

Proposed technique: analytical model used for the mesh zones definition

The proposed technique uses the aforementioned Rosenthal analytical solution to estimate the temperature field of the component substrate [133]. This simplified model allows to compute the workpiece temperature field based on the following assumptions:

- Punctual heat source, rather than a distributed one.
- Semi-infinite solid.
- The temperature dependence of material properties is neglected.
- The transformation heat effect is neglected
- Straight welding trajectory.
- Quasi steady state solution.

The quasi steady state condition means that the workpiece has an infinite heat capacity, since it is assumed to be a semi-infinite solid. This allows treating the heat diffusion problem as steady state in a coordinate system moving according to the welding path, as defined in Eq. 28 and shown in Figure 4.27:

$$\begin{cases} x^1 = x - v_f t \\ y^1 = y \\ z^1 = z \end{cases} \quad \text{Eq. 28}$$

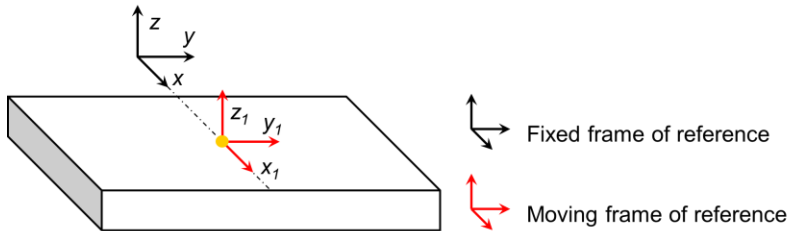


Figure 4.27: Rosenthal model outline.

where v_f is the welding velocity. With these assumptions, the solution of the heat diffusion problem is given by Eq. 29:

$$T(x_1, y_1, z_1) = T_0 + \frac{\dot{Q}}{2\pi\lambda} \exp\left(-\frac{v_f x^1}{2\alpha}\right) \exp\left(-\frac{v_f R}{2\alpha}\right) \frac{1}{R} \quad \text{Eq. 29}$$

where T is the unknown temperature, T_0 is the initial uniform workpiece temperature, λ is the thermal conductivity, α is the thermal diffusivity, \dot{Q} is the thermal power input and R is defined by Eq. 30:

$$R = \sqrt{x_1^2 + y_1^2 + z_1^2} \quad \text{Eq. 30}$$

Clearly the Rosenthal model involves many strong assumptions, not ensuring an accurate estimation of the workpiece temperature field, in particular in correspondence of the molten region. Nevertheless, this model takes the most significant parameters of process and material into account. This enables to quickly provide an estimation of the temperature distribution over the workpiece for a specific configuration. Hence it is considered here a suitable aid for the definition the optimal mesh size.

Proposed technique: mesh pattern used for the mesh zones definition

A mesh pattern is required to achieve a mesh zoning of the workpiece substrate. In particular, a direction of mesh increase shall be selected. This thesis proposes the mesh size increase along the y direction of the moving frame of reference defined by the Rosenthal model. The proposed mesh pattern is shown in for a simple bead-on-plate (Figure 4.28 (a)): the substrate is divided into several zones, defined by selecting planes normal to the welding trajectory and to the substrate plane.

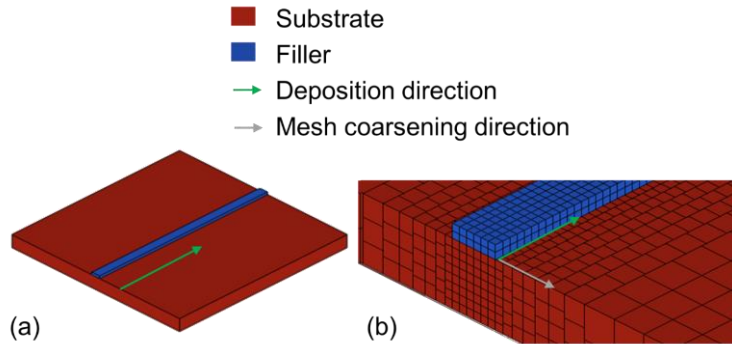


Figure 4.28: Simple bead on plate geometry (a) modelled using the proposed technique (b).

Each zone is uniformly discretized by hexahedral elements: the zone underneath the welding bead meets the heat source mesh size constraints, while for the other zones the mesh size increases with the distance from the substrate. This is compliant with the Rosenthal temperature distribution pattern: as shown in Eq. 29 the temperature gradient is steeper in the proximity of the welding arc (i.e., of the molten pool) and experiences a significant decay at increasing distance from the arc center.

Proposed technique: algorithm used to define the zones mesh size

The key point of the mesh zoning strategy is to define the mesh size for every zone to meet the interpolation error requirement. This is achieved by means of a specific recursive algorithm that interpolates the analytical temperature distribution with a polynomial function of the same order of the shape functions used in the FE model. Since first order elements are most commonly adopted for the heat transfer analyses, the algorithm is here presented referring to this specific element order (i.e., linear interpolation function). For starters the analytical temperature distribution is calculated, given the welding and material parameters, as a function of the y coordinate only (i.e., the mesh coarsening direction). This is achieved by evaluating Eq. 29 in $x^1 = 0$, $y^1 = y$ and $z^1 = 0$, as shown in Eq. 31:

$$T(y) = T(0, y, 0) = \frac{\dot{Q}}{2\pi\lambda} \exp\left(-\frac{v_f y}{2\alpha}\right) \frac{1}{y} \tag{Eq. 31}$$

Eq. 31 represents a function of the y coordinate, describing the workpiece temperature profile for a specific welding operation. It must be pointed out that evaluating the $T(y)$ function at $x^1 = 0$ and $z^1 = 0$ is a conservative option, since the steepest temperature gradients in y direction are located onto the workpiece top surface, thus requiring a finer interpolation grid to meet the error criterion. Figure 4.29 (a) shows the zone partition obtained by the algorithm: each zone i has a lower bound marked as y_1^i and an upper bound marked as y_2^i . Except for the lower bound of the zone 1, which coincides with the heat source semi-axis b , all the remaining boundaries are the unknowns to be identified. To achieve this, the algorithm operates in a sequential way, namely it identifies the unknown upper bound of a zone which is then used as the known lower bound of the subsequent one. Figure 4.29 (b) outlines the identification procedure of the unknown boundary y_2^i .

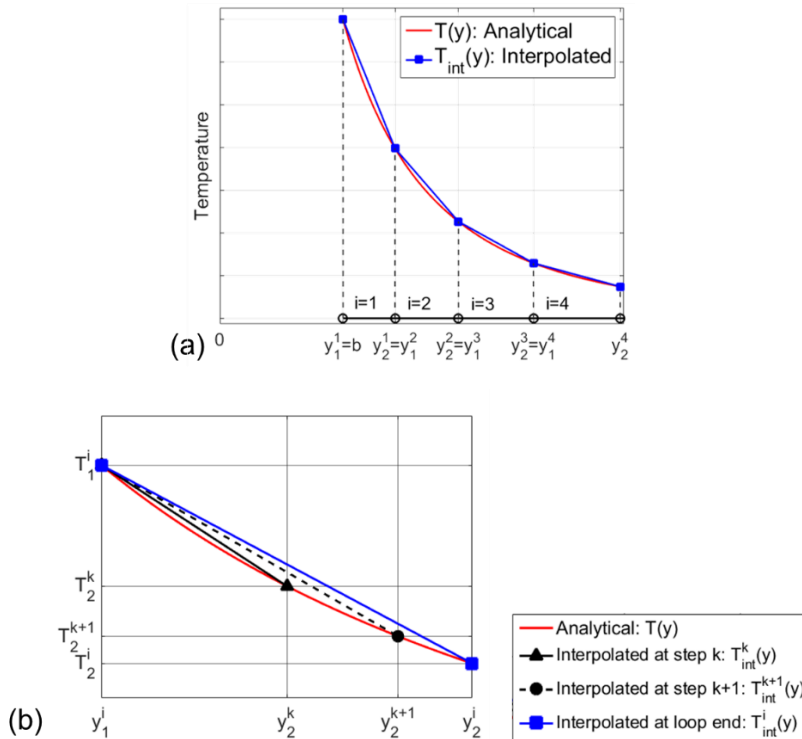


Figure 4.29: Temperature profile interpolation through mesh zoning (a) and stepwise algorithm outline (b).

As shown in Figure 4.8 (b), y_2^i is identified by means of a stepwise procedure. Assuming k parameter as step counter, a guess upper bound value is calculated, together with temperature values at zone boundary, as shown in Eq. 32:

$$\begin{cases} y_1^i = y_2^{i-1} \\ y_2^k = y_1^i + sk \\ T_1^i = T(y_1^i) \\ T_2^k = T(y_2^k) \end{cases} \quad \text{Eq. 32}$$

The parameter y_2^k is the guess upper bound of the i -th segment, T_1^i is the analytical temperature value computed in y_1^i and T_2^k is the analogous for y_2^k . The parameter s is the step distance, i.e., the distance between two subsequent guess boundaries. To ensure an accurate identification of the zones mesh size, s should be set to be much smaller than the heat source radius b . Once that guess zone boundaries are computed, the interpolation function is defined according to Eq. 33:

$$T_{int}^k(y) = \frac{T_2^k - T_1^i}{y_2^k - y_1^i} (y - y_1^i) + T_1^i \quad \text{Eq. 33}$$

This function represents the best approximation of the analytical temperature distribution achievable by a FE solver between the nodes placed in y_1^i and y_2^k (i.e., linear shape function). Finally, the interpolation error can be calculated using Eq. 34:

$$Err = \max \left| \frac{T_{int}^k - T(y)}{T(y)} \right| \quad y \in [y_1^i, y_2^k] \quad \text{Eq. 34}$$

The Err parameter, is the absolute maximum of the relative error between the analytical temperature distribution and its interpolation. Due to the complexity of the Rosenthal function, an analytical solution is hardly practicable and the most convenient way to identify it is by means of numerical techniques. Once the error value for the current guess is computed, the following check (Eq. 35) is performed:

$$Err \geq Err_t \quad \text{Eq. 35}$$

Where Err_t is the target error value. Basically, this condition is the stopping criterion for the boundary search algorithm: as shown in Figure 4.29 (b), if the s parameter is kept much smaller than b , the Err parameter will increase with the number of guesses, allowing to trigger the target error value, i.e., providing the maximum mesh size that allows to reach the required accuracy. If the stopping criterion is not met, then another guess is performed, calculating the zone upper bound as shown in Eq. 36:

$$y_2^{k-1} = y_1^i + (k + 1)s \quad \text{Eq. 36}$$

Otherwise if the criterion is met, another zone will be analyzed, after the calculation of its lower bound and the mesh size for the current zone, according to Eq. 37 and Eq. 38:

$$y_1^{i+1} = y_2^i = y_2^k \quad \text{Eq. 37}$$

$$d_{el}^i = y_1^{i+1} - y_1^i \quad \text{Eq. 38}$$

It must be pointed out that the error parameter should not be regarded as the value of the expected discrepancy between the FE model and the experimental data. Such parameter represents the capability of a specific mesh to interpolate a reference temperature profile, hence its theoretical maximum precision to fit the estimated temperature distribution.

The proposed discretization technique was validated by means of a two-step approach: a numerical and an experimental one. The former was carried out to evaluate the accuracy of the proposed technique to predict the base plate temperature distribution, with respect to a reference model. On the other hand, the experimental validation was carried out to verify the effect of the achievable accuracy in temperature prediction on the mechanical calculation.

Numerical validation of the proposed technique

This paragraph depicts the numerical validation of the proposed technique.

The test case used for the numerical validation is presented in Figure 4.30: it is a single weld bead, deposited onto a square plate substrate.

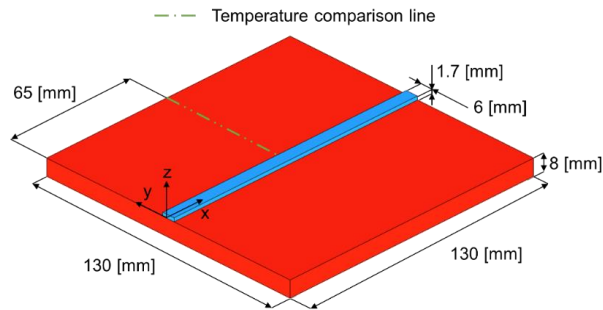


Figure 4.30: Geometry of numerical validation models.

The test case model was discretized using both the proposed technique and the mesh biasing approach, to compare their performances. A reference model was created discretizing all the substrate to meet the mesh size requirement of the weld bead. The accuracy of the FE models was compared analyzing the temperature profile along the comparison line (Figure 4.30) at the simulation time in which the heat source was located at $x=65$ mm. All the FE simulations were carried out using first order hexahedral elements. Due to the symmetry of the test case, only half of its geometry was discretized: Figure 4.31 shows yz cross sections of the FE models used in this validation stage.

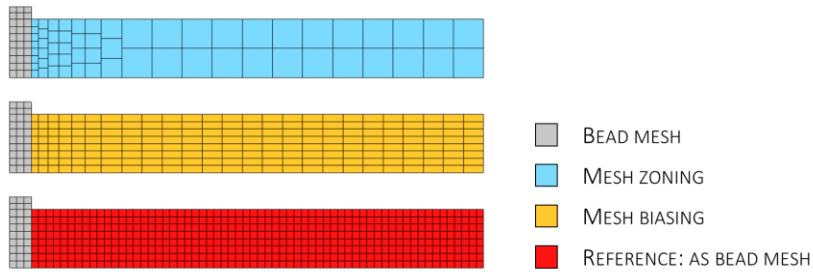


Figure 4.31: Comparison of mesh biasing, mesh zoning and reference models.

The proposed model was created setting the maximum error parameter (Err_i) of the proposed mesh size identification algorithm equal to 5%. This led to a FE model composed by 7768 hexahedrons, with a maximum elements aspect ratio not exceeding 1.2. The mesh biasing model was created with the constraint of not exceeding a limit value of the elements maximum aspect ratio (limit value: 3.0), leading to a FE model made of 29900 hexahedrons. In all the FE models, weld bead was discretized with three elements per half width and two elements per thickness. The region underneath the weld bead was discretized using the same mesh size. Following these guidelines, the reference model was composed by 68380 hexahedrons.

The FE simulation was carried out considering a total heat input per unit time of $2.8e+3$ W, and a welding head travelling speed of 300 mm/min. The proposed heat source model was used, setting the heat source dimensional parameters according to Table 4.8.

Table 4.8: Heat source dimensional parameters used for the numerical validation

Heat source dimensional parameters [mm]								
a_f	a_r	b	c	f_f	f_r	w_l	h_l	l_l
1,4	3,5	3.0	3.0	0.6	1.4	3.0	1.7	1.44

The simulations were carried out using the material properties defined in the beginning of the section. The latent heat of fusion was included according to the proposed model.

Figure 4.32 summarizes the validation results: in Figure 4.32 (a), the temperature profile on the comparison line computed by the reference model is presented. Figure 4.32 (b) shows the percentage errors of the mesh biasing and the proposed models with respect to the reference one. Figure 4.32 (b) clearly highlights that both the element-saving strategies lead to reduced percentage errors in estimating the reference temperature profile (below 5%). The mesh biasing model shows a slightly lower error than the proposed one. This might be due to the larger number of elements used to discretize the comparison line in the mesh biased model, as required to meet the maximum aspect ratio constraint.

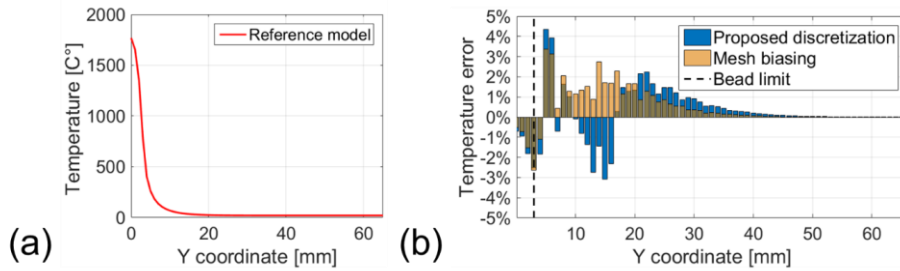


Figure 4.32: Reference model temperature profile (a); biased and proposed models error (b).

The other aspect to be considered is the simulation time. Table 4.9 compares the elapsed time of the reference, mesh biasing and proposed models. The mesh biasing allowed achieving a great reduction in computational time with respect to the reference one. However, with the proposed model a further improvement was achieved, reducing the computational time of about 70% with respect to the mesh biasing model. This significant difference in simulation time is related to the lower element number used to discretize the proposed model, compared to the mesh biasing one.

Table 4.9: Elapsed simulation time for the different substrate discretization.

Simulation times [s]		
<i>Reference model</i>	<i>Mesh biasing</i>	<i>Proposed model</i>
26481	10099	3182

In summary, the proposed model returned an accurate prediction of the reference temperature field and allowed to significantly reduce the simulation time. Despite the proposed mesh zoning leads to a slightly larger temperature error with respect to the mesh biasing one, this lack of accuracy might be negligible compared to the great reduction of simulation time provided by the proposed model.

Experimental validation of the proposed technique

The numerical validation confirmed that the proposed discretization technique returns an accurate prediction of the substrate temperature distribution. As already mentioned, one of the main purposes of AM simulation is the prediction of workpiece mechanical response in terms of distortions and residual stresses. To test the effect of the proposed mesh coarsening on the accuracy of mechanical analysis, an experiment was performed. A test-case workpiece was manufactured using the WAAM machine presented in section 3.2. The workpiece distortions were then measured and compared with process simulation results.

The test case used for the experimental validation is shown in Figure 4.33.

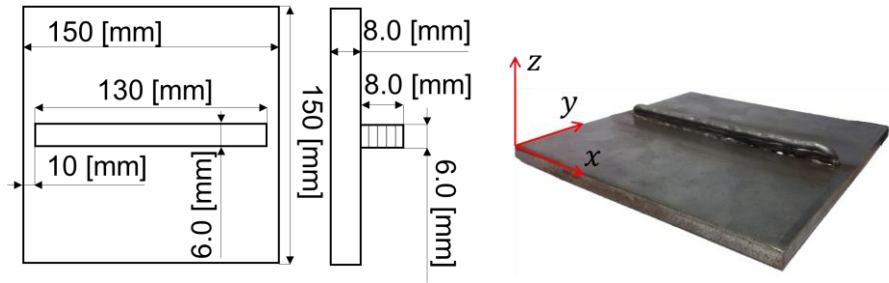


Figure 4.33: Test case dimensions and actual appearance.

Basically, it consists in a 5 layers wall, i.e., a series of straight beads deposited onto a plane substrate. The substrate is made of S235JR structural steel, while the deposition was carried out using a ER70S-6 0.8 mm metal wire, that is a standard filler material for carbon steel welding. The deposition process was performed using a Millermatic 300 GMAW welding unit. The process parameters used for test case manufacturing are summarized in Table 4.10.

Table 4.10: Process parameters used to manufacture the test case.

Process parameters	
Average welding voltage	19 [V]
Average welding current	81 [A]
Electrical power	1480 [W]
Wire feed speed	4.6 [m/min]
Travelling speed	300 [mm/min]

The test case was constrained with an isostatic scheme during the deposition process. This fixture scheme was realized supporting the base plate on three rest points. This strategy was preferred to avoid modeling the boundary conditions and the unclamping simulation that could affect the validation analysis. Hence, only the deposition and cooling phases were simulated, without including the unclamping in the FE analysis. The workpiece distortions were measured by means of a Mitutoyo Euro Apex C776 CMM (Coordinate Measurement Machine), probing the top surface of the base plate, i.e., the x - y plane corresponding to $z=0$, (Figure 4.33). The workpiece was scanned before and after the deposition to take the base plate unevenness into account when comparing the distortions. Based on the preliminary measurement of the substrate, the geometry of the FE model top surface was updated projecting the top surface nodes on the actual top surface geometry.

The FE modeling of the test case was carried out using the procedures described for the numerical validation models. The substrate discretization was carried out using the proposed technique. The mesh size selection algorithm was run using 10% as maximum error parameter. This lead to a model size of 21742 hexahedrons and 13627 nodes. The mesh coarsening pattern is shown in Figure 4.34.

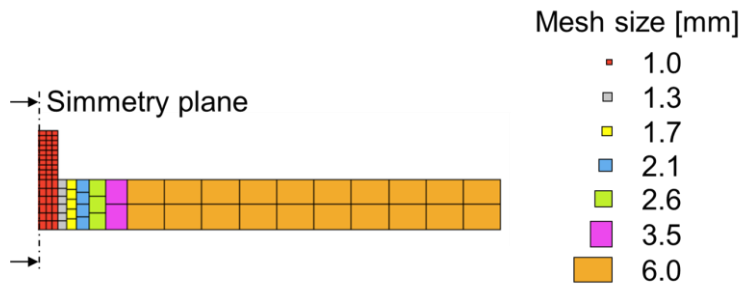


Figure 4.34: Mesh size pattern for the wall model.

The weld beads were discretized using three elements per half bead width and two elements per bead thickness. The heat source dimensional parameters were set according to the values used for the numerical validation.

For the heat transfer analysis, free convection BCs (Boundary Conditions) were assigned on the substrate top and bottom surfaces and on the wall surface, with heat transfer coefficients equal to $8.5 \text{ W/m}^2\text{K}$, $4.0 \text{ W/m}^2\text{K}$, $12.0 \text{ W/m}^2\text{K}$ respectively. The heat transfer coefficients were computed using literature correlations for free convection [117]. A general radiation to environment BC was included, setting the material emissivity to 0.2 [132]. For both the convection and radiation BCs, the room temperature was set to 298.16 K.

Both thermal and mechanical material properties were set according to the indications provided in the beginning of the section.

The model accuracy in predicting the workpiece mechanical response was evaluated comparing the deformed top surface of the actual plate and the simulated one. Figure 4.35 compares the experimental and simulated surfaces.

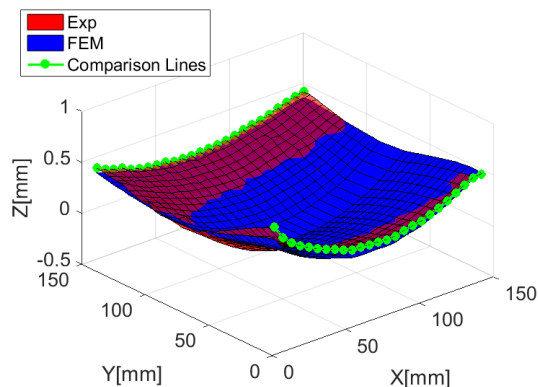


Figure 4.35: Predicted and experimental top surface deformed geometry.

To provide a better insight on the simulation accuracy, the two edges of the top surface in the X direction (green lines with round markers in Figure 4.35) are shown separately in Figure 4.36.

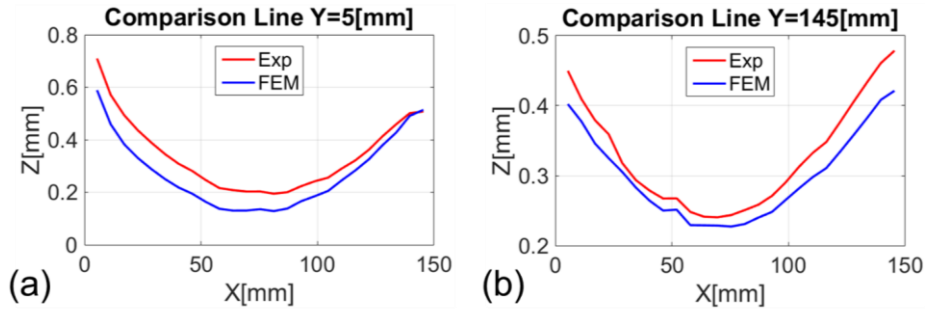


Figure 4.36: Predicted and experimental comparison lines at: Y=5mm (a) and Y=145 mm (b).

These figures show that the FE simulations results are in general agreement with the experimental ones. Indeed, the surface curvature are quite similar, with a maximum error of 0.16 mm on the z position. This result is in line with what presented in previous works concerning WAAM simulation [138],[142] and it is compliant with the accuracy required by practical applications of the process simulation. Moreover, the simulation was carried out using literature data and correlations for material properties and heat transfer coefficients and without any model updating operations to identify the heat source parameters. This suggests that the simulation accuracy could be improved with a better estimate of the input parameters. In summary, the simulation carried out by means of the proposed discretization techniques achieves an accuracy level compliant with literature data, for what concerns workpiece distortions, confirming the results obtained in the numerical validation.

In conclusion the proposed mesh coarsening technique enables an accurate simulation of the mechanical and thermal behavior of the workpiece during the WAAM process with a significant reduction of the calculation time. Besides it provides a systematic tool to define the mesh size of the substrate a priori, i.e. without time consuming convergence analyses.

4.4. Conclusions and remarks

This thesis proposes three advancements respect to the current state of the art of WAAM macro scale simulation: a new heat source model, an enhanced latent heat model and a mesh coarsening technique to reduce the elements required to discretize the workpiece substrate. The latent heat model and the mesh coarsening technique were explicitly developed to reduce the calculation time, increasing the time efficiency of the WAAM simulation. On the contrary, the proposed heat source model allows to overcome an accuracy issue of the state of the art solution. However, it is pinpointed that, unlike the state of the art method, the proposed heat source model does not require specific tuning operations, reducing the model pre-processing time.

Finally, it is worth to highlight that the proposed techniques do not aim to replace the state of the art solutions. On the opposite, the aim is to propose a series of improvement which can be integrated with the state of the art techniques to further increase the time efficiency of WAAM simulation. As an example, the state of the art remeshing techniques could be easily combined with the substrate mesh coarsening algorithm.

The thesis contributions to the state of the art are remarked in Table 4.11.

Table 4.11: Summary of the thesis contributions to the WAAM simulation SoA.

Heat source: <i>Thesis contribution</i>
Novel heat source model tailored for GMAW [1]:
Increased accuracy and reduction of tuning operations
Increasing of simulation time step: <i>Thesis contribution</i>
Novel latent heat modelling technique [2]:
Increasing of the minimum time step requirements
Decreasing of required DOFs: <i>Thesis contribution</i>
Novel substrate mesh coarsening technique [2]
Reduction of the DOFs required to discretize the workpiece substrate

5. Application of WAAM simulation

The previous chapter presented the work carried out to improve the current WAAM macro-scale simulation techniques in terms of achievable accuracy and computational efficiency.

The aim of this chapter is to show the practical application of the presented modelling techniques, by tackling an issue that affects the WAAM process: the heat accumulation. Such phenomenon can be the source of several problems during the manufacturing process, such as structural collapses or non-homogeneous mechanical properties. In this section the proposed modelling techniques are used to test and develop two approaches to mitigate this issue:

- Jet impingement cooling.
- Idle time selection.

The first proposed approach is to apply the jet impingement cooling to the WAAM process, namely to use a cooling technique, well-established in other sectors, to increase the convective heat flux, preventing the heat accumulation. The proposed model is used to test the effectiveness of the proposed solution.

The second proposed approach is to use the process simulation to schedule the interlayer idle times, namely time intervals between each layer in which the workpiece can cool down to a target interpass temperature. The identification of the cooling times is achieved through a dedicated algorithm based on the process simulation.

The contents of this chapter are structured as follows:

5.1 Heat accumulation issue in WAAM: this section depicts the heat accumulation issue, highlighting its causes and effects. The available state of the art techniques used to tackle such issues are presented, discussing their advantages and drawbacks.

5.2 Heat accumulation issue in WAAM: this section describes the jet impingement cooling application to the WAAM process. The proposed cooling system is described together with the numerical procedure used to assess its effectiveness.

5.3 Idle times selection technique: this section describes the proposed model-based approach to schedule the interlayer idle times. The proposed algorithm is presented together with an experiment carried out to test its effectiveness.

5.4 Conclusions and remarks: this final section will summarize the proposed contribution, providing conclusive remarks.

5.1. Heat accumulation issue in WAAM

During the deposition process, the arc transmits a large amount of heat to the workpiece, melting the filler material and forming the molten pool. The heat of the molten pool is transmitted to the surrounding workpiece material and to the environment. As shown in Figure 5.1, the main modes of heat transfer are: conduction through the workpiece towards the substrate; convection and radiation to the environment.

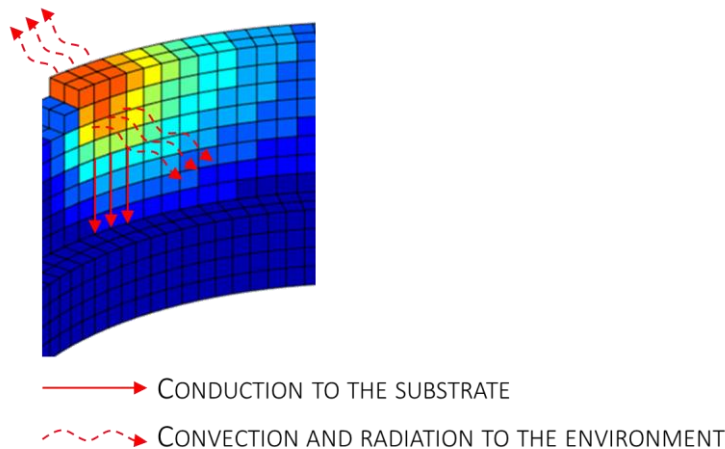


Figure 5.1: Modes of evacuation of the molten pool heat.

Several works [149,150] showed that the dominant heat transfer mode is the conduction to the substrate. The reason of this is twofold: first the thermal conductivity of the metal is generally high, leading to a high magnitude of the conductive heat flux; second the heat transfer between the workpiece and the room air usually occurs in free convection conditions, leading to poor transfer coefficients. However, the conductive heat flux depends on the distance between the substrate and the molten pool, i.e. on the number of deposited layers. This effect was shown by Zhao et al. [150] which performing FE simulations and experiments highlighted a significant reduction of the temperature gradient in the substrate direction with the increase of the number of layers. This leads to the phenomenon of heat accumulation, i.e. an increase of the workpiece average temperature with the increase of the number of layers. This phenomenon has a detrimental effect since it modifies the following process variables:

- The interpass temperature.
- The molten pool size.

The interpass temperature is the workpiece temperature at the start of a layer deposition. The heat accumulation phenomenon leads to a progressive increase of the interpass temperature. This parameter was found out to be a crucial in WAAM process: Zhao et al. [87] showed that decreasing the interpass temperature can reduce the magnitude of the

residual stresses; Geng et al. [85] stated that controlling the interpass temperature is essential to avoid bead defects and to prevent part collapse. Besides, the interpass temperature selection is fundamental to avoid solidification defects and to achieve adequate material properties: Shen et al. [70] investigated the influence of interpass temperature on WAAM processing of iron aluminide alloys, concluding that it has a significant influence on yield stress, elongation and longitudinal cracking occurrence; Ma et al. [151] studied the titanium aluminides alloys finding a significant influence of interpass temperature on the local chemical composition, microstructure, phase concentration and microhardness. In light of the aforementioned literature recommendations, it is crucial to control the interpass temperature during the WAAM process.

The other parameter affected by the heat accumulation phenomenon is the molten pool size. The heat accumulation can lead to an increase of the molten pool size with the increase of the layers. An excessive increase in the molten pool size can lead to detrimental phenomena such as the occurrence of structural collapse due to the reduced dimensional stability of the excessively hot workpiece [16,152]. Figure 5.2 shows an example of such phenomenon: a cylindrical workpiece was affected by an excessive heat accumulation which led to the increase of the molten pool size with consequent collapse of its external surfaces.

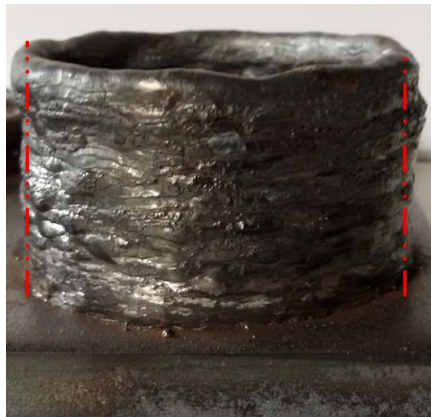


Figure 5.2: A WAAM component affected by structural collapse, highlighted by the non-vertical pattern of the cylindrical surface.

Besides the structural collapse, the molten pool size has a significant influence on both the temperature gradient and the cooling rate. The excessive increase of the molten pool size can thus lead to non-uniform mechanical properties along the workpiece height. This phenomenon was observed by several authors. Wang et al. [92] analyzed the mechanical properties of WAAM processed Inconel 625 at different distances from the substrate. A significant reduction of both ultimate tensile strength and yield stress was found in the samples located further from the substrate. The molten pool size was measured using a high-speed camera, finding a significant increase in its size in the top layers. This increase in the molten pool size determined a segregation of the Laves phases, resulting in the reduction of the yield and tensile strengths. A similar effect was found by Zhang et al. [46] while working on stainless steel components. Liberini et al. [153] highlighted differences in both the microhardness and the phase content along the height of WAAM processed ER70S-6 workpieces. Figure 5.3 shows the pattern of the micro-hardness found in this work.

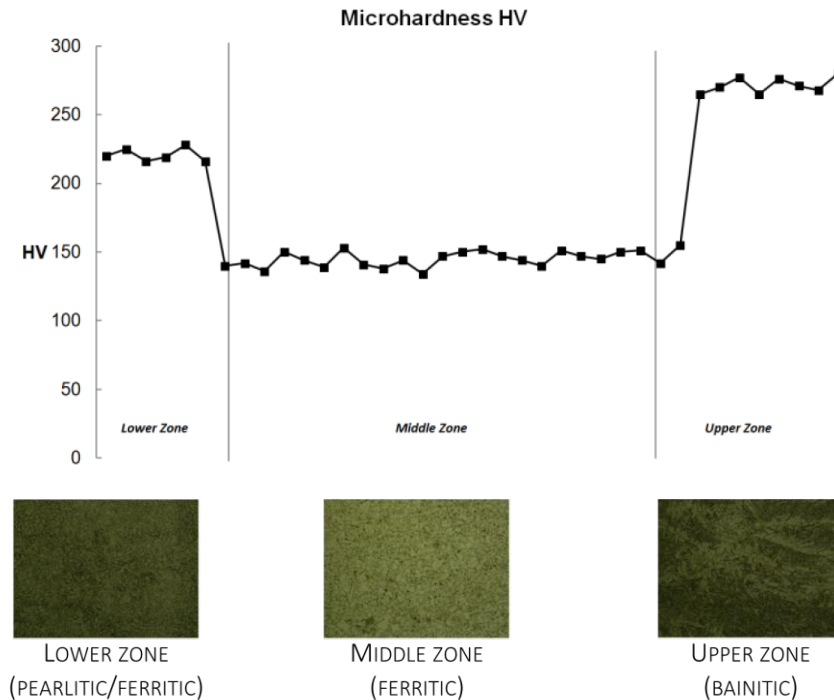


Figure 5.3: Different microhardness and phase content along the workpiece height in WAAM processed ER70S-6 [153].

It is highlighted that the microhardness is higher in lower zone, because of the heat sink effect of the substrate. Consistently, this area exhibits a perlite/ferrite microstructure, typical of a rather quick cooling. On the opposite, in the central part the hardness is significantly lower and the material has a ferritic microstructure. This is a consequence of the reduced cooling rate due to the increase of the molten pool size. Finally, the top layer exhibits the highest microhardness and a bainitic structure. This is expected since the last layer does not undergo any re-melting.

This analysis highlights that, tackling the heat accumulation phenomenon is an important task, both to control the interpass temperature and to limit the increase of the molten pool size. According to literature, two main paths can be pursued to mitigate such issue:

- Introduce interlayer idle times.
- Increase the heat transfer rate.

The first solution consists in introducing idle times between the layers, i.e. time intervals in which the workpiece is allowed to cool down [110]. During the idle times the workpiece cools down transferring the accumulated heat to the environment. This allows reduce the amount of heat accumulated by the workpiece and to control the interpass temperature. However, a significant issue is the scheduling of the idle times values. Currently this is achieved by two main techniques: fixed idle times selection and substrate

temperature monitoring. The former one consist in introducing a fixed idle time at the end of each layer in the deposition part program [86]. This technique allows the workpiece to cool down, but it requires a series of pre-tests to set the correct idle time. Besides, using fixed idle times might not allow to maintain a constant interpass temperature, due to the aforementioned reduction of the conductive heat flux [150]. Hence, to provide the same interpass temperature, the idle time should increase as the deposition progresses. This is usually achieved by monitoring the substrate temperature by means of a sensor (usually a thermocouple). After the deposition of a layer, the process is kept idle until the thermocouple signal reaches the prescribed value. Despite this technique allows to keep the substrate temperature constant at the end of each layer, it does not allow to achieve a constant molten pool size, i.e. increasing the distance between current layer location and the substrate, the molten pool increases its volume, as shown by Wang et al. [92].

An alternative approach to the idle times is to increase the heat transfer rate between the workpiece and the environment, preventing an excessive increase of the workpiece internal energy. This can be achieved by two main approaches: increasing the substrate heat sink effect or increasing the convective heat flux. The substrate heat sink effect is usually increased using water cooled fixtures, as shown by Karunakaran et al. [43] and by Ding et al.[138]. This approach enables a faster cooling of the workpiece, but the molten pool heat is still mainly dissipated through conduction. Hence this solution does not allow to keep the cooling rate and the molten pool size constant along the component building direction. The second strategy, i.e. increasing convective heat flux, was implemented by Sasahara et al. [154,155], using a WAAM facility in which the workpiece is immersed in a water cooled tank. This approach was shown to be extremely effective in preventing an excessive heat accumulation. However the usage of a water cooled tank is not compliant with the usage of existing equipment to perform WAAM operations, an important standpoint of such technology [74].

Table 5.1 summarizes the state of the art techniques used to prevent and mitigate the detrimental consequences of the heat accumulation.

Table 5.1: Summary of the state of the art techniques to mitigate the heat accumulation issue.

Limitation of heat accumulation	
<i>Idle times</i>	
Zhao et al. [86] Mughal et al. [87]	Fixed idle times
Chiumenti et al. [112]	Substrate temperature monitoring
<i>Increase of the heat transfer rate</i>	
Karunakaran et al. [43] Ding et al.[138]	Water cooled fixtures
Sasahara et al. [154,155]	Water cooled workpiece tank

The aim of this thesis is to improve both the techniques used to tackle the heat accumulation, proposing:

- A cooling system based on the air jet impingement technique that allows to achieve a high heat transfer rate but is compliant with existing machines.
- An idle time scheduling technique that takes the reduction of the conductive heat flux into account, allowing to schedule the idle times in pre-process phase without the need of installing additional sensors on the machine.

5.2. Jet impingement application to the WAAM process

This thesis proposes to use the jet impingement cooling system to increase the convective heat flux to environment in WAAM operations. This technique consists in cooling a target surface by means of an impinging fluid jet. It is already used for several applications requiring high heat flux per surface, including other manufacturing processes [156]. The proposed approach is to cool the workpiece by means of an air jet conveyed on the deposited material surface by means of a coolant hose mounted on the deposition head. To further increase the cooling rate, low temperature air can be supplied to the hose by means of a vortex tube. This device allows to generate a chilled air flow without heat exchangers or moving mechanical parts, making it simple to be applied in a manufacturing environment [157]. Hence, the proposed cooling system could be easily installed on existing welding facilities or machine tools and would require just a standard compressed air supply. Furthermore, it would provide a local cooling effect, allowing to decrease the cooling rate differences in the workpiece.

This thesis aims at assessing the effectiveness of jet impingement cooling in WAAM, by means of a numerical investigation, i.e. including the jet impingement heat transfer into a FE (Finite Element) thermal model of the WAAM process. This strategy, in opposition to an empirical approach, will enable future optimization of the cooling system, testing different flow parameters or jet orientation and positioning. To achieve the proposed goal, a model of the jet impingement is implemented in the FE solver used to simulate the WAAM process (LS-DYNA). The proposed modelling technique was then verified by means of dedicated experiments. Finally, a WAAM operation was simulated, comparing the results obtained with and without jet impingement. This allows to assess of the effectiveness of proposed system.

Jet impingement modelling: overview

Figure 5.4 presents an archetype of the arrangement of the proposed cooling system. The coolant hose is fixed on the support of the welding torch, thus moving synchronously with the deposition head. This layout would enable to maximize the cooling effect of the air jet, conveying it close to the hottest region of the workpiece. It must be pointed out that this is a hypothesis of possible configuration, used as a reference to implement the jet impingement model.

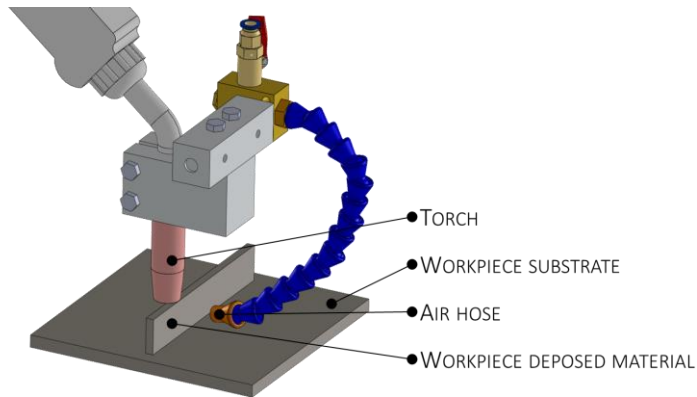


Figure 5.4.: Archetype of proposed cooling system.

To integrate the jet impingement effect, in a FE model of the WAAM process, a suitable convective boundary condition must be prescribed on the target surface of the workpiece FE model. The convective heat transfer, between a fluid and a surface of a solid body, is given by the Newton's law:

$$\dot{q} = h(T_s - T_\infty) \quad \text{Eq. 39}$$

Where \dot{q} is the heat flux per unit surface, T_s is the local surface temperature, T_∞ is fluid reference temperature and h is the transfer coefficient. The specific case of jet impingement is a complex phenomenon, since both the fluid temperature and the heat transfer coefficients have non uniform values over the target surface [158]. Nevertheless, due to the large number applications, many empirical correlations [159] are available to calculate local values of both these quantities. An analysis of scientific literature was carried out, identifying two correlations: one for the heat transfer coefficient and one for the fluid reference temperature. Both correlations were then implemented in LS-DYNA, to define a suitable boundary condition. The following paragraphs present the correlations used to calculate the convective coefficient and the fluid reference temperature respectively and their implementation in LS-DYNA.

Jet impingement modelling: heat transfer coefficient

The correlation selected to calculate the heat transfer coefficient is the one proposed by Goldstein and Franchett [160] since it provides local values of the heat transfer coefficient and it was developed testing a wide range of fluid flow and geometrical parameters. These features make the correlation suitable to investigate the effectiveness of jet impingement on WAAM. The correlation returns the non-dimensional form of the heat transfer coefficient, namely the Nusselt number, as shown in Eq. 40:

$$u = A Re^{0.7} \exp[-(B + C \cos\phi)(r/d)^{0.75}] \quad \text{Eq. 40}$$

Where d is nozzle outlet diameter; Re is the Reynolds number; the parameters r and ϕ define the position of the surface points in the coordinate system x_j, y_j, z_j , defined as

shown in Figure 5.5. z_j is directed according to the target surface normal, x_j is directed according to the projection of nozzle axis on the target surface and y_j is defined in accordance with the right-hand rule.

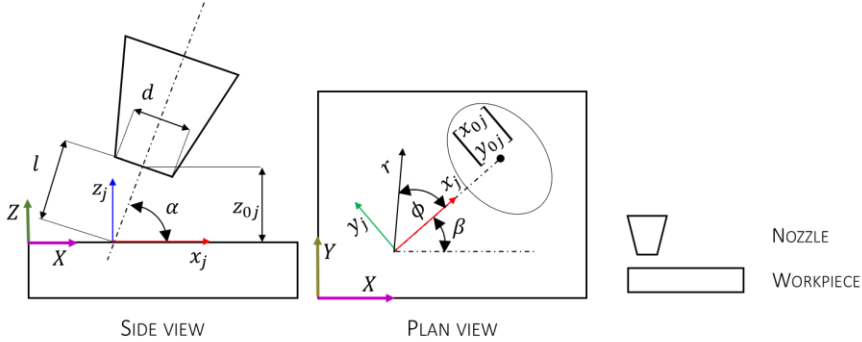


Figure 5.5: Geometric parameters of a generic jet impingement system.

The values of the parameters A , B and C are given in [160] as functions of the nozzle angle α (Figure 5.5), and of the l/d ratio, i.e. of the distance between nozzle outlet and the target surface. The Nusselt and Reynolds numbers for this correlation are defined according to Eq. 41:

$$\begin{cases} Nu = \frac{hd}{\lambda_f} \\ Re = \frac{U_m d}{\nu_f} \end{cases} \quad \text{Eq. 41}$$

Where U_m is fluid flow average velocity in the nozzle outflow section, λ_f and ν_f are respectively the fluid thermal conductivity and kinematic viscosity. In summary, once that the nozzle geometry, the mass flow rate and the nozzle to surface distance and inclination are known, the correlation coefficients can be calculated. The correlation can finally be used to calculate the local values of the heat transfer coefficient.

Jet impingement modelling: fluid reference temperature

According to Eq. 39, a fluid reference temperature must be defined to calculate the convective heat flux. Most of the literature correlations use nozzle outflow temperature as reference value. According to Goldstein et al. [161], this is correct only in case of ambient temperature jet. For different outflow temperature, the mixing between jet and ambient air modifies flow temperature, leading to inaccuracies in the heat flux calculation. The solution to overcome this issue is to use the jet adiabatic wall temperature [162], i.e. the fluid flow temperature evaluated in the vicinity of the target surface, in the condition of no heat transfer between the flow and the surface. It must be pointed out that as the heat transfer coefficient, the adiabatic wall temperature is not constant over the target surface. Hence it must be computed using specific literature correlations. This thesis refers to the work of Hollworth and Wilson [163] for the adiabatic wall temperature calculation. Hollworth and Wilson provided the data of a large set of experiments, that can be used to compute the local values

of the adiabatic wall temperature from jet parameters. In this thesis, such data are interpolated by means of spline curves. This enables to integrate the correlation in the FE solver. As for the heat transfer coefficients, the adiabatic wall temperature data are given in terms of the non-dimensional parameters defined in Eq. 42:

$$\begin{cases} \eta_1 = \eta_1(l/d) = \frac{T_{ws} - T_a}{T_{0j} - T_a} \\ \eta_2 = \eta_2(r/r_{12}) = \frac{T_w - T_a}{T_{ws} - T_a} \end{cases} \quad \text{Eq. 42}$$

Where T_w is the local value of the adiabatic wall temperature; T_{ws} is the adiabatic wall temperature at the stagnation point (i.e. $r = 0$ for a vertical jet); T_a is the ambient air temperature; T_{0j} is the jet outflow total temperature; r_{12} is the jet half width, evaluated as a function of l/d [163]. According to Eq. 42, the procedure to obtain the local values of adiabatic wall temperature is the following: first η_1 is calculated from l/d , allowing to determine T_{ws} ; then r_{12} is calculated from l/d , allowing to compute η_2 for the required values of r . Finally, T_w is computed from η_2 and T_{ws} . The curves used to calculate the non-dimensional parameters are shown in Figure 5.6. It is interesting to pinpoint that T_w is not dependent on the Reynolds number, i.e. on jet flow rate.

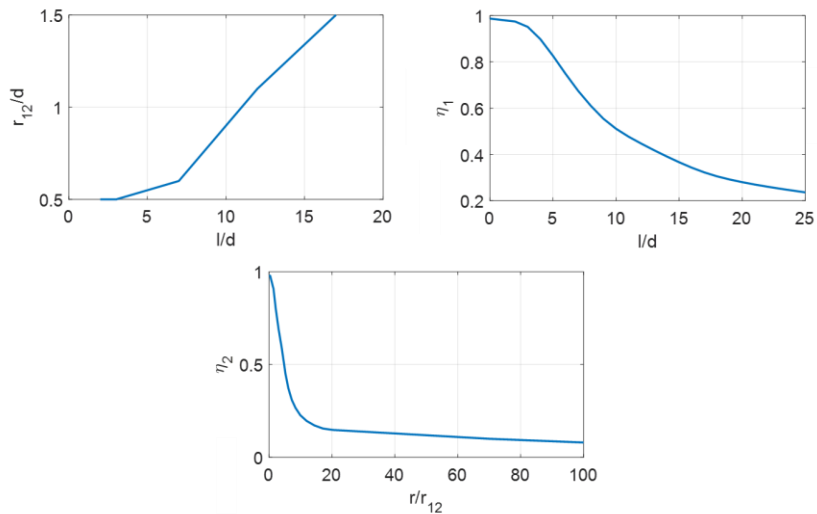


Figure 5.6: The curves used to calculate non-dimensional adiabatic wall temperature.

Jet impingement modelling: implementation in LS-DYNA

The aforementioned models of jet impingement heat transfer are implemented in the LSDYNA. Such model allows to include the effect of a moving jet, impinging on a plane wall. The convection boundary condition is included via the *BOUNDARY_CONVECTION [123] option. To implement the presented correlations, both

heat transfer coefficient and adiabatic wall temperature are defined as functions of time and global coordinates, i.e. the coordinate system in which the FE nodes are defined. This was achieved by means of the *DEFINE_FUNCTION option. In this paragraph, the general workflow of such functions is presented. First a coordinate transformation is applied to get the coordinates of the current evaluation point in the local system x_j, y_j, z_j defined in Figure 5.5. The coordinate transformation is presented in Eq. 43, referring to Figure 5.5 case:

$$\begin{cases} x_j = X - \{x_{0j}(t) + |Z - z_{0j}(t)| \cotan(\alpha) \cos(\beta)\} \\ y_j = Y - \{x_{0j}(t) + |Z - z_{0j}(t)| \cotan(\alpha) \sin(\beta)\} \\ z_j = Z - z_{0j}(t) \end{cases} \quad \text{Eq. 43}$$

Where X, Y and Z are the global coordinates (Figure 5.5); x_{0j}, y_{0j}, z_{0j} are the coordinates of the nozzle center, given as time dependent functions (*DEFINE_FUNCTION_TABULATED in LS-DYNA), to take nozzle motion into account; β is the angle between the x_j and the X axis. Having evaluated current point coordinates, the implemented functions evaluate r and ϕ parameters, with a Cartesian to polar coordinates transformation. With this step, the transfer coefficient and the adiabatic wall temperature are calculated using the procedures described in the previous sections. If the target surface has a different orientation, the same coordinate transformation can be applied introducing a further coordinate system rotation.

Jet impingement model verification: overview

To verify the accuracy of jet impingement modelling, an experimental verification was carried out. The testing procedure consisted in cooling a target by means of an impinging jet while measuring its temperature. The same operation was simulated using proposed model, comparing the experimental and the numerical results. The target was a 250x250x8 mm steel plate, made of S235JR. The impinging air jet was generated through a vortex tube (Exair, Adjustable Spot Cooler). Two tests were carried out: first the target was cooled by the jet for 900 s, then the jet was removed allowing the plate to warm up for 900 s. The warm up test served as reference to verify the accuracy of FE model parameters such as material properties, radiation and free convection boundary conditions. The cooling test was used for the actual verification of the jet impingement model. First the experiments are presented. Then the details about the FE modelling procedure are given. Finally, tests results are presented and discussed.

Jet impingement model verification: test description

The experimental set up used for the verification is shown in Figure 5.7 (a). The target steel plate was positioned into the working area of the NMV1500DCG milling machine. The target was supported onto 4 rest points, avoiding the contact with machine table. Due to the small cross section of the supports, it was quite safe to assume that no heat transfer occurred between the plate and the machine. The vortex tube was attached to the z-axis of the machine, enabling an accurate positioning of its nozzle in the center of the plate. The cooling test was performed by positioning the axis of the orthogonal to the plate ($\alpha=90^\circ$) at a distance of 24 mm. Since the nozzle diameter is 6 mm, this distance corresponds to a l/d ratio equal to 4. Dried compressed air was supplied to the vortex by a 0.2 m³ plenum at a pressure of 6 bar. This inflow conditions led to an outflow total temperature of 265.3 K and a velocity of

54 m/s, corresponding to a Reynolds value of 31200. Air total temperature and velocity were separately measured by means of a k-type thermocouple and a pitot tube. The target plate temperature was measured by means of an IR camera (Flir EB-40), acquiring thermal images via the Flir Research-IR software. Figure 5.7 (b) shows a thermal image taken at the end of the cooling phase. A black paint coating was applied on the target surfaces, to increase their emissivity. Additionally, two k-type thermocouples were installed: one was attached in the center of the target lower surface, the other in the machine working area, far from the impinging jet. The former provided an additional measurement of the target temperature, while the latter provided a measurement of the room temperature, which was 294.5 K during the tests. The thermocouple signals were acquired using a National Instruments 9213 thermocouple module.

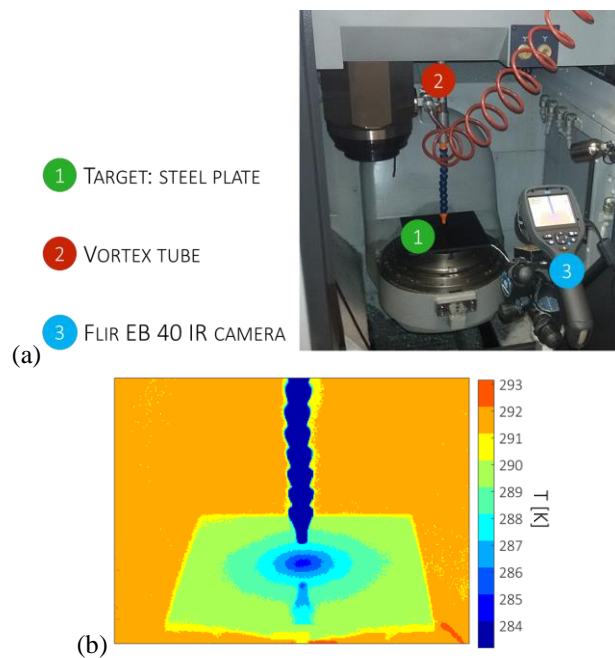


Figure 5.7: Testing equipment (a) and IR image of the target after 900 s of cooling (b).

Jet impingement model verification: FE modelling

Both the warm up and the cooling simulation were carried out as transient non-linear thermal analyses, using LS-DYNA. The steel plate was discretized using 7688 solid hexahedral elements. The material was modelled using temperature dependent properties presented in section 4.3. Simulations were carried out using a Crank-Nicolson time integration scheme. The time step was automatically adjusted by the solver, to keep the maximum temperature variation per time step below 0.5 K. In both simulations, radiation to environment was included: the emissivity was set to 0.9, since this value provided the best agreement of IR images with the thermocouple data; the radiating source temperature was set to the room value (294.5K). In the cooling simulation, free convection on the lower surface of the plate was considered, while in the warm up analysis, free convection was prescribed on both the plate faces. Free convection coefficients were included as temperature dependent

functions, according to literature correlations [117]. The initial conditions for the warm up simulation were set extracting temperature values from the IR image and prescribing such temperature distribution to FE model nodes, as shown in Figure 5.8 (a). In the cooling simulation, a uniform temperature value of 291.9 K was imposed as initial condition, based on the workpiece mounted thermocouple. The jet impingement was modelled using the proposed technique.

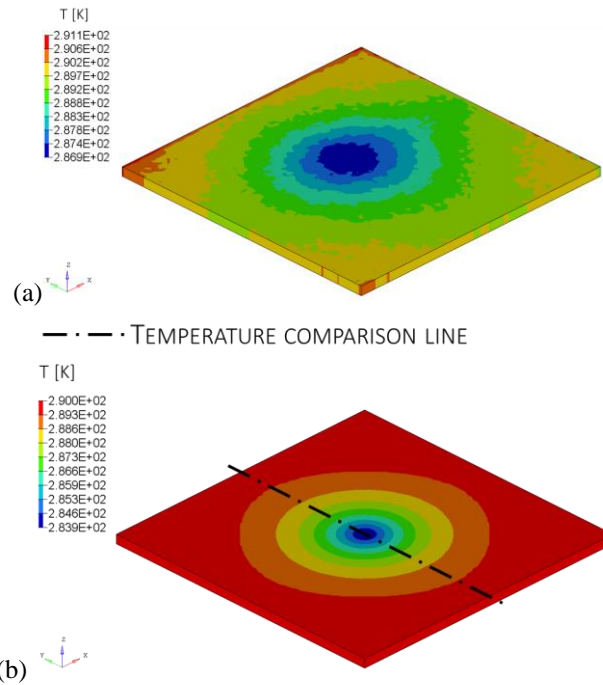


Figure 5.8: FE model: initial state of the warm up simulation (a); final state of the cooling simulation (b);

Jet impingement model verification: test results

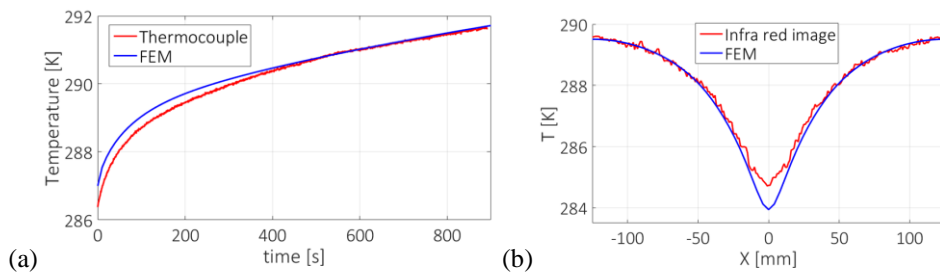


Figure 5.9: Comparison of tests and modelling results: time history during the warm up test (a); temperature profile at the end of the cooling test (b).

This paragraph presents the results of the verification, comparing the measured and the simulated data. For the warm-up test, Figure 5.9 (a) shows the comparison of the plate

mounted thermocouple, with the temperature time history of the FE model node located in the corresponding position. The thermocouple signal was chosen over the IR one since, after 50 s, the IR images showed a maximum temperature gradient of 2 K over the target surface. Hence thermal images do not provide any additional information to the thermocouple data that are more accurate in punctual temperature measurements. Figure 5.9 (a) shows that measured and simulated data are in good agreement since the maximum error does not exceed 0.5 K. This result suggests that the modelling assumptions concerning material and boundary conditions are compliant with the actual process physics, making the cooling test significant in providing a reliable feedback on the accuracy of jet impingement model.

The cooling simulation was verified comparing the numerical and the experimental (IR) temperature distributions at the end of the cooling phase (900 s). The analysis was carried out on the temperature profile along the comparison line shown in Figure 5.8 (b). This method was preferred over the time history comparison since, on the opposite of the warm up test, the plate experiences significant temperature gradients over the target surface. The verification result is shown in Figure 5.9 (b): it is highlighted that the proposed jet impingement model achieves an accurate prediction of the temperature profile, returning a maximum error of about 1 K in correspondence of the stagnation point. This result suggest that proposed modelling technique could be effectively used to analyze the influence of jet impingement on WAAM process by means of a FE simulation, provided that the same flow configuration is simulated.

Assessment of the jet impingement effect on WAAM: overview

The aim of this activity is to verify if an impinging air jet can increase the cooling rate during WAAM process, limiting the average temperature increase. This was achieved comparing the results of a WAAM operation simulated both in standard conditions and including the effect of jet impingement.

First the FE model used for the verification is introduced. Then the results are presented and discussed.

Assessment of the jet impingement effect on WAAM: FE model

The comparison was carried out simulating the manufacturing of a wall, i.e. a series of vertically stacked straight layers. An example of WAAM manufactured wall is shown in Figure 5.10 (a). The FE model of the wall is shown in Figure 5.10 (b): it is composed by 15 layers 6 mm wide and 1.6 mm thick deposited in the centerline of a 150x150x8 mm square plate. Since the component is symmetric, only half of it was discretized (Figure 5.10 (b)) using 12212 solid hexahedral elements. The effect of jet impingement was prescribed on the exterior surface of the wall, considering a nozzle moving according to the welding torch path. The jet impingement condition is activated at the beginning of the 5th layer deposition, with nozzle axis positioned at $z = 0$. This delay was prescribed since in the starting layers there is no need of additional cooling, due to the proximity of the substrate.

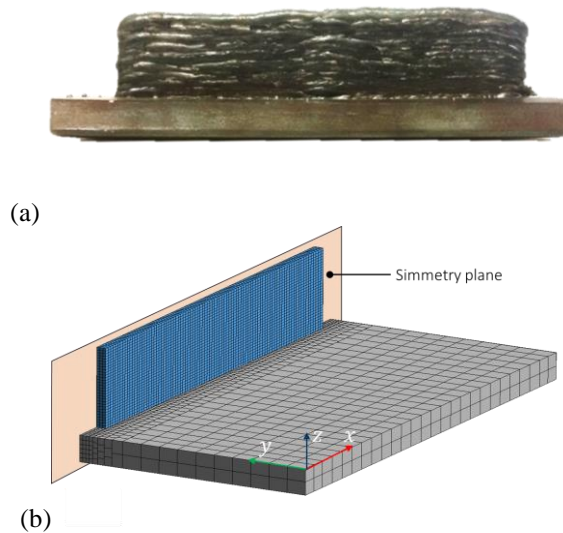


Figure 5.10: Example of a wall produced by WAAM process(a); FE element model used for the numerical test (b).

The heat transfer coefficient and the adiabatic wall temperature were calculated referring to the verified condition. Due to the symmetry condition, the simulation considered the effect of two symmetric impinging jet.

The WAAM process was simulated using the proposed modelling technique, described in section 4.3. The substrate material was S235JR structural steel, filler metal was ER70S-6 steel wire and the deposition was carried out at a travelling speed of 300 mm/min, considering an input power of 1480 W. For what concerns boundary conditions, both free convection and radiation to environment were included, considering a room temperature of 294.5 K. Convective coefficients and emissivity were set according to [1], except for the jet impingement simulation, where the free convection on the wall exterior surface is replaced by the jet impingement condition after its activation.

Assessment of the jet impingement effect on WAAM: results and discussion

The comparison of the reference and the jet impingement simulations shows that the impinging jet has a great influence on the WAAM process. Figure 5.11 compares the temperature field calculated in the reference and in the jet impingement simulation at 140 s and 350 s of simulation time, namely during the deposition of the 4th and the 10th layers respectively.

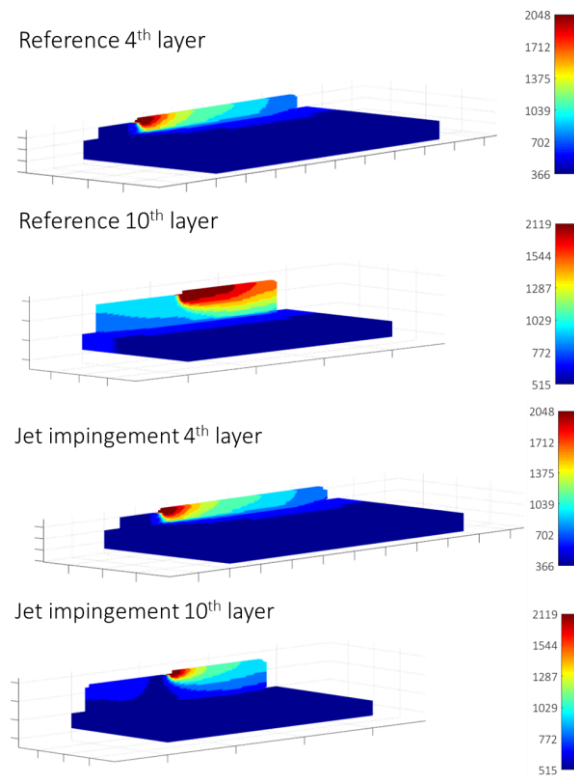


Figure 5.11: Comparison of temperature field of reference and jet impingement simulations during the deposition of 4th and 10th layers

It is highlighted that including the jet impingement effect in the simulation results in a considerable reduction of wall average temperature. In the reference model the amount of elements above the solidus temperature (1673 K) experiences a significant variation between the 4th and the 10th layer. On the opposite, in the jet impingement simulation the extension of such high temperature region is almost constant throughout all the simulation. At the 10th layer, the application of jet impingement allows to reduce the volume of the elements above the solidus temperature of about 87%.

The reduction of the wall average temperature is highlighted also by the temperature time histories. Figure 5.12 compares the reference and jet impingement simulation, showing the time histories of two nodes placed in the center cross section of the wall at different distances from the base plate (z axis Figure 5.10 (b)). It can be noticed that both the reference and jet impingement results show cyclic temperature peaks corresponding to the welding torch passage. The effect of the jet impingement is highlighted looking at the minimum value of these temperature cycles. Indeed, in the reference process, such value increases constantly throughout the whole simulation, i.e. the wall experiences an increase of its average temperature. On the opposite, when the jet impingement is used, the minimum value of the thermal cycles is almost constant after the jet activation.

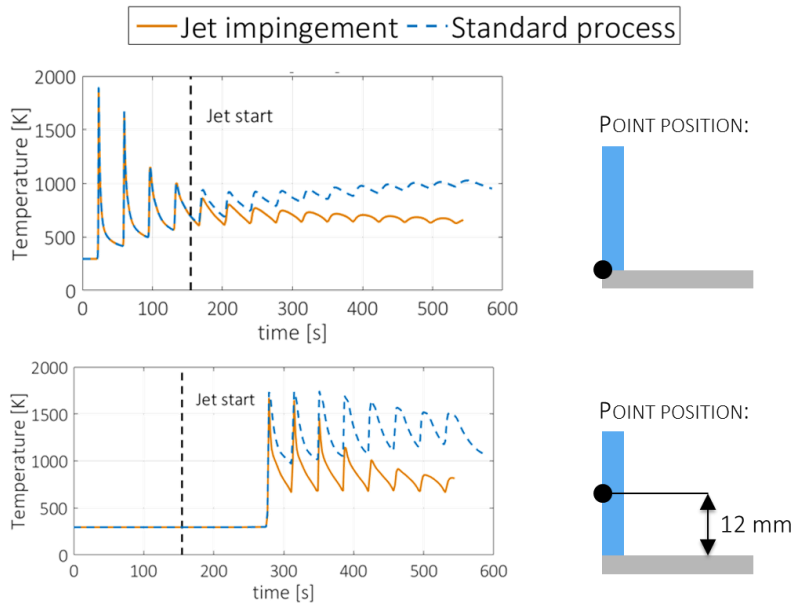


Figure 5.12: Comparison of temperature time histories at two different distances from the base plate.

In summary, the numerical comparison highlights that in the tested configuration, jet impingement has a significant influence on WAAM process. The increase in the heat transfer coefficient results in a significant reduction of wall average temperature, mitigating the risk of part collapse and allowing a higher deposition rate. Despite the investigation was carried out on a simple geometry, similar results are expected on more complicated parts, since in jet impingement the largest thermal fluxes occur in the stagnation region, minimizing the effect of surface curvature on heat exchange coefficient. In addition, due to the great influence on the process, proposed technique could be optimized to produce WAAM components with homogeneous metallurgical structure and mechanical properties.

5.3. Idle times selection technique

This thesis proposes an innovative FEM based technique to schedule the interlayer idle times for the WAAM technology. The interpass temperature is monitored during the simulation at a different point for each layer. Hence a different idle time is calculated for each layer, to ensure a constant interpass temperature on the last deposited layer. It is demonstrated that this approach significantly limits the increase of the molten pool size during the process. The calculated idle times can be introduced as dwells in the WAAM part program, ensuring the consistency between the simulated and the actual process. The usage of a FE simulation rather than sensor-based monitoring has a twofold advantage: it overcomes the issues related to temperature measurements in the workpiece areas close to the molten pool and it enables to perform sensitivity analysis using different interpass temperature. To verify its effectiveness, the proposed technique was used to schedule the idle times for the manufacturing of a test case component. Such part was then manufactured using the prescribed idle times. Finally, CMM measurements were carried out on the workpiece to verify the effect of proposed approach on the dimensional accuracy of the component.

Proposed technique: overview.

This thesis proposes a novel approach to calculate the idle times required to achieve a constant interpass temperature and to limit the increase of the molten pool size in WAAM operations. The base idea of the proposed approach is to monitor the cooling of each layer right after its deposition during a FE simulation of the process, calculating the required idle times to meet the interpass temperature constraint. Unlike the most common procedure of monitoring the substrate temperature in a set of fixed points, this technique associates a specific control point to each layer. This enables a local control of the interpass temperature, compensating for the reduction of the conductive heat flux. This is proven to result in constant molten pool size. The FE simulation provides the knowledge of the workpiece temperature field in an arbitrary point, a result hardly achievable by direct measurement [149]. Furthermore it is a consolidated practice for WAAM [138] and different metal AM processes [164].

The proposed approach consists in the following steps, repeated for each layer of the component:

- The deposition of the current layer is simulated, without any idle time at the end of the calculation.
- The final temperature field at the end of the simulation is prescribed as initial condition to a twin model of the workpiece. Then the natural cooling of the workpiece is simulated for a fixed amount of time, significantly higher than the time expected to meet the required interpass temperature constraint.
- The temperature time history of a predetermined node, serving as specific monitoring point for the current layer, is extracted from the cooling simulation results. Such data is analyzed, calculating the idle time associated to the current layer.
- At this stage, the deposition of the following layer is simulated, prescribing an initial idle time equal to the calculated one.

The following paragraphs provide a detailed description of the key aspect of the proposed technique: the control points positioning, the deposition and cooling simulation steps and the idle times calculation.

Proposed technique: control nodes positioning.

A control point is defined for each layer of the workpiece, to monitor its cooling after the deposition, allowing to calculate the required idle time to meet the target interpass temperature. In the simulation domain, the control points correspond to a set of FE nodes, located on the top surface of each layer at the end of its deposition path, i.e. the points of the deposition path where the idle time shall be introduced. Figure 5.13 shows this arrangement on a straight wall, used as sample components.

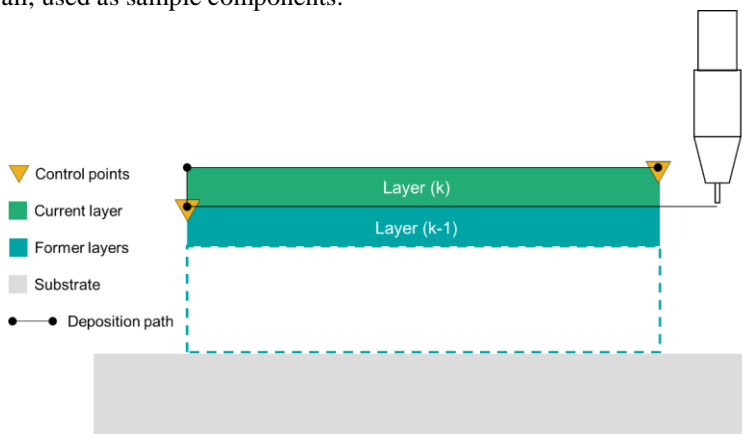


Figure 5.13: Control points location strategy.

In this case, the deposition is carried out following an alternate strategy, i.e. the deposition end points of subsequent layers (circle marks) lay on the opposite ends of the wall, resulting in an alternate positioning of the control nodes. Selecting the end of each layer as control point is a conservative strategy since it will be the point experiencing the highest temperature after the deposition. Hence, compared to other areas of the layer, it requires the highest idle time to achieve the target interpass temperature.

Proposed technique: deposition and cooling simulation.

The proposed approach is to calculate a specific idle time for each layer to fulfill the constant interpass temperature condition. The required cooling time is dependent on the amount of heat accumulated by the workpiece during the deposition and cooling phases of the former layers. Hence the idle times for each layer cannot be identified separately. On the opposite, the calculation for a layer must take the results of the former ones into account. This is tackled by using the simulation strategy outlined in the Figure 5.14 chart.

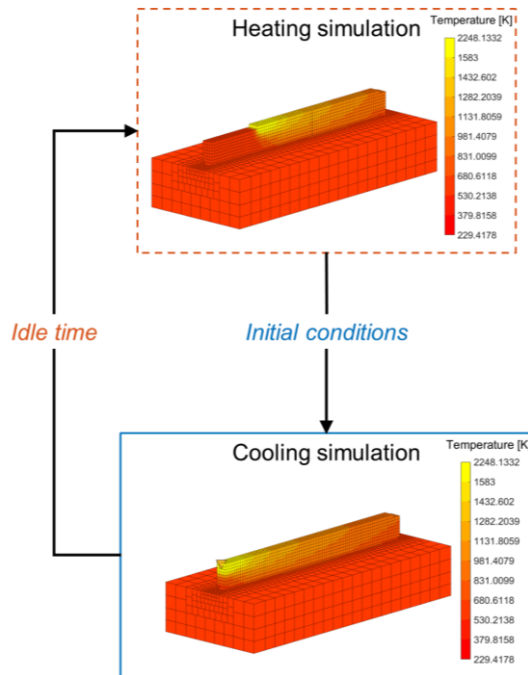


Figure 5.14: FE simulation strategy used for the idle times calculation

The manufacturing of the workpiece is simulated using twin models, one for the heating (deposition) and one for the cooling simulation. The two models are identical in terms of mesh topology, material properties and boundary conditions. The only difference is the presence of the heat source, which is used only in the heating model. In the heating step, the deposition of the current layer is simulated without any idle time at the end of. The end state of this simulation is used to define the initial conditions for the cooling step, i.e. the initial temperature field and the active/quiet state of the elements. The initial elements activation state is prescribed by the initial value of the $\gamma(T_{max})$ variable (defined in section 4.3). The cooling simulation is then started, reproducing the thermal behavior of the workpiece during the idle time at the end of the current layer deposition. To ensure that the control node of the current layer reaches the required interpass temperature, the cooling behavior shall be simulated for a longer time that the expected idles. This is achieved by tuning the total simulation time for the specific workpiece and process parameters. It must be pointed out that this is not a time-consuming approach, due to the large time step that can be used in the cooling phase. The results of the cooling simulation are directly used to calculate the idle time for the current layer, providing the input for the heating simulation of the subsequent layer. This is achieved by including an initial idle time in the heating simulation of the generic layer k , corresponding to the value calculated for the layer $k - 1$. This strategy allows to take the effect of the former idle times into account.

The proposed calculation technique is implemented combining a MATLAB code to start the FE simulations, update the models and to calculate the idle times. The FE simulation are performed in LS-DYNA but any commercial FE code suitable to deal with non-linear heat transfer analyses could be used in its place.

Proposed technique: idle time calculation.

The idle time calculation procedure is outlined in Figure 5.15.

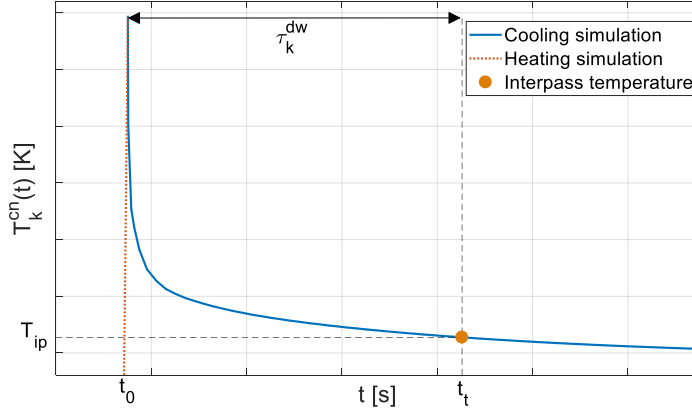


Figure 5.15: Idle times calculation procedure.

Let T_k^{cn} be the time history of the control node temperature returned by the FE solver during the cooling simulation of the k -th layer. This data can be expressed as a continuous function of the simulation time (t) by using a piecewise linear interpolation. Let T_{ip} be the target interpass temperature. The goal is to identify the target simulation time t_t , which fulfills the following equation:

$$T_k^{cn}(t_t) - T_{ip} = 0 \quad \text{Eq. 44}$$

The Eq. 44 can be solved using numerical techniques. This solution is directly used to calculate the idle time corresponding to the k -th layer, τ_k^{dw} :

$$\tau_k^{dw} = t_t - t_0 \quad \text{Eq. 45}$$

Where the term t_0 corresponds to the initial time value of the k -th layer cooling simulation. Hence, at the end of the calculation, an idle time value is associated to each layer.

Verification of the proposed technique: overview

The effectiveness of the proposed technique is demonstrated through an experiment. The proposed technique was applied on a test case component, identifying the idle times required for the manufacturing process. The manufacturing process was then simulated using the calculated idle times. Simulation data were post processed to evaluate the trend of the molten pool size with the increase of deposited layers, assessing the fulfillment of the activity goal.

The test case was manufactured using the WAAM machine presented in section 3.2. A thermocouple was attached to the substrate of the component, acquiring the temperature

time history of specific point during the process. Such data was compared with the FE simulation one to show the accuracy of the modelling techniques used in this thesis. After its manufacturing, the test case geometry was measured through a CMM (Coordinate Measurement Machine) and compared with the reference geometry, highlighting that no significant collapses occurred using the proposed idle times calculation scheme.

Verification of the proposed technique: test case and experiment description

The selected test case is an airfoil. The part drawing and dimensions are shown in Figure 5.16 (a): the cross section is constant throughout the chordal length and the camber line geometry is defined according to the NACA 9403 designation. The deposition was carried out using a 0.8 mm wire made of ER70S-6, a standard filler material used for carbon steel welding. The airfoil was deposited on a block made of S235JR structural steel with low carbon content. The manufactured test case is shown in n Figure 5.16 (b).

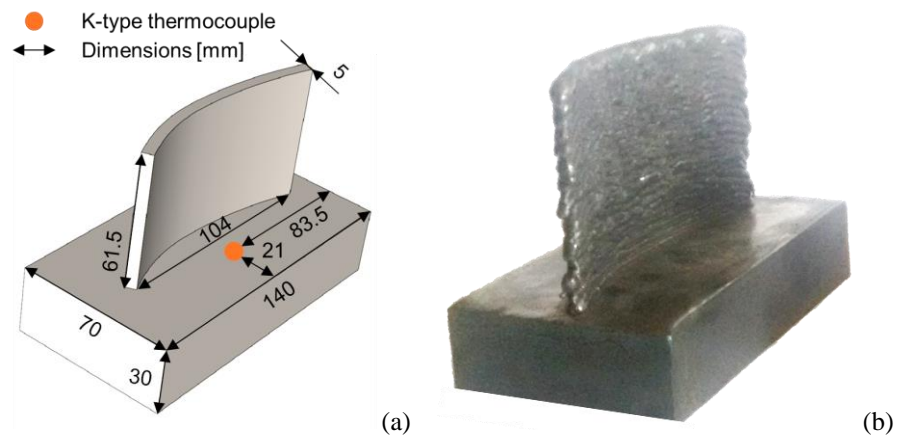


Figure 5.16: The airfoil used as test case: dimensions and thermocouple arrangement (a); actual manufactured part (b)

The WAAM process was carried out using a commercial GMAW machine (AWELCO 250 PULSEMIG). The process parameters used during the deposition are listed in Table 5.2.

Table 5.2: Process parameters used for the test case manufacturing.

Process parameters	
Average welding voltage	18 [V]
Average welding current	80 [A]
Electrical power	1440 [W]
Wire feed speed	4.6 [m/min]
Travelling speed	300 [mm/min]

The presented process parameters resulted in an average layer height of 1.5 mm and an average layer width of 5.0 mm, requiring 41 layers to create the presented geometry. No preheat was applied to the substrate, starting the deposition at room temperature. A k-type

thermocouple was used to measure the substrate temperature during the manufacturing process. The sensor was attached to the top surface of the substrate, positioning it according to the Figure 5.16 (a). The thermocouple signal was logged using a National Instrument 9213 acquisition system, using a sample rate of 10 Hz. After the deposition process the workpiece geometry was scanned using a Mitutoyo Euro Apex C776 CMM to acquire its geometry.

Verification of the proposed technique: FE modelling and idle times calculation

The FE model of the test case is shown was created using 24543 hexahedral elements with a single integration point. The resulting FE model is shown in Figure 5.17.

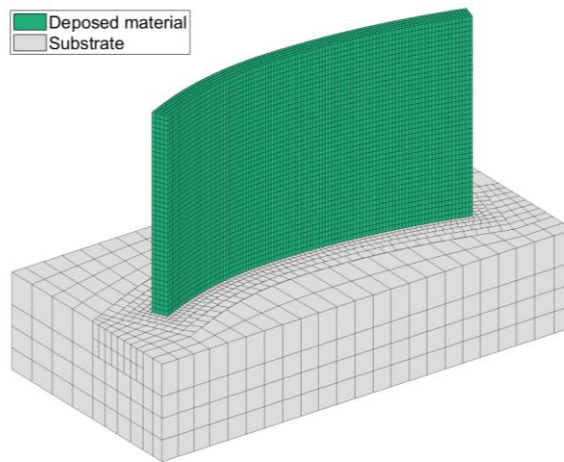


Figure 5.17: FE model of the test case.

The FE calculation was carried out using the techniques and the temperature dependent material properties depicted in section 4.3. The variable time-stepping was adjusted to allow a maximum temperature variation of 400 K per step [123]. For what concerns the boundary conditions, both free convection and radiation were included in the FE model. The convective coefficients were calculated via non-dimensional correlations commonly used in heat transfer literature [117]: 9.94 W/m²K on the substrate vertical surfaces, 10.44 W/m²K on the substrate top surface, 5.22 W/m²K on the substrate bottom surface and 7.8 W/m²K on the airfoil vertical surfaces. The far field temperature was set to 294 K, equal to the room temperature. For the radiation condition the emissivity was set to 0.4, according to literature data [132].

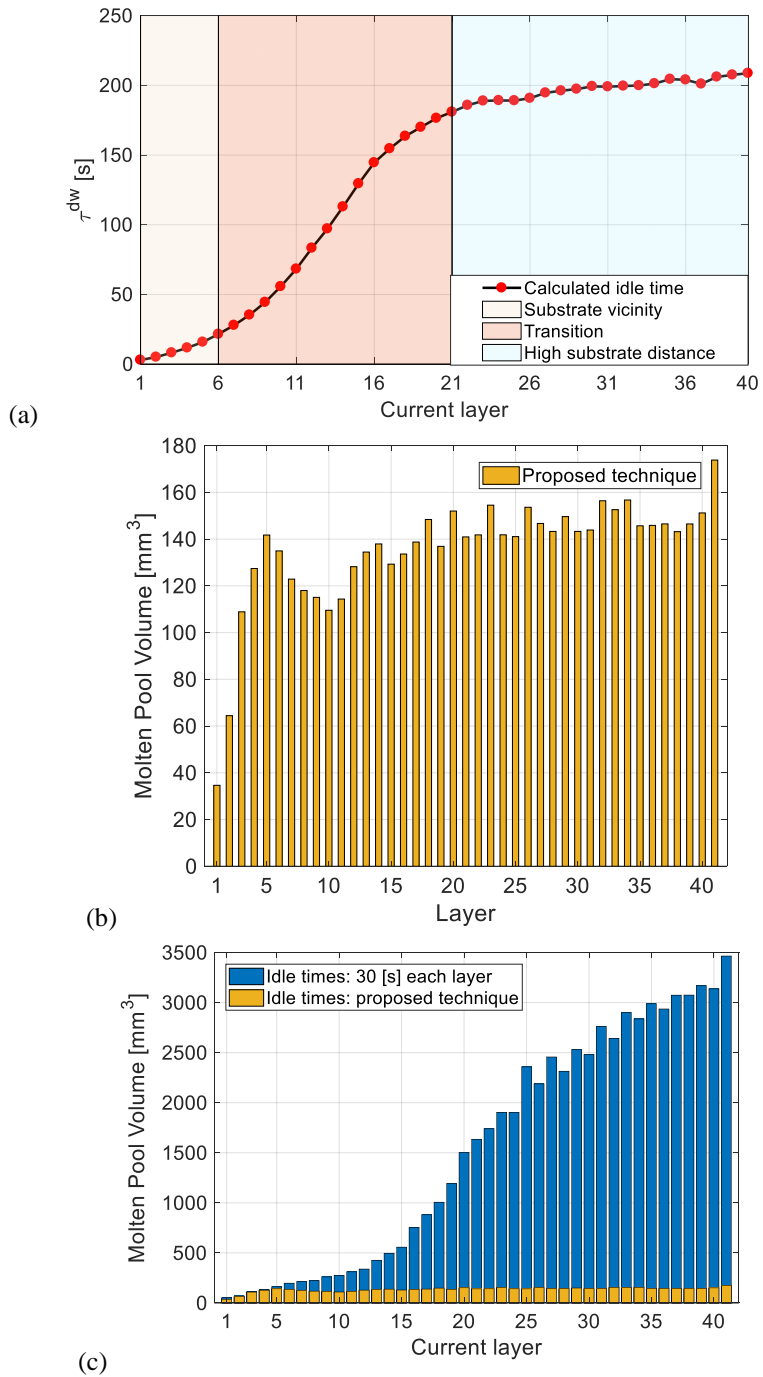


Figure 5.18: Results of the idle time calculation procedure: idle times values (a) and molten pool volume for each layer.

The FE model of the test case was first used to calculate the interlayer idle times, prescribing a constant interpass temperature of 600 K. The result of this calculation is shown in Figure 5.18 a, where the idle times are presented as a function of the current layer index. As expected, the proposed technique prescribes a significant increase of the idle time to achieve a constant interpass temperature on the top of the current layer, thus compensating the reduction of the conductive heat flux in the substrate direction. Besides, the idle time increase is not constant with the workpiece growth. The curve shows a sigmoidal trend with three distinct regions (Figure 5.18 (a)) having different rate of idle time increase. Such pattern can be motivated considering the distance between the substrate and the molten pool. The vicinity region corresponds to the first layers, with the substrate close to the molten pool. This creates a heat sink effect leading to a quick cooling. Hence the growth of the workpiece has a marginal effect on the conductive heat flux, resulting in the small variations of the idle time. On the opposite, the high substrate distance region corresponds to the last layers, where the heat sink effect of the substrate is significantly reduced. In this condition, the cooling problem approaches the one-dimensional behavior, where the magnitude of the conductive heat flux is roughly proportional to the overall workpiece height. Hence, due to the low value of the layer high with respect to the workpiece one, the convective heat flux experiences a slight reduction for any additional layer, resulting in a slight increase of the idle times. According with these considerations, the central part of the curve has been labeled as a transition region, in which the heat sink effect of the substrate reduces its influence on the cooling behavior. This results in a high increase of the idle times. It must be pointed out that the extensions of the three regions are expected to be dependent on the prescribed interpass temperature, on the process parameters and on the workpiece geometry.

After the calculation of the idle times, the manufacturing of the test case was simulated to evaluate the effect of the proposed technique on the molten pool size, quantified as the volume of the elements above the solidus temperature, namely with liquid phase fraction greater than zero. The calculation was repeated for each time state of the simulation results, extracting an average value for each layer. Figure 5.18 (b) shows the result of this calculation. It is highlighted that the molten pool size is almost constant throughout all the layers. Indeed, except for the initial 6 layers, the maximum variation of the molten pool volume is below the 15%. The initial steep growth of the molten pool is related both to the absence of preheating and to the heat sink effect of the substrate. This is consistent with the trend of Figure 5.18 (a), which shows that the upper bound of the substrate vicinity region is located in correspondence of the 6th layer. It is expected that pre-heating the workpiece would result in a slighter variation of the molten pool volume in the initial layers.

To compare the results of the proposed technique with a random selection of the idle times, the simulation was repeated using a constant idle time value of 30 s after each layer. Figure 5.18 (c) compares the molten pool volume calculated with the proposed idle times and with constant value. In this case, the usage of a constant idle time leads to a constant increase of the molten pool size per each additional layer. On the opposite, the proposed technique allows to keep the molten pool size almost constant throughout the whole process.

This comparison highlights that, in free convection conditions, it is important to adopt a structured procedure to determine the idle times. The proposed technique fairly serves this purpose, eliminating the need to perform time consuming trial and error procedures.

Verification of the proposed technique: results of the experiments

This section presents and discusses the results of both thermocouple and CMM measurements.

The goal of the thermocouple measurement was to highlight the accuracy of the FE simulation technique. Figure 5.19 shows the comparison of the thermocouple data with the temperature time history of a node located in the same position. The data is shown from the 18th layer to the end of the process

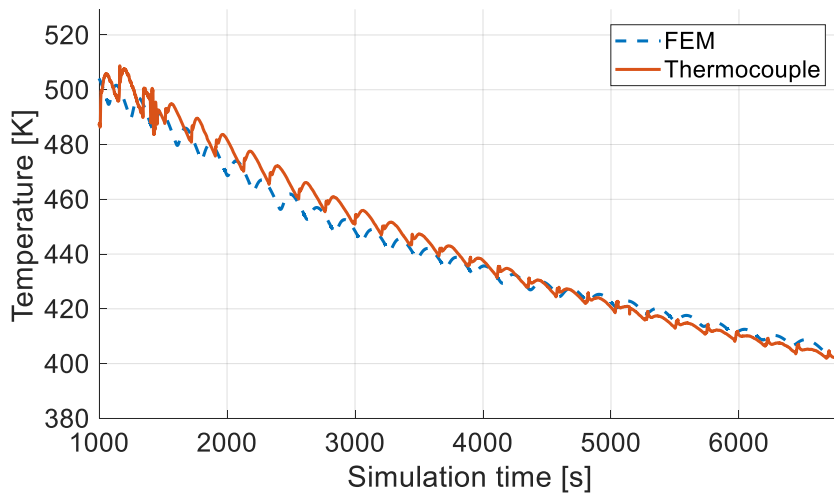


Figure 5.19: Comparison of simulation and thermocouple data.

This comparison highlights that the simulation data are in good agreement with the measured ones, both for what concerns the overall trend and the punctual values. This is a relevant result since the proposed idle times calculation is effective only if the FE model is accurate in predicting the workpiece temperature field, otherwise the interpass temperature constraint might not be fulfilled in the actual process. Moreover, this result supports the reliability of the molten pool size pattern shown in Figure 5.18 (b), yield from simulation data.

The goal of the CMM measurement was to show that the proposed technique allowed to avoid major part collapses without performing trial and error operations to select the idle times. The functional surfaces of the airfoil, namely the pressure and the suction side, were scanned by the CMM and compared with the target surfaces, as shown in Figure 5.20.

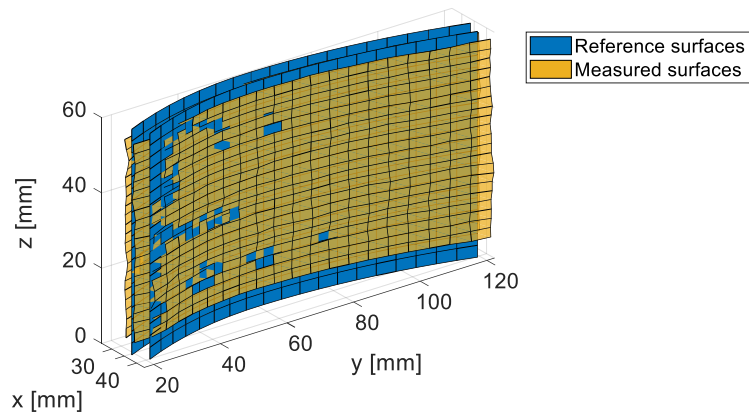


Figure 5.20: Comparison of the measured blade surface and the reference CAD model.

The average deviation from the target surface was 0.65 mm for the pressure side and 0.39 mm for the suction side. It must be pointed out that the measured surfaces were affected by a significant waviness (Figure 5.16 (b)) typical of the WAAM processes. Hence this result confirms that no significant collapse phenomenon occurred during the deposition process.

As a conclusion, it is important to remark that despite the effectiveness of the proposed technique an excessive interpass temperature could still cause the workpiece collapse. For this reason it is important to refer to literature works recommending interpass temperature values for various materials.

5.4. Conclusions and remarks

This thesis shows that the WAAM macro scale simulation can be an effective tool to address the heat accumulation. The state of the art highlighted that two main techniques can be pursued to prevent the heat accumulation in WAAM: increase the heat transfer rate from the workpiece to the environment or introduce idle times between the layers. This thesis used the process simulation to pursue both these paths, proposing the usage of an alternative cooling system to increase the heat transfer rate and developing an algorithm to schedule the interlayer idle times. Table 5.3 summarizes the contributions to the state of the art proposed in this chapter.

The process simulation was used to assess the effectiveness of the jet impingement cooling applied to the WAAM process. This allowed to test the performances of such cooling system in a virtual environment, enabling a detailed evaluation of the temperature field, hardly practicable by an empirical approach. Besides the developed jet modeling technique enables to optimize the cooling system parameters, tailoring it for different materials and applications.

The idle times scheduling technique is entirely based on the process simulation. This allows to determine the interpass temperature on the top layer, resulting in an almost constant molten pool size over the workpiece height. Moreover, the effect of different interpass temperature on the thermal and mechanical behavior could be investigated without the need to perform a large number of experiments.

Hence the process simulation was proven to be effective tool in tackling the heat accumulation issue, in accordance with previous researches which used it to tackle different process criticalities such as the residual stresses and deformations.

Table 5.3: Summary of the thesis contributions to the heat accumulation SoA.

Heat accumulation
Increase heat transfer rate: <i>Thesis contribution</i>
Jet impingement application to WAAM process [3]:
Increase of the heat transfer rate, constant molten pool size.
Idle times: <i>Thesis contribution</i>
Adaptive idle times scheduling based on FE simulation:
Constant molten pool size and interpass temperature.

6. Milling of WAAM parts

The chapters 4 and 5 are dedicated to the AM part of the hybrid WAAM-milling process, proposing improvements to the current simulation techniques and an actual application of the WAAM modelling. However, to make the hybrid approach effective, both WAAM and milling processes must be considered. This chapter is focused on the issues that related to machining operations of WAAM components. This thesis considers milling as post-process machining technology.

Post process milling of WAAM parts can be a challenging task since it requires to deal with two issues:

- Machinability of the WAAM processed material: as extensively discussed, during WAAM the material undergoes thermal transformations affecting its microstructures and its mechanical properties. This might result in a different machinability of the WAAM processed material, with respect to the cast or wrought one. This requires a preliminary analysis of the machinability of the WAAM material to select suitable cutting parameters.
- Milling of thin-walled parts: from an economic point of view, the WAAM process is convenient for thin-walled components rather than bulk ones. Making thin walled parts by milling requires to remove a large amount of the feedstock volume, a time-consuming process involving a large waste of material. The hybrid WAAM-milling process reduces the feedstock material to be removed, being a convenient alternative for the thin walled components. However, milling operations of this kind of workpieces is a critical task, since thin-walled components are prone to vibration issues. This could result in a significant reduction of the accuracy and surface finish.

This thesis addresses both of the presented issues.

For what concerns the machinability of the WAAM processed material, this thesis presents a machinability analysis of AISI H13 tool steel, focused on the cutting forces. The purpose of this work is to compare the cutting forces magnitude of the AM processes material with the wrought one.

To address the issues related to the milling of thin walled components, this thesis proposes an FEM based technique to identify the changing workpiece dynamics. Indeed, the knowledge of the system dynamic behavior is a crucial information to predict and prevent the occurrence of vibration issues in milling. This can be a challenging task when dealing with thin walled components since the dynamic response of the workpiece changes during

the machining cycle. Based on the toolpath and on the stock geometry, the proposed algorithm calculates the driving point FRF (Frequency Response Function) at the contact point between tool and workpiece. The knowledge of the changing workpiece dynamics is used to carry out an optimization of the spindle speed parameter.

The contents of this chapter are structured as follows:

6.1 Machinability of WAAM processed material: this section presents the state of the art regarding the machinability of metal AM parts, highlighting the novelty of the proposed contributions. The experimental activity is then described, depicting the adopted procedures and the performed machinability tests. The results are finally presented and discussed.

6.2 Machining of thin-walled components: first this section provides an introduction to the issues concerning the machining of thin walled components, detailing the state of the art solutions used to tackle such issue.

6.3 Conclusions and remarks: this section summarizes the thesis contributions to the state of the art and provides some final remarks.

6.1. Machinability of WAAM processed material

WAAM, and in general DED components, require post-process machining operations to achieve the functional requirements in terms of dimensional accuracy and surface finish. Therefore, assessing the machinability of AM materials is a crucial topic. Since there is not a unique indicator to define the machinability of a material [165], the following three aspects are usually considered: tool life, surface integrity and cutting forces [166]. In literature few works deal with AM materials machinability: Bordin et al. [167] compared tool life and surface integrity in turning wrought and Electron-Beam-Melting (EBM) CrCoMo alloy, highlighting an increase of tool wear and the arise of surface craters in the AM material. In a subsequent work, Bordin et al [168] compared the dry and cryogenic cutting strategies in turning operation of Ti6AlV4 alloy, analyzing the wear mechanisms, the tool life and the surface integrity.

The presented state of the art works investigated machinability of AM material for what concerns tool life and surface integrity aspects. However, no analysis of the cutting forces was carried out. This is a relevant parameter in evaluating material machinability, especially in milling operations: higher specific cutting forces (i.e., cutting coefficients) can reduce the stability limit [169] and increase the amplitude of vibrations [170] especially when using flexible tooling or milling thin-walled parts [171].

In this thesis, the machinability of AM and wrought material is compared analyzing cutting forces in peripheral milling operations. The analysis was carried out for two different DED technologies: the LENS and the WAAM process. LENS is a DMLD process using powder feedstock, in opposition to WAAM which is wire based.

The analyzed material was the AISI H13, a low alloy steel usually adopted in dies and molds manufacturing, that is one of the main application of AM technologies both for manufacturing and repair operations [16].

Milling tests were carried out on wrought, LENS and WAAM specimens. The cutting forces were measured using a table dynamometer. Measured cutting forces were used to

compute cutting force coefficients as defined in Altintas et al. [172] mechanistic cutting force model. This step provided an indicator of cutting forces independent from the adopted cutting parameters.

Cutting force analysis: overview

The objective of this work is to provide a comparison between cutting forces in milling AM and wrought AISI H13 steel. This short paragraph gives an overview of the procedure followed in the analysis.

Before carrying out the milling tests, the hardness of the specimens was measured to acquire preliminary information about the material. After this pre-test step, the cutting parameters were selected according to the recommendations of the tool manufacturer. Finally, cutting tests were carried out measuring cutting forces. Cutting coefficients were then identified according to the mechanistic technique.

Cutting force analysis: experimental set up

The LENS specimen was manufactured using an OPTOMECH 850 R machine thanks to the support of the company EMO Orodjarna. The WAAM specimen was manufactured in Tokyo University of Agriculture and Technology (TUAT) using a Daihen gas metal arc welding unit attached to a tailor-made four axis machine tool. AM and wrought specimens are shown in Figure 6.1. The cutting tests on wrought and LENS samples were carried out using a DMG Mori NMV1500DCG vertical milling center in the University of Firenze laboratory. WAAM specimen was machined using a MAZAK VCN-410A vertical milling center in the TUAT. For both machines, cutting forces were used using a Kistler 9257 B three axial table dynamometer.



Figure 6.1: Wrought (a), WAAM (b) and LENS (c) material specimens

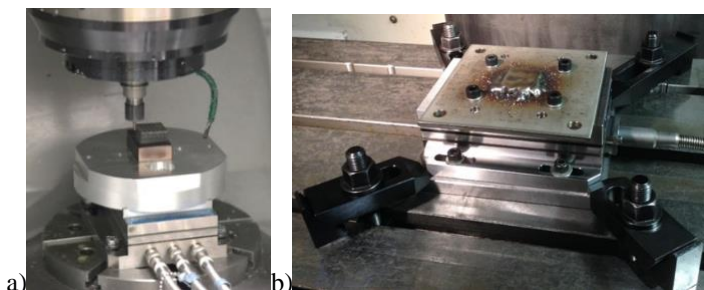


Figure 6.2: LENS (a) and WAAM (b) specimen test set-up.

Cutting tests were carried out using a 4mm diameter Taegutech (HSF 2040 060 100) solid carbide end mill (sharp edge). The selected end mill is suitable for finishing operations

on pre-hardened and hardened steel. Furthermore, tool has sharp edge, simplifying the cutting coefficients identification procedure [169]. Cutting tool and machines set-up conditions are shown in Figure 6.2.

Cutting force analysis: preliminary hardness tests

As mentioned earlier, before carrying out the cutting tests material hardness was measured for all the specimens. Rockwell testing (Type C) was selected. The results are presented in Table 6.1.

Table 6.1: Rockwell C hardness measuring results.

Hardness: HRC		
<i>Wrought</i>	<i>LENS</i>	<i>WAAM</i>
19	59	55

The hardness tests highlight that both the AM materials experience a significant increase in hardness. This increase of hardness is compliant with the martensitic transformation occurring in both welding and DMLD of AISI H13 [173]. Based on such results, an increase of cutting forces is expected on the wrought material with respect to the wrought one.

Cutting force analysis: cutting force coefficients identification procedure

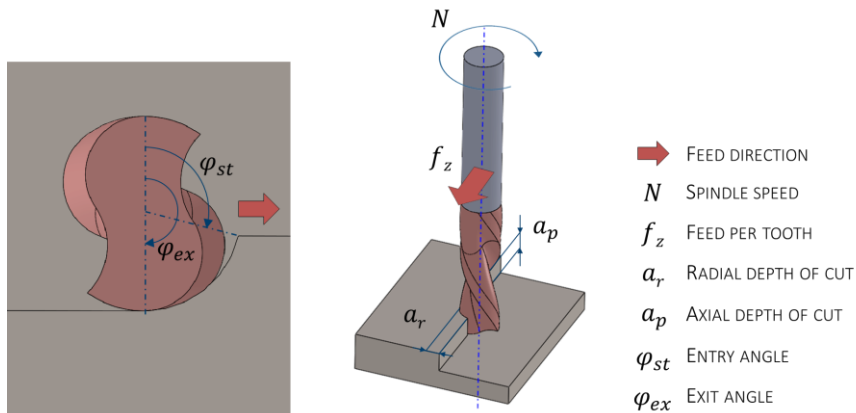


Figure 6.3: Cutting parameters in a peripheral milling operation.

The cutting force model proposed in [172] was used to evaluate the cutting force coefficients. This model computes the force components (tangential, radial and axial) by means of six coefficients as expressed in Eq. 46, where db is chip width, dl is the engaged cutting-edge length and t_n the chip thickness for an infinitesimal section of the chip.

$$\begin{aligned}
 dF_i &= K_{tc}t_n db + K_{te} dl \\
 dF_r &= K_{rc}t_n db + K_{re} dl \\
 dF_a &= K_{ac}t_n db + K_{ae} dl
 \end{aligned}
 \tag{Eq. 46}$$

K_{tc} , K_{rc} and K_{ac} are the shear coefficients, relating the cutting force with the uncut chip section, namely the $t_n db$ product. K_{te} , K_{re} and K_{ae} are the edge coefficients, relating the cutting force to the length of the cutter edge engaging the workpiece. The chip thickness and width are dependent on the depths of cut (both radial and axial) and on the feed per tooth.

Figure 6.3 depicts the aforementioned cutting parameters, represented on a typical peripheral milling application: f_z is the feed per tooth; a_p and a_r are the axial and radial depth of cut respectively; N is the spindle speed; φ_{st} and φ_{ex} are the entry and exit angles, which value can be calculated by Eq. 48

$$\begin{cases}
 \varphi_{st} = \pi - \arccos\left(1 - \frac{2a_r}{D}\right) \\
 \varphi_{ex} = \pi
 \end{cases}
 \tag{Eq. 47}$$

According to their definition, the cutting force coefficients can be regarded as an indicator of the material machinability from a cutting force perspective. Since these parameters are independent on the material removal rate, they are related only to the tool and workpiece material, serving as an indicator of the specific cutting force.

This work compares the machinability of wrought and AM AISI H13 using the radial and tangential cutting coefficients. The axial coefficients are not included in the analysis, since the tangential and radial ones are the most significant for tool vibration in peripheral milling [174].

The cutting force coefficients were computed according to the mechanistic identification procedure in [169]. In such a technique, a series of peripheral milling tests must be carried out at different feed per tooth but with fixed depth of cut, radial engagement and cutting speed. The cutting forces are measured in X, Y and Z directions: X is the feed direction, Z is the spindle axis direction and Y is the normal direction according to the right-hand rule. The force time series are then post-processed to identify average forces per cutter revolution. Since the cutting force in milling is periodic, the average force per cutter revolution is equivalent to the average cutting force during the whole cutting test. Figure 6.4 (a) shows the time history of a generic component of the cutting force (i). The figure compares average and instantaneous values: F_i is the instantaneous force signal while \underline{F}_i is the average force value.

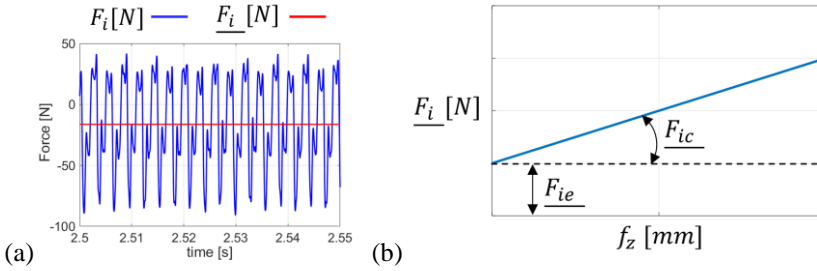


Figure 6.4: Average force per tooth revolution (a); linear relation between average force and feed per tooth (b).

According to the cutting force model described in Eq. 46, a linear relation exists between average cutting forces and feed per tooth, as shown by Eq. 48:

$$\underline{F}_i(f_z) = \underline{F}_{ie} + \underline{F}_{ic} f_z \quad \text{Eq. 48}$$

Where $\underline{F}_i(f_z)$ is the generic average force expressed as a function of the feed per tooth; \underline{F}_{ie} and \underline{F}_{ic} are the zeroth and first order coefficients respectively. The values of such coefficients can be calculated by performing a linear regression, of the measured average forces. Then \underline{F}_{ie} is related to the edge coefficients according to the following relation:

$$\frac{N_z a_p}{2\pi} \begin{vmatrix} \sin \varphi_{st} - \sin \varphi_{ex} & \cos \varphi_{ex} - \cos \varphi_{st} \\ \cos \varphi_{st} - \cos \varphi_{ex} & \sin \varphi_{st} - \sin \varphi_{ex} \end{vmatrix} \begin{vmatrix} K_{te} \\ K_{re} \end{vmatrix} = \begin{vmatrix} \underline{F}_{xe} \\ \underline{F}_{ye} \end{vmatrix} \quad \text{Eq. 49}$$

In the same way, the shear coefficients can be calculated by solving Eq. 50:

$$\frac{N_z a_p}{8\pi} \begin{vmatrix} \cos 2\varphi_{ex} - \cos 2\varphi_{st} & 2(\varphi_{ex} - \varphi_{st}) - (\sin 2\varphi_{st} - \sin 2\varphi_{ex}) \\ 2(\varphi_{ex} - \varphi_{st}) - (\sin 2\varphi_{st} - \sin 2\varphi_{ex}) & \cos 2\varphi_{ex} - \cos 2\varphi_{st} \end{vmatrix} \begin{vmatrix} K_{tc} \\ K_{rc} \end{vmatrix} = \begin{vmatrix} \underline{F}_{xc} \\ \underline{F}_{yc} \end{vmatrix} \quad \text{Eq. 50}$$

Therefore, solving the linear systems presented in Eq. 49 and in Eq. 50 returns the values of the cutting force coefficients. One of the mechanistic procedure is the usage of the average rather than instantaneous ones, since this value is not affected by measurement errors induced by vibrations [175].

To pursue the presented identification procedure, six different feed per tooth values were used for the cutting tests. Table 6.2 presents the cutting parameters used in the tests.

Table 6.2: Tests cutting parameters

Feed per tooth [mm]					
0.05	0.07	0.09	0.11	0.13	0.15
Radial depth of cut [mm]			0.8		
Axial depth of cut [mm]			0.5		
Cutting velocity [m/min]			120		

Usually such tests are performed in slotting conditions, namely with radial depth of cut equal to the tool diameter. The reason is that this cutting condition simplifies the identification of cutting coefficients from linear regression data. Preliminary slotting tests were carried out to assess the feasibility of such approach on AM materials. Even though the wrought material could be easily milled in this condition, remarkable effects of high cutting temperature were observed on the AM material, as shown in Figure 6.5. This caused detrimental effects both on surface quality and on tool integrity. This aspect is particularly relevant to identify reliable cutting coefficients values: since such parameters are dependent on tool rake angles, an excessive tool wear could affect the identification procedure. After the pre-test, a side milling condition was chosen over the slotting one, adopting the radial engagement recommended by tool manufacturer, presented in Table 6.2.

All tests were carried out in down milling condition without any type of coolant or lubrication.

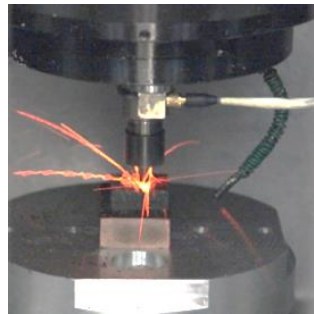


Figure 6.5: Hot chip during LENS specimen slot milling.

Cutting force analysis: results and discussion

This paragraph presents the outcome of the cutting tests. Two main results are given: average cutting forces and cutting force coefficients. To improve the robustness of the input data for cutting coefficient identification, all cutting tests were repeated twice. The average force values extracted from the tests at the same feed per tooth were then averaged, reducing the effect of casual errors, such as measurement noise. Therefore, average forces presented in this section are not related to a single test but are averaged as described above.

Average forces are given in the feed and in the normal direction: Figure 6.6 (a) and Figure 6.6 (b) show the comparison between average values of AM and wrought cutting forces (on both directions). Despite cutting tests were carried out for six different feed per tooth values, just the three lower values are presented. This was due to an issue concerning cutting tests on WAAM material: average forces concerning higher feed experienced a significant deviation from the regression line. On larger feed per tooth value on WAAM material, remarkable tool vibrations were observed and the finished. This was compliant with a bad surface finish. Therefore, for wrought and LENS material the data from six tests were used to carry out cutting coefficients computation, while for WAAM material just the three values were used.

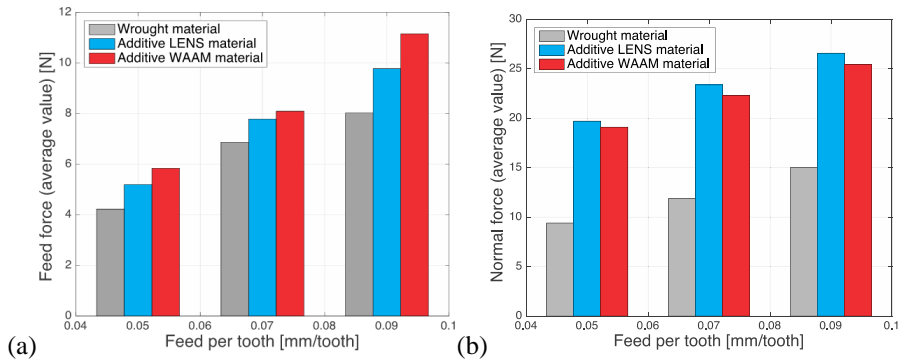


Figure 6.6: Comparison of average values of feed (a) and normal (b) forces.

The results concerning cutting coefficients are presented in Table 6.3: the values of the radial and tangential constants are compared between the three different specimens.

Table 6.3: Cutting coefficients identification results.

	Cutting force results			
	K_{tc} [MPa]	K_{rc} [MPa]	K_{te} [MPa]	K_{re} [MPa]
<i>Wrought</i>	2424	808	8	20
<i>LENS</i>	2721	1077	42	76
<i>WAAM</i>	2848	1007	40	71

As expected from hardness testing, cutting force values are significantly higher in LENS material. Both average forces and cutting coefficients values confirm this pattern. As shown in Table 6.3, the LENS material tangential cutting coefficient is about 10% higher than the wrought material one. Such difference increases to 30% for the radial cutting coefficient.

Cutting forces and coefficients observed on WAAM material are compliant with the LENS ones. A general increase of both average cutting forces and cutting coefficients was observed. As shown in Table 6.3, tangential cutting coefficients turned out to be higher on WAAM material than in the LENS one. On the other hand, the trend is opposite for the radial coefficient, higher on the LENS material.

In summary, this analysis highlights that additive manufactured AISI H13 is harder to machine compared to the wrought one. The results show a significant increase of both average cutting forces and cutting force coefficients. According to literature and hardness measurements, this increase in cutting force coefficients could be related to the formation of a martensitic microstructure, due to the quick cooling occurring in both LENS and WAAM process. Hence a specific definition of cutting parameters for milling operation of AM parts is required to effectively machine this material processed by AM technologies. Moreover, this result suggests that, in general, machining of metal AM parts should be regarded as critical operation, requiring a careful definition of the cutting parameters.

6.2. Machining of thin-walled components

One of the main application of the metal hybrid processes is the manufacturing of thin walled components. The number of such parts is increasing in many industries (e.g. power generation, aerospace, automotive) to cope with the growing need of weight reduction. Due to the strict strength and fatigue requirements, such structures are often machined from the bulk as monolithic components, removing a large amount of material to create the final product. Usually this is achieved throughout intensive milling operations, removing up to 95% of the stock volume, to create the final geometry [176]. For this reason, hybrid processes represent a convenient alternative, enabling a dramatic reduction of the wasted material [17]. AM acts as primary process, creating a part which geometry is close to the one of the final component. The final shape of the component is then achieved by milling the AM stock. However, milling thin walled parts is a critical operation due to the low stiffness of such workpieces, making them prone to forced vibrations, chatter (self-excited vibration [177]) and deflection issues, being responsible for surface location errors and poor finish [178]. It must be pointed out that this issue is not only related to the hybrid WAAM-milling process but it affects every hybrid AM-machining technique.

The general approach used by the industry to prevent these issues is to limit the Material Removal Rate (MRR) by means of conservative machining parameters. This generates a reduction of the cutting forces which limit the workpieces vibrations at the expense of a reduced productivity. Therefore, several researchers worked on this issue to develop strategies mitigating the workpiece vibrations without affecting the productivity. Thevenot et al. [179] investigated the vibration phenomena occurring in thin walled components. The authors highlighted that the driving point FRFs (Frequency Response Functions), namely the combined tool-workpiece FRFs at the cutting point, change during the machining process due to the material removal. Moreover, in a thin walled workpiece, the driving points FRFs are strongly dependent on the excitation point, resulting in a different dynamic behavior over the component. Therefore, the knowledge of the changing workpiece FRFs is mandatory to define optimized cutting parameters.

The most effective approach to mitigate the workpiece vibrations is to modify the spindle speed. Indeed, such parameter is selected independently by the toolpath. Moreover, it has a direct influence on the frequency content of the cutting forces. Bolsunovskiy et al. [180] used a 3D FE model to predict the changing FRFs of a thin walled workpiece. This information was used to counteract the forced vibrations, by defining a changing spindle speed with the objective of avoiding the excitation of the workpiece resonance frequencies by the tooth pass frequency harmonics. Seguy et al. [181] used a similar approach finalized to avoid the occurrence of chatter vibrations rather than forced ones. This led to the definition of a variable spindle speed but with a different pattern. Tuysuz and Altintas [182] proposed a sub structuring approach to calculate the workpiece FRFs. Based on FE modelling, this technique enables to reduce the computational effort required to calculate the workpiece FRFs. Arnaud et al. [183] combined a 3D FE model of the workpiece with a cutting force model, aiming at an accurate prediction of both cutting forces and machined part geometry.

Table 6.4 summarizes the state of the art approaches to deal with milling of thin walled parts

This thesis proposes an innovative approach to identify the dynamic behavior of thin walled workpieces during milling operations. The basis of the proposed technique is the identification of the workpiece dynamics through FE modelling using 2D shell elements.

This approach enables an efficient and accurate description of thin walled structures dynamics [140]. Moreover, the generation of a shell model could be easily automated exploiting AM deposition path, since it provides the information concerning the workpiece skeleton surface.

The proposed technique is divided in three main stages: AM stock modelling, stock thickness updating and FRFs identification. In the first step a shell FE model of the deposited material is created. The milling G-code is then analyzed by an automated algorithm that identifies the position of tool-workpiece contact point and updates the stock geometry by thickness property of the shell elements. This information is used to generate an updated FE model of the workpiece which takes the material removal effect into account, giving an accurate description of its changing dynamic behavior. In the final step, the workpiece FRFs are calculated at the driving points (i.e. the tool-workpiece contact point) for every step of the machining process. This provides all the required information to optimize the milling process.

The accuracy and effectiveness of this technique was verified by means of a test case. Three specimens of a specific thin walled component were manufactured by means of the WAAM machine presented in section 3.2. A 5-axis milling cycle was then defined and analyzed using the proposed technique, identifying the evolution of workpiece dynamics. The machining parameters, namely the spindle speed and the feed rate, were subsequently adjusted following three different optimization techniques. The specimens were machined, interrupting the process to carry out impact testing experiments, required to verify the accuracy of proposed modelling technique. At the end of the milling process, the specimens were analyzed through CMM measurements, to assess the surface location error.

The contents of this section are arranged as follows: first the details of the test case geometry and manufacturing are provided; then the proposed FRFs calculation technique is described; the applied optimization techniques are then presented; finally, the results of the machining tests are presented and discussed.

Table 6.4: Summary of the state of the art works related to milling of thin walled parts.

Milling of thin walled parts	
Thevenot et al. [179]	Investigates the effect of changing dynamic on workpiece vibrations
Bolsunovskiy et al. [180]	Model based spindle speed selection to avoid forced vibrations
Seguy et al. [181]	Model based spindle speed selection to avoid forced vibrations
Tuysuz and Altintas [182]	Sub structuring based technique to reduce the FRFs calculation time
Arnaud et al. [183]	3D FE model of the workpiece combined with a cutting force model

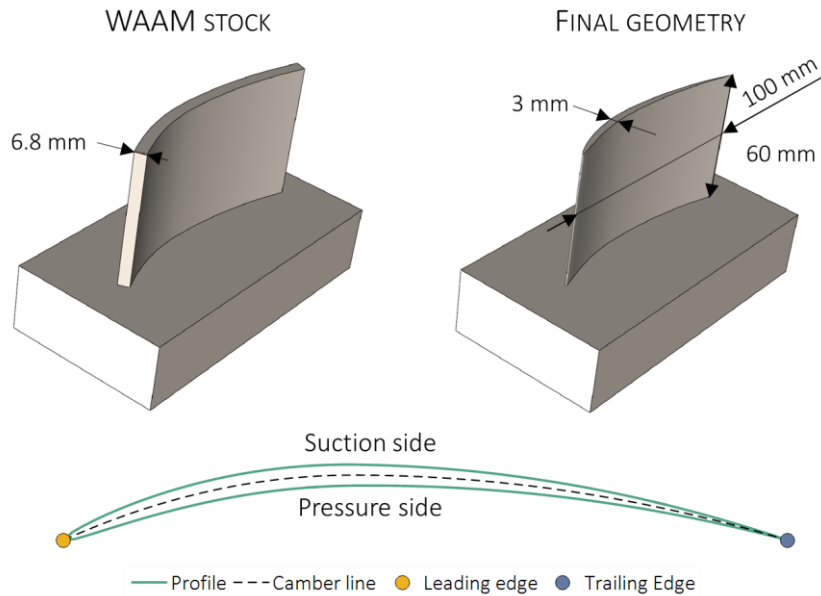
Description of the test case

Figure 6.7: Geometry of the test case selected for the verification of the proposed technique.

The test case selected to test the proposed technique is the NACA 9403 airfoil presented in section 5.3. Figure 6.7 presents the test case geometry after the WAAM deposition and after the finishing operation. The test case has a maximum thickness of 3 mm, making it a representative example of a thin walled component. The WAAM deposition toolpath is defined to create a constant thickness component shaped as the camber line of the airfoil (Figure 6.7). The subsequent milling operation creates the functional surfaces of the airfoil, namely the pressure side and the suction side (Figure 6.7).

The airfoil was deposited by stacking 35 layers of ER70S-6 onto a brick shaped substrate made of S235JR. The deposition was carried out using the process parameters presented in Table 6.5. Such parameters resulted in an average layer height of 1.8 mm and in a layer width of 6.8 mm.

Table 6.5: Process parameters used for the test cases manufacturing.

Process parameters	
Average welding voltage	18 [V]
Average welding current	80 [A]
Wire feed speed	4.6 [m/min]
Travelling speed	200 [mm/min]

These test cases were created by using a lower travelling speed with respect to the one selected for the test case presented in section 5.3. This ensured a wider layer providing the machining allowance required to achieve the final geometry.

The airfoil was machined using a 5-axis cycle to cope with its geometry. The cycle is constituted by three phases: roughing, semi-finishing and finishing. The goal was to optimize the finishing step since it is the one responsible for the accuracy and the surface finish of the final part.

The tool used for all the operations is a 2 flutes 10 mm carbide ball end mill produced by Garant (cod. 207280), designed for dry cutting condition on carbon steel. A morphing strategy was applied for the roughing phase to achieve an offset geometry of the airfoil starting from the nearly constant thickness geometry produced by WAAM process. Figure 6.8 (a) shows a step of the roughing operation.

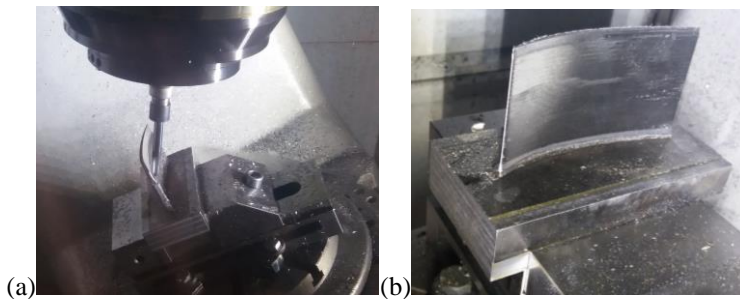


Figure 6.8: a) Roughing cycle, b) finished part

The following machining parameters were selected, based on previous experiences of WAAM parts machining [184]: axial depth of cut 2 mm, cutting speed 180 m/min and feed per tooth 0.062 mm/tooth. A machining allowance of 0.5 mm was left on the product, to be removed in the following steps. RTCP was activated for the G Code set-up and a constant 30° tilt angle of the tool respect to the airfoil surface was used. The geometry of the WAAM stock was acquired by CMM measurement after the deposition. This data was used to optimize the alignment between the final part and the stock. The oriented geometry of the airfoil was then used to create the toolpath by the CAM software ESPRIT®. After the roughing cycle, a semi-finishing and a finishing operation were carried out to complete the manufacturing of the airfoil. The two cycles used the same tilt angle of the roughing phase. The axial depth of cut adopted for the machining operations was 1 mm for semi-finishing and 0.5 mm for finishing. These parameters were selected considering the expected surface finish. Figure 6.8 (b) shows one of the specimens after the finishing step.

Proposed technique

The dynamics of thin walled parts can be effectively estimated by FE models. This thesis proposes to use 3D shell elements to discretize the workpiece. These elements have a twofold advantage: they enable to reduce the calculation time (reduced DOFs number) and they provide a more accurate description of the dynamic behavior of thin walled parts. Moreover, considering the application of proposed technique to WAAM process, the deposition path can be used to automatically generate the shell FE mesh. Each point of the NC code generated to create the deposition toolpath can be used to become a node of the FE model, where only the properties and thickness of the shell elements must be adjusted to achieve a realistic model.

The WAAM stock is initially discretized by shell elements, as shown in Figure 6.9.

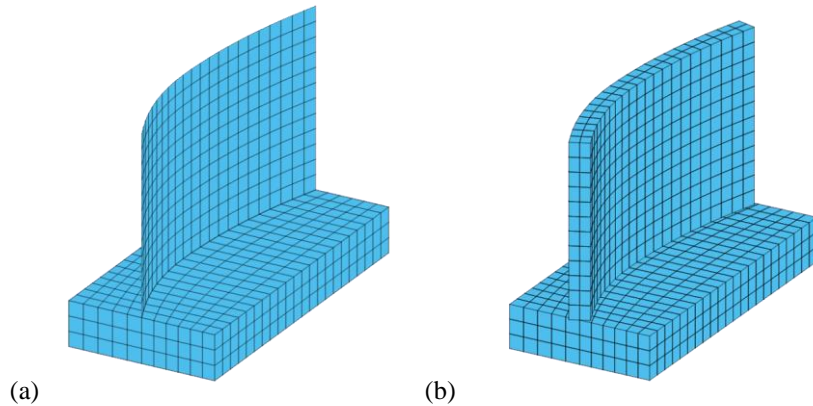


Figure 6.9: Test case discretized by shell elements: traditional (a) and 3D (b) representations.

It must be pointed out that the model shown in Figure 6.9 do not represent the whole test case. The airfoil is modelled by using shell elements, but the substrate is not completely discretized. As shown by Figure 6.8 (a), during the milling process the substrate is clamped inside a vise. Therefore, its contribution to the dynamics of the airfoil is negligible. In this work a reduced portion of the substrate in the vicinity of the airfoil is modelled by solid elements to reproduce the local stiffness effect. The substrate is then blocked by single point constraints.

A correct evaluation of the workpiece changing dynamics requires to take the material removal into account. Hence, the FE model must be continuously updated, according to the tool position along the milling toolpath. For this reason, a general algorithm was developed to modify the nodal thicknesses, according to the tool engagement obtained by a post-processing of the G-code. First, the proposed algorithm associates each node of the FE model to a point of the G-code, based on the minimum distance criterion, as shown in Figure 6.10.

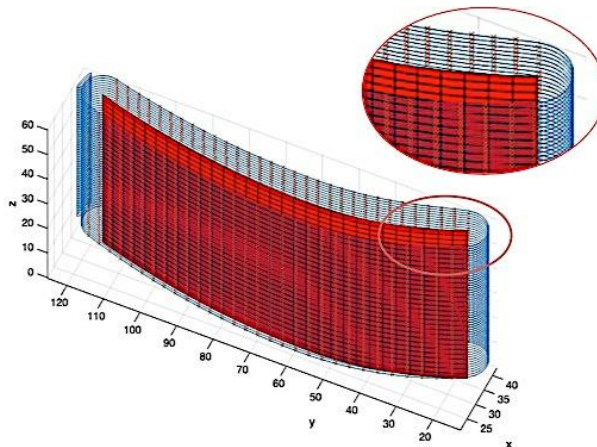


Figure 6.10: Association between FE model nodes and G-code points.

Basically, the toolpath is discretized considering a reduced set of line block, corresponding to the nodes position of the FE model. This enables to use a mesh size coarser than the G-code resolution.

Based on the identified correspondence, the algorithm calculates the engagement by intersecting the geometry of the tool with the one of the machined surface, as shown in Figure 6.11 (a).

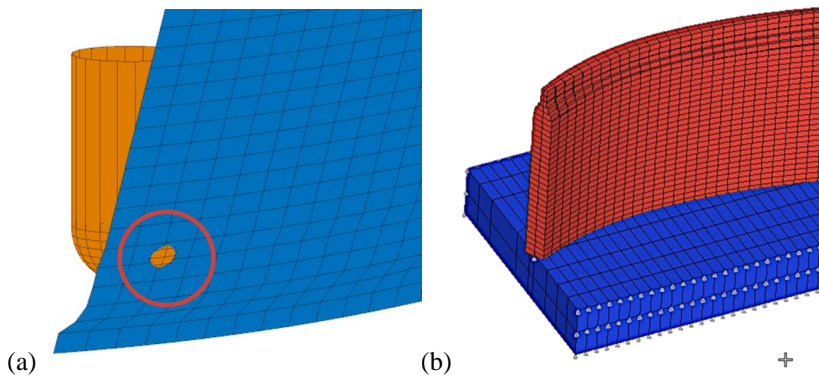


Figure 6.11: Stock geometry updating: calculation of the engagement (a) updated FE model (b).

The calculated engagements are then used to update the nodal thickness of the shell elements, as shown by Figure 6.11 (b). This procedure enables to calculate workpiece FRFs per each driving point of the milling toolpath, considering the material removal. Figure 6.12 shows an example of the calculated workpiece FRF: the FRF at the leading edge in the direction normal to the camber line are evaluated at different distances from the base (i.e. the substrate). This figure highlights a significant shift of the resonance frequency, confirming the dependency of the workpiece FRFs on the position of the driving point and on the removed material.

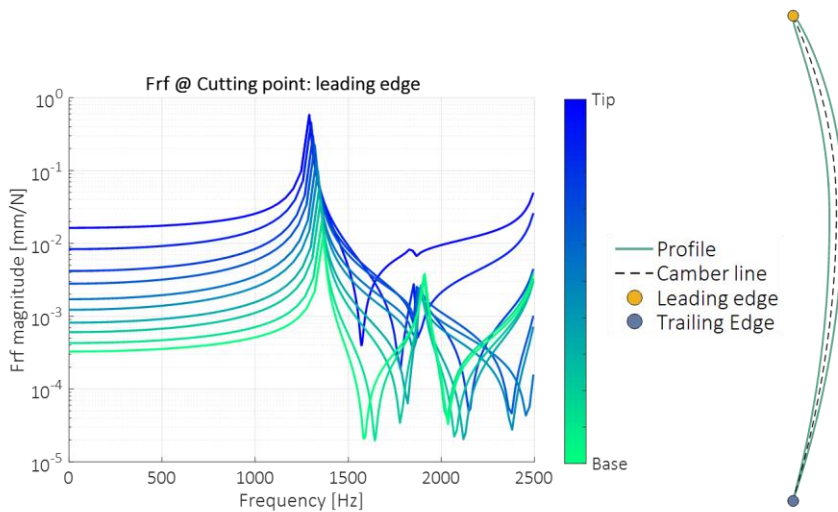


Figure 6.12: Workpiece FRFs evaluated at the leading edge at different distances from the base.

For the FRFs calculation this work used the commercial FE solver MSC Nastran. The FRFs calculation was carried out using the modal superposition method to increase the computational efficiency. The material properties used in the simulation were set according to the following values: Young's modulus $2.0e^{+5}$ MPa, mass density $7.85e^{+3}$ kg/m³, Poisson ratio 0.31, structural damping coefficient $5.0e^{-3}$. The calculation of the FRFs for the test case took about 2 hr. and 8 minutes on an 8 cores workstation. In this time more than 5000 FRFs were calculated, highlighting the computational efficiency of the proposed technique.

The final step of the proposed algorithm is the composition of the workpiece FRFs with the tool contribution. This achieved by summing the tooltip and workpiece FRFs according to the orientation of the tool (lead and tilt angle). In this work, the tooltip FRF is directly measured by impact testing experiments. It must be pointed out that in the machine used in this study the dynamic behavior is almost independent on the direction [185], enabling to use a single measurement. Figure 6.13 compares the combined FRF with workpiece FRF evaluated at a specific location and with the tooltip one. Despite the contribution of the workpiece is dominant in this case, a contribution of the tool dynamics can be observed around 1000 Hz.

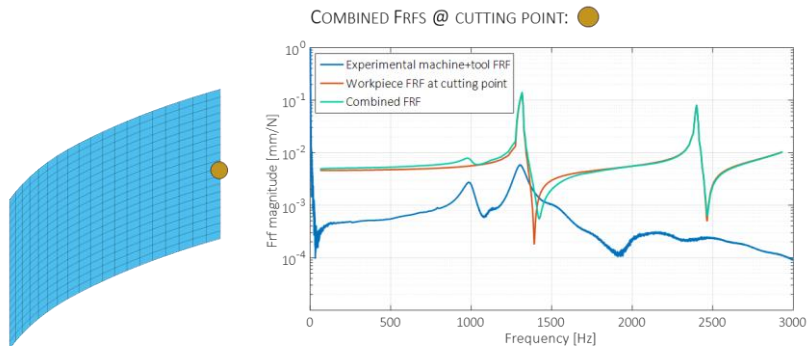


Figure 6.13: Comparison between the workpiece, tooltip and combined FRF.

The presented technique was implemented in the Matlab software, which has the possibility of calling the execution of Nastran simulation to calculate the required FRFs.

The accuracy of the proposed technique was tested by performing impact testing experiments on the workpiece after the roughing phase. The stock model was updated by the proposed technique, according to the roughing cycle. The FRFs were then calculated in the measurement points using the updated model. These FRFs were compared with the experimental data. Figure 6.14 shows an example of such comparison. The test highlights that the proposed technique enables an accurate calculation of the workpiece FRFs, achieving an error on the modes resonance frequency lower than 5%. Therefore, this test confirms that the proposed technique is effective in predicting the changing dynamics of the workpiece, allowing to use it for the optimization of the spindle speed.

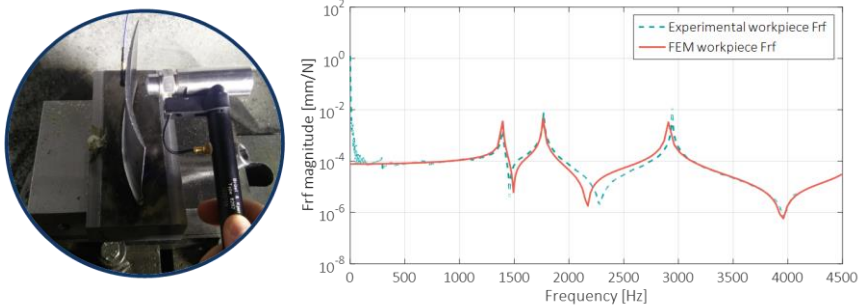


Figure 6.14: Results of the comparison between impact testing FRFs and the calculated ones.

Optimization strategies: overview

The proposed approach identifies the dynamics of the tool-workpiece system during the whole machining cycle. Hence it can be coupled with any optimization strategy to achieve different goals, computing an optimized machining cycle.

Two main dynamic phenomena could arise in machining thin-walled components: forced and chatter vibrations. The former one is always present in milling since the cutting forces in milling are time dependent. However, the forced vibrations can have a detrimental effect on the workpiece roughness and accuracy if the cutting forces excite the workpiece eigenmodes. This condition depends on the frequency content of the cutting forces, namely on the spindle speed. On the opposite, chatter is an unstable regenerative phenomenon which occurs for specific cutting conditions [177]. In milling, once the axial and radial depths of cut are fixed, the occurrence of chatter is related to the selected spindle speed according to the stability lobe diagram. Hence the spindle speed is the most suitable parameter for an optimization, as already highlighted in the state of the art review. However, the selection of spindle speed has conflicting requirements for forced and chatter vibrations. To reduce the forced vibrations, the spindle speed should be selected to keep the harmonics of the cutting force as far as possible from the resonance frequencies of the system. This condition reduces the relative tool-workpiece displacements during the cycle. On the contrary, for chatter avoidance the optimal spindle speeds result in cutting force harmonics which excite the resonance frequency of the dominant mode [182].

According to these considerations, the spindle speed optimization strategy should be tailored for the specific application. This work applies three optimization strategies, with the aim of showing the potential applications of the proposed approach.

Strategy A. Chatter avoidance strategy using an optimized spindle speed, constant throughout all the cycle.

Strategy B. Strategy that aims at minimizing the effect of forced vibrations.

Strategy C. Chatter avoidance strategy using an optimized spindle speed variable throughout all the cycle.

All the strategies were applied to the finishing phase of the test case milling cycle. The fundamental input was the dynamic behavior of the system at the cutting points, computed by the proposed technique. The following paragraphs outlines the tested optimization strategies.

Optimization strategies: strategy A

The aim of this strategy is to avoid chatter occurrence by selecting an optimal spindle speed, constant throughout all the machining cycle. As earlier mentioned, the best condition to avoid chatter occurrence is to select a spindle speed that allows one of the cutting force harmonics to excite the dominant mode of the combined tool-workpiece FRF. In milling, the cutting forces are time-dependent periodic functions. The main frequency of such signals is the tooth pass frequency, defined by Eq. 51:

$$f_{tp} = \frac{N}{60} n_z \quad \text{Eq. 51}$$

Where n_z is the number of flutes of the tool and N is the spindle speed. Hence, the frequency content of the cutting forces is constituted by all the harmonics of the tooth pass frequency. The amplitude of the harmonics depends on the type of tool and on the depths of cut [171]. Figure 6.15 shows the Fourier transform of the cutting force component normal to the machined surface, for the test case cutting conditions (i.e., $a_r = 0.2 \text{ mm}$, $a_p = 0.5 \text{ mm}$).

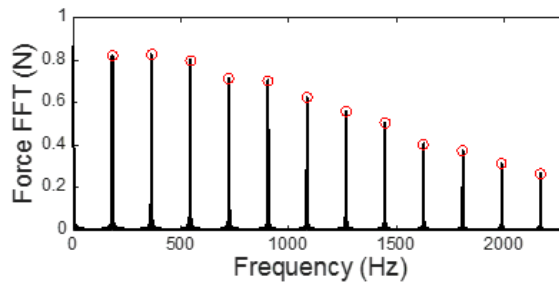


Figure 6.15: Frequency content of the cutting forces for a peripheral milling operation with a ball nose tool.

Hence, modifying the spindle speed, it is possible to excite different structural behaviors of the tool-workpiece response.

As earlier mentioned, the goal of this optimization strategy is to define a constant spindle speed allowing to excite the dominant mode of the combined response. The dominant mode is defined as the one which results in the highest magnitude peak in the FRF. Since the frequency of the dominant mode changes throughout the whole cycle, an average value of the dominant mode frequency was calculated among all the responses of every driving point excited during the finishing cycle. Figure 6.16 outlines this averaging operation, showing a subset of all the considered FRFs. For the selected test case, this operation calculated an average dominant frequency of 1302 Hz. Based on the cutting speed achievable by the selected tool it was decided to excite the dominant mode with the 7th harmonic of the toothpass frequency. This resulted in a spindle speed of 5580 RPM.

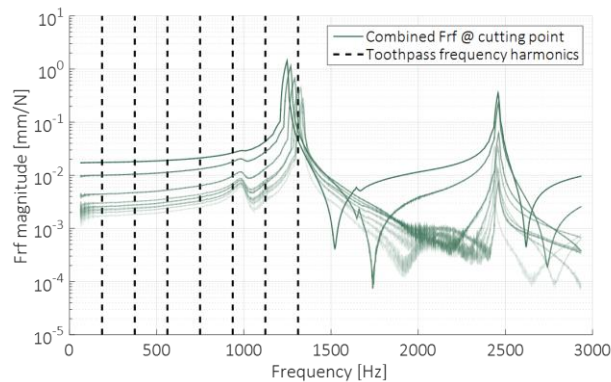


Figure 6.16: Outline of the optimization strategy A.

Optimization strategies: strategy B

The goal of this strategy is to minimize the effect of the forced vibrations. This is achieved by minimizing the relative displacement between the tool and the workpiece. This requires the knowledge of the tool-workpiece FRF and of the cutting forces. The combined dynamic response is calculated by means of the proposed technique, considering the driving point response in a direction perpendicular to the machined surface. A detailed calculation of the cutting forces would require the knowledge of the cutting coefficient for the specific material-tool couple. However, the cutting force coefficients act as a scale factor on the amplitude of cutting force harmonics, namely the relative value of the harmonics is independent on such parameters [172]. For the sake of the optimization, achieving a detailed calculation of the displacement is not crucial. Thus, using an accurate value of the cutting force coefficient is not mandatory. In this work, a pseudo cutting force is defined to perform the optimization independently on the cutting coefficients. The cutting forces are simulated considering the finishing cutting condition, tool and using standard values of the cutting force coefficients for mild steel. The simulation is carried out using the software CutPro. The magnitude of the vector sum of the feed and cross feed components of the cutting forces is then analyzed in the frequency domain, highlighting its harmonics, as shown in Figure 6.17.

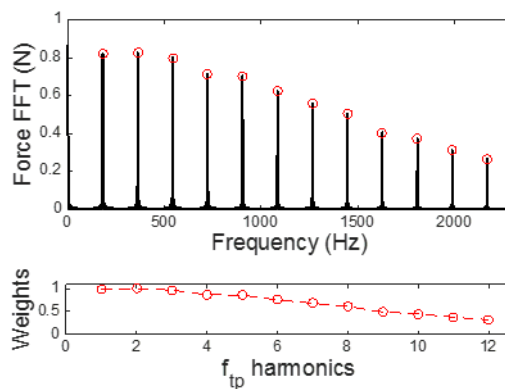


Figure 6.17: Weights assigned to the cutting force harmonics for optimization.

The amplitude spectrum is then scaled, dividing the amplitude of the harmonics by the value of the fundamental one (corresponding to the tooth pass frequency). This leads to the definition of a weight (w_i) per each harmonic. The set of calculated weights has all the information concerning the relative amplitude of the cutting force harmonics. Considering the hypothesis in which all the harmonics have phase zero, the relative displacement can be expressed as the product of the driving point FRF by the weights, as shown in Eq. 52:

$$F_{obj} = \sum_{i=1}^n w_i |G_{dp}(if_{tp})| \quad \text{Eq. 52}$$

Where F_{obj} is the displacement, i.e. the objective function of the optimization; $G_{dp}(if_{tp})$ is the FRF evaluated at the i^{th} harmonic of the toothpass frequency; n is the number of harmonics considered in the cutting force simulation (in this case 12). Recalling Eq. 51, the objective function becomes a direct function of the spindle speed, as shown by Eq. 53:

$$F_{obj}(N) = \sum_{i=1}^n w_i \left| G_{dp}\left(i \frac{Nn_z}{60}\right) \right| \quad \text{Eq. 53}$$

The optimization consists in minimizing the objective function defined in Eq. 53 for each driving point of the FE model. Each optimization is carried out within the spindle speed range provided by the tool manufacturer. The minimization of the function was carried out using the GA algorithm of the Matlab software [186]. The result is a variable spindle speed which is used to update the G-code, resulting in a part program having an assigned spindle speed for every line block. An extract of the calculated spindle speed is shown in Figure 6.18.

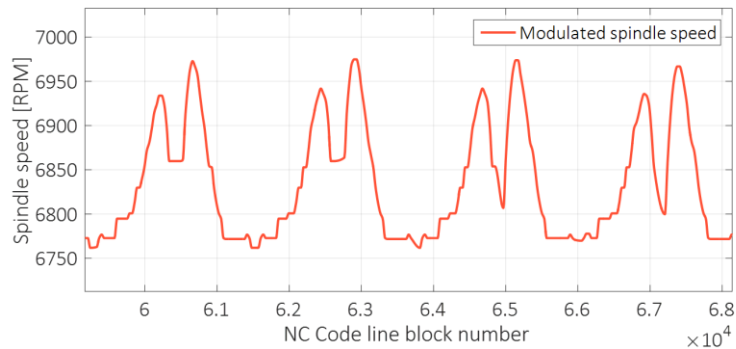


Figure 6.18: Modulated spindle speed pattern calculated by the optimization strategy B.

The stepwise trend of the spindle speed is due to the dynamic behavior of the workpiece. Figure 6.19 shows the first two modes of the airfoil.

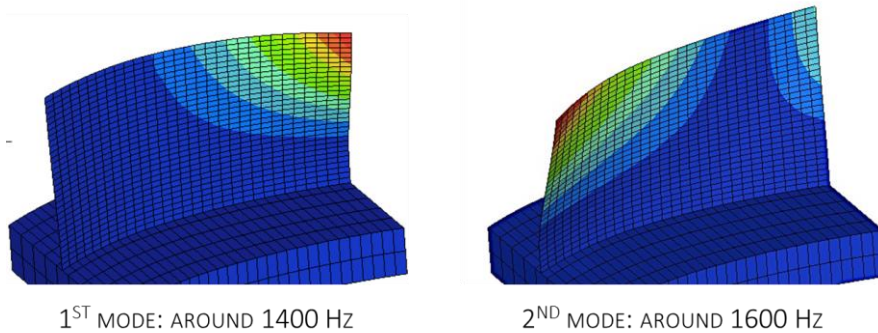


Figure 6.19: The first two modes of the airfoil during the finishing step

The first mode is a bending vibration of the trailing edge region, while the second one involves mainly the leading edge region. Thus, when the tool is cutting in the vicinity of the trailing edge, the optimization returns a spindle speed value which avoids to excite the first mode. On the opposite, when the tool is in the vicinity of the trailing edge, the objective function is more influenced by the second mode, resulting in a different spindle speed.

Optimization strategies: strategy C

This optimization strategy is based on the same concept of the strategy A, namely to avoid chatter occurrence by exciting the dominant mode with one of the tooth pass frequency harmonics. However, this strategy does not calculate a constant spindle speed value. On the opposite, an optimal spindle speed is calculated for each driving point of the toolpath exciting the instantaneous dominant mode. As in the strategy A, the spindle speed was calculated to allow the 7th harmonic of the tooth pass frequency to excite the instantaneous dominant mode. This resulted in a part program with a variable spindle speed, similar to the one produced by B.

Results and discussion

The three specimens of the test case were machined by using the depicted optimization strategy. The geometry of the resulting airfoils was scanned by means of a CMM Mitutoyo Euro Apex C776, to assess the effectiveness of the different optimization techniques. Figure 6.20 shows a comparison between the reference geometry and the measured one. The compared quantities are the camber line pattern along the chordal distance and the blade thickness along the chordal distance.

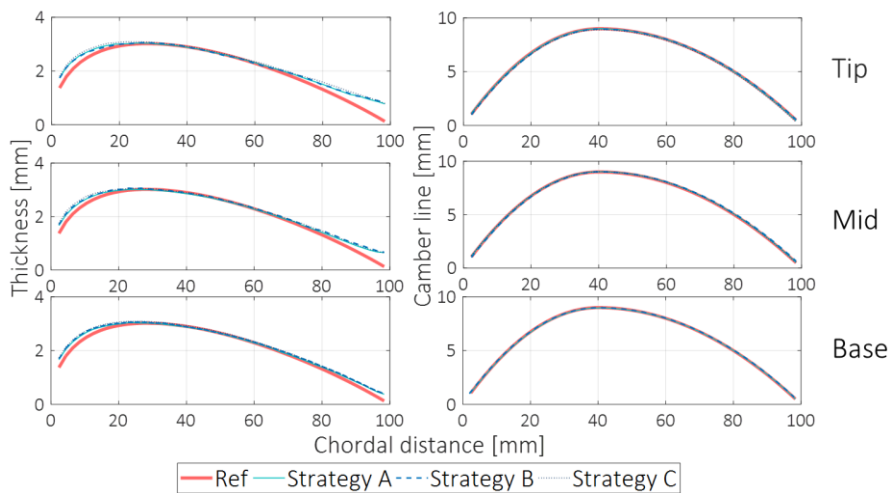


Figure 6.20: Comparison of measured camber lines and airfoil thickness with the reference one.

The comparison highlights a general agreement between the measured and the reference data. The camber line pattern is accurate in all the three specimens. For what concerns the thickness, all the optimization strategies led to higher errors in correspondence of the leading and trailing edge. This is expected since these areas are the most flexible part of the workpiece because of its modal behavior (Figure 6.19). In the same way, the error increases with the distance from the substrate with its maximum value at the top of the blade. However, this analysis does not highlight any significant difference between the optimization strategies. Figure 6.21 shows the error on the blade thickness with respect to the reference geometry along the chordal distance and the blade height.

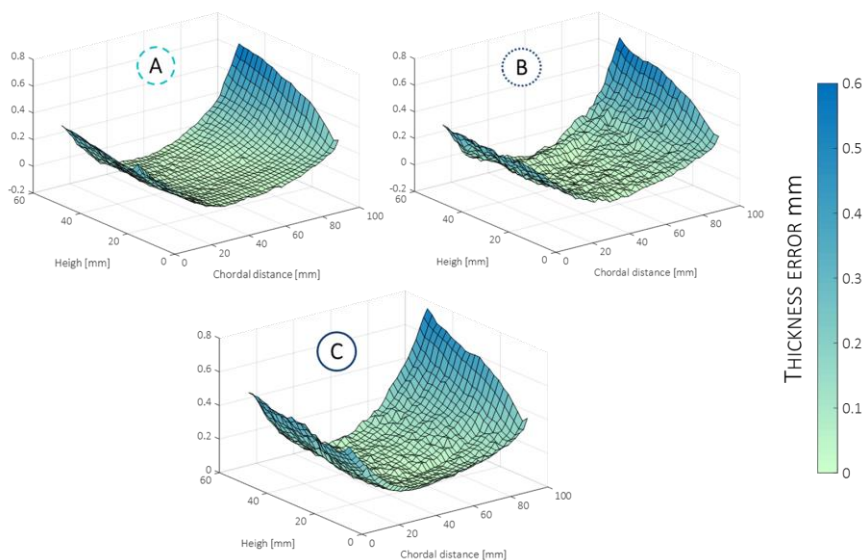


Figure 6.21: Thickness error along chordal distance and blade height for the three specimens.

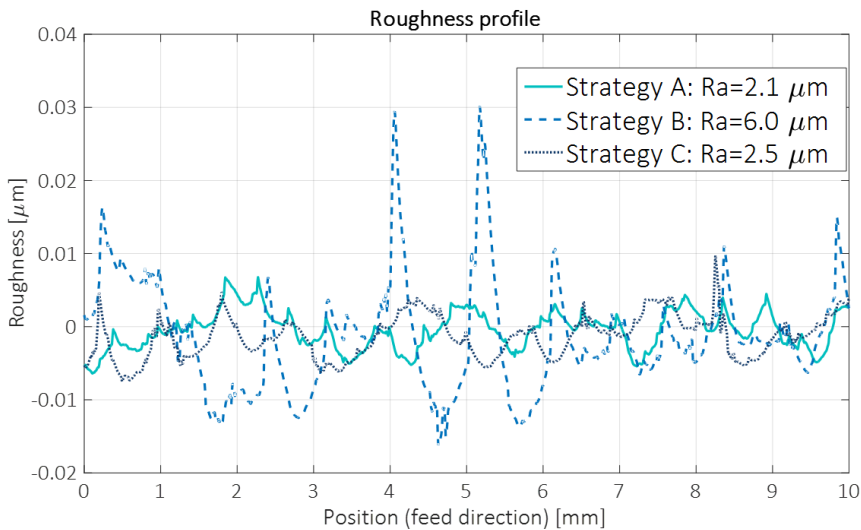


Figure 6.22: Comparison of the roughness achieved by using the three optimization strategies.

It is highlighted that all the three strategies lead to low error, compliant with the required tolerances in standard airfoils. However, the specimen manufactured using the strategy that aims at reducing the effect of forced vibrations (strategy B), leads to a wavy error surface. This was interpreted as an indicator of a poor surface finish. To verify this hypothesis, the roughness of the specimens was measured along the chordal distance. The results of such tests are shown in Figure 6.22, both in terms of measured surface profiles and of surface roughness. The roughness comparison highlights what expected from the analysis of the thickness error: the strategy B leads to a higher roughness with respect to both chatter avoidance strategies ($6.0\ \mu\text{m}$ against $2.1\ \mu\text{m}$ and $2.5\ \mu\text{m}$).

The presented results lead to the following conclusions: the chatter avoidance strategies were more effective for the specific test case since the chatter vibration was the most severe vibration phenomenon. The minimum displacement strategy, tailored to avoid forced vibrations, brought the tool-workpiece system to work above the stability limit. No significant difference was found between the strategy A and C, namely the constant and variable spindle speed chatter avoidance techniques. The reason of this similarity could be the dynamic behavior of the combined system: despite the dominant mode significantly shifted during the finishing cycle, it did not shifted enough to affect the effectiveness of the constant speed strategy.

In light of these conclusions, the three optimization strategies can be useful, depending on the selected depth of cut. Figure 6.23 provides a graphical outline of this concept, referring to a stability lobe diagram.

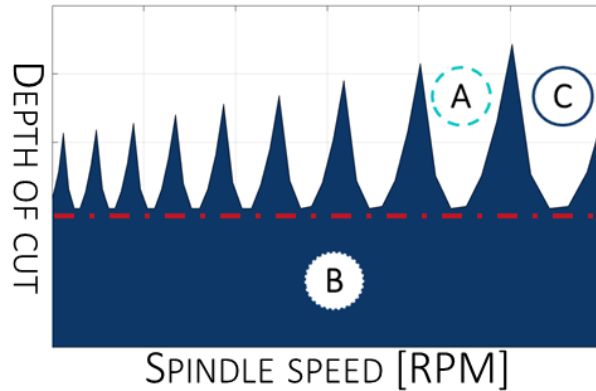


Figure 6.23: Applicability ranges of the different optimization strategies.

The lobe diagram has an asymptotic limit depth of cut (red line in Figure 6.23). Below this limit, the spindle speed can be arbitrarily selected without resulting in chatter vibrations. Hence, if the selected depth of cut is below this limit, the strategy B is the best suited to increase the performances of the process. On the opposite, the chatter avoidance strategy are the best suited one if the depth of cut is higher than its asymptotic value. In this case the optimization exploits the lobbing effect, ensuring stable cutting conditions. The selection of a variable or constant spindle speed strategy depends on the amplitude of the dominant mode shifting during the process.

6.3. Conclusions and remarks

This chapter dealt with the issues arising in the second step of the hybrid WAAM-milling process, i.e. the milling operations required to achieve the required accuracy and surface finish. The aim was to analyze the possible issues that could arise in such operation, affecting the outcome of the whole hybrid process. Two aspects were considered: the machinability of the WAAM material and the issues arising when milling thin walled parts. On the machinability side, the importance of considering the material cutting force behavior was highlighted by a machinability analysis of a tool steel. To improve the quality of the milling operations of thin walled parts, this thesis proposes an algorithm to calculate the changing dynamic behavior of the workpiece. This enables to optimize the spindle speed, reducing the detrimental effect of the vibration phenomena.

In conclusion, to achieve an effective hybrid process, the milling process should be carefully planned, considering the technological constraints posed by the WAAM material and the geometry of the WAAM workpieces.

Table 6.6 summarizes the contribution to the state of the art depicted in this chapter.

Table 6.6: Summary of the thesis contributions to the machining of WAAM components.

Machining of WAAM components
WAAM material machinability: <i>Thesis contribution</i>
Machinability analysis of AISI H13 [4]:
Highlighting of the cutting force variation between AM and wrought material.
Machining of thin walled components: <i>Thesis contribution</i>
Changing workpiece dynamics calculation procedure [187]:
Possibility of optimizing the spindle speed to increase process performances.

7. Conclusions and final remarks

This thesis deals with the hybrid WAAM-milling process. This technology has significant advantages compared to other hybrid techniques: it provides the possibility of manufacturing very large parts, it has a high deposition rate, it has a reduced installation and feedstock material cost. However, several factors are still limiting its diffusion among the manufacturing companies. These drawbacks involve both the steps of the process, namely the WAAM deposition and the subsequent finishing by milling. The aim of this PhD work is to analyze the criticalities of such process, proposing improvements to the techniques currently used to tackle them.

Since the object of the study is a hybrid process, this thesis is divided in two main parts: the first one tackles the WAAM process while the second one is focused on the issues arising when milling a component produced by WAAM.

While milling is a consolidated process, WAAM is still undergoing its development stage, requiring large research efforts to increase its technology readiness level. Therefore, most of the thesis is dedicated to WAAM.

The WAAM process uses electric arc welding to deposit layers of metal creating the component geometry. Scientific literature highlights that the thermal issues are the most severe limitation of this technology. The large amount of heat introduced by the welding arc results in a non-temperature field of the workpiece. This can cause significant issues: residual stresses, workpiece distortions, uneven material properties and possible part collapse. A further analysis highlighted that process macro-scale simulation is a suitable strategy to predict the occurrence of the thermal issues and to assess the effectiveness of suitable mitigation strategies. The main issue of this approach is to achieve a trade-off between simulation accuracy and computational efficiency. This thesis proposes three improvements to the state of the art simulation technique: a new heat source model, a new technique to include the latent heat of fusion and a technique to reduce the number of elements required to discretize the substrate. All the techniques enable to reduce the simulation time without resulting in a significant loss of accuracy. The proposed heat source model is more closely related to the actual process physics than the state of art one. Hence, it does not require tuning operations to achieve accurate results. This results in a reduction of the simulation set-up time. The latent heat model enables to increase the simulation time step, reducing the overall calculation time. The substrate mesh coarsening technique reduces the number of model DOFs, making each simulation step more efficient. All the proposed simulation techniques are validated by means of experimental tests, verifying the accuracy in predicting both the workpiece temperature and residual deformations.

Having proposed improvements to the simulation technique, the thesis focuses their application to the heat accumulation problem, a detrimental issue responsible for workpiece

collapse and material properties unevenness. Unlike for the residual stresses and distortions issues, the process simulation was never applied to the heat accumulation. This thesis proposes two approaches: the application of jet impingement cooling to increase the heat transfer rate to the environment and a simulation based algorithm to schedule idle times between the layers allowing the component to cool down. The jet impingement technique enables to overcome the limitations of the current cooling systems used in WAAM in terms of effectiveness and integration on existing machines. The process simulation is used to assess the effectiveness of this cooling system applied to WAAM. A jet impingement model is developed and validated. It is then included in the validated simulation of the WAAM process. The results of simulations with and without jet impingement are compared. It results that the jet impingement cooling enables to limit the increase of both molten pool size and interpass temperature, the most detrimental consequence of the heat accumulation. The alternative approach used to prevent heat accumulation is to include interlayer idle times. The process simulation was applied to define an algorithm that calculates the idle times required to achieve the required interpass temperature on a specific workpiece, material and process parameters. The algorithm calculates a specific idle time per each layer. This results in a resulting in a constant molten pool size. A test case is manufactured using the proposed idle times scheduling technique. It is shown that the selected idle times prevent major structural collapses, confirming the effectiveness of the proposed approach.

The second part of the thesis is dedicated to the milling of WAAM components. Despite milling is a consolidated process, WAAM processed material and WAAM components geometry present specific criticalities. Since achieving an accurate milling process is crucial for the performances of the overall hybrid technology, requiring to carefully consider the issues related to this phase.

This thesis identifies two main issues related to the milling of WAAM components: the machinability of the WAAM material and the vibrations when milling thin walled parts. For what concerns the machinability, this thesis performs machinability tests on a tool steel focused on comparing the cutting forces of the AM processed and wrought material. Such tests highlight that the AM material shows a significant increase of the cutting forces, requiring such aspect to be considered in process planning steps. The other relevant issue is posed by the geometries of the WAAM components, involving thin walled features prone to vibrations in milling. This thesis develops a simulation based algorithm to predict the changing dynamic behavior of the workpiece. This enables to optimize the spindle speed pattern during the milling cycle, preventing the detrimental effects caused by tool and workpiece vibrations. The proposed technique is validated by impact testing experiments. Three different optimization techniques are proposed and applied to machine an actual test case. The results in terms of accuracy and surface finish point out that the optimization strategy must be carefully selected with respect to the cutting conditions. Nevertheless, it is highlighted that a suitable optimization of the spindle speed produces significant improvements in terms of surface finish.

The following table summarizes the thesis contributions to the state of the art.

Process simulation

Novel heat source model tailored for GMAW [1]:

Increased accuracy and reduction of tuning operations

Novel latent heat modelling technique [2]:

Increasing of the minimum time step requirements

Novel substrate mesh coarsening technique [2]

Reduction of the DOFs required to discretize the workpiece substrate

Heat accumulation

Jet impingement application to WAAM process [3]:

Increase of the heat transfer rate, constant molten pool size.

Adaptive idle times scheduling based on FE simulation:

Constant molten pool size and interpass temperature.

Milling of WAAM parts

Machinability analysis of AISI H13 [4]:

Highlighting of the cutting force variation between AM and wrought material.

Changing workpiece dynamics calculation procedure [187]:

Possibility of optimizing the spindle speed to increase process performances.

Table 7.1: Summary of the thesis contribution to the state of the art

In terms of quantitative achievements, the thesis results can be summarized as follows:

- The combined application of the proposed latent heat and heat source models enabled to achieve an accuracy of 1.5% in predicting the peak temperature in a WAAM operation.
- The proposed substrate mesh coarsening technique allowed to reduce the simulation time of about 50%, compared to the traditional mesh biasing, achieving an error below 0.16 mm on workpiece distortions.
- The numerical validation highlighted the effectiveness of the jet impingement cooling in controlling the heat accumulation issue. The test case selected for the validation highlighted a reduction of 87% of the molten pool size at the 10th layer, compared to the same test case without jet impingement.
- The proposed idle time selection algorithm resulted in maximum increase of the molten pool volume of 15% over the layers of the workpiece.

Based on the presented activities and results, this thesis draws six main conclusions:

- The efficiency of WAAM process simulation can be increased without affecting its accuracy, provided that the actual process physics is considered when introducing simplifying assumptions.
- FE modeling is crucial in predicting the outcome of the WAAM process, both in thermal and mechanical domains.
- The heat accumulation is a further issue which can be effectively overcome using the process simulation. Moreover, process modelling provides the possibility of carrying out virtual what if analysis, enabling a time and cost-efficient investigation of the WAAM process.
- Achieving a successful hybrid operation requires a careful planning of the post process milling.
- The impact of WAAM process on the specific cutting forces should be considered. More generally, the WAAM process affects the material behavior which can result in complications during the machining step.
- Besides the WAAM step, the FE simulation is a useful tool to increase the performance of the post process milling. Its usage in predicting workpiece dynamics is crucial to optimize the spindle speed.

The results achieved in this thesis provided the following ideas for future works:

- Introduce further simplification to the FE model of the WAAM process, developing a simulation technique specifically tailored for the idle times calculations.
- Analyzing the effect of jet impingement and adaptive idle times on the mechanical properties of the WAAM material through process simulations and experiment.
- Identify a correlation between the cutting force coefficients and the material thermal history during the WAAM deposition, enabling a fully predictive approach for the calculation of the cutting force.
- Identifying a single comprehensive strategy to optimize the spindle speed. The goal would be developing an approach which would allow to consider both forced and chatter vibrations.

Acknowledgements

The work presented in this thesis was carried out in the MTRL (Manufacturing Technology Research Laboratory) of the Department on Industrial Engineering of the University of Firenze. Therefore, first I would like to thank my supervisors Dr. Gianni Campatelli and Dr. Antonio Scippa for their constant guide and support during all the activities. Moreover, I must express my gratitude to all the colleagues which provided constant suggestions and active contribution to the presented research: Lorenzo, Niccolò, Giuseppe, Riccardo, Sandro, Lisa.

I would like to thank Professor Sasahara and Hisataka Takagi of the Tokyo University of Agriculture and Technology for their contribution to the work related to the AISI H13 Machinability.

I would like to acknowledge Prof. Yamazaki, Prof. Soshi and Dr. Mori, since MTTRF (Machine Tool Technology Research Foundation) loaned the NMV1500DCG milling machine to MTRL. This machine was important for the research presented in this thesis and to improve my practical knowledge of machine tools.

I would like to thank my girlfriend Francesca for her constant presence in my life and for her support during all these year.

I am also grateful to my parents and all my friends.

Bibliography

- [1] F. Montevercchi, G. Venturini, A. Scippa, G. Campatelli, Finite Element Modelling of Wire-arc-additive-manufacturing Process, in: *Procedia CIRP*, 2016: pp. 109–114. doi:10.1016/j.procir.2016.08.024.
- [2] F. Montevercchi, G. Venturini, N. Grossi, A. Scippa, G. Campatelli, Finite Element mesh coarsening for effective distortion prediction in Wire Arc Additive Manufacturing, *Addit. Manuf.* 18 (2017) 145–155. doi:10.1016/j.addma.2017.10.010.
- [3] F. Montevercchi, A. Scippa, G. Campatelli, Analysis of air jet impingement cooling applied to wire arc additive manufacturing process, in: *XIII Convegno dell'Associazione Ital. Di Tecnol. Mecc.*, 2017: pp. 11–13.
- [4] F. Montevercchi, N. Grossi, H. Takagi, A. Scippa, H. Sasahara, G. Campatelli, Cutting Forces Analysis in Additive Manufactured AISI H13 Alloy, in: *Procedia CIRP*, 2016. doi:10.1016/j.procir.2016.04.034.
- [5] B.P. Conner, G.P. Manogharan, A.N. Martof, L.M. Rodomsky, C.M. Rodomsky, D.C. Jordan, J.W. Limperos, Making sense of 3-D printing: Creating a map of additive manufacturing products and services, *Addit. Manuf.* 1 (2014) 64–76. doi:10.1016/j.addma.2014.08.005.
- [6] X. Wang, S. Xu, S. Zhou, W. Xu, M. Leary, P. Choong, M. Qian, M. Brandt, Y.M. Xie, Topological design and additive manufacturing of porous metals for bone scaffolds and orthopaedic implants: A review, (2016). doi:10.1016/j.biomaterials.2016.01.012.
- [7] F. Weng, C. Chen, H. Yu, Research status of laser cladding on titanium and its alloys: A review, *Mater. Des.* 58 (2014) 412–425. doi:10.1016/j.matdes.2014.01.077.
- [8] C. Beyer, Strategic Implications of Current Trends in Additive Manufacturing, *J. Manuf. Sci. Eng.* 136 (2014) 64701. doi:10.1115/1.4028599.
- [9] W.E. Frazier, Metal additive manufacturing: A review, *J. Mater. Eng. Perform.* 23 (2014) 1917–1928. doi:10.1007/s11665-014-0958-z.
- [10] H.H. Zhu, L. Lu, J.Y.H. Fuh, Development and characterisation of direct laser sintering Cu-based metal powder, in: *J. Mater. Process. Technol.*, Elsevier, 2003: pp. 314–317. doi:10.1016/S0924-0136(03)00755-6.
- [11] J. Milewski, G. Lewis, D. Thoma, G. Keel, R. Nemeč, R. Reinert, Directed light fabrication of a solid metal hemisphere using 5-axis powder deposition, *J. Mater. Process. Technol.* 75 (1998) 165–172. doi:10.1016/S0924-0136(97)00321-X.
- [12] S. Jhavar, N.K. Jain, C.P. Paul, Development of micro-plasma transferred arc (μ -PTA) wire deposition process for additive layer manufacturing applications, *J. Mater. Process. Technol.* 214 (2014) 1102–1110.

- doi:10.1016/j.jmatprotec.2013.12.016.
- [13] Roland Berger, Additive Manufacturing: A game changer for the manufacturing industry?, Rol. Berger Strateg. Consult. (2013) 33. http://www.rolandberger.com/media/pdf/Roland_Berger_Additive_Manufacturing_20131129.pdf.
- [14] J.M. Flynn, A. Shokrani, S.T. Newman, V. Dhokia, Hybrid additive and subtractive machine tools - Research and industrial developments, *Int. J. Mach. Tools Manuf.* 101 (2016) 79–101. doi:10.1016/j.ijmachtools.2015.11.007.
- [15] S.W. Williams, F. Martina, A.C. Addison, J. Ding, G. Pardal, P. Colegrove, Wire + arc additive manufacturing, *Mater. Sci. Technol.* (2015) 1743284715Y.000. doi:10.1179/1743284715Y.0000000073.
- [16] D. Ding, Z. Pan, D. Cuiuri, H. Li, Wire-feed additive manufacturing of metal components: technologies, developments and future interests, *Int. J. Adv. Manuf. Technol.* 81 (2015) 465–481. doi:10.1007/s00170-015-7077-3.
- [17] D. Ding, Z. Pan, D. Cuiuri, H. Li, A practical path planning methodology for wire and arc additive manufacturing of thin-walled structures, *Robot. Comput. Integr. Manuf.* 34 (2015) 8–19. doi:10.1016/j.rcim.2015.01.003.
- [18] J. Alcisto, A. Enriquez, H. Garcia, S. Hinkson, T. Steelman, E. Silverman, P. Valdovino, H. Gigerenzer, J. Foyos, J. Ogren, J. Dorey, K. Karg, T. McDonald, O.S. Es-Said, Tensile properties and microstructures of laser-formed Ti-6Al-4V, *J. Mater. Eng. Perform.* 20 (2011) 203–212. doi:10.1007/s11665-010-9670-9.
- [19] M. Gurr, Chapter 01477 - 8.4 Rapid Prototyping, *Ref. Modul. Mater. Sci. Mater. Eng.* (2015) 1–27. doi:10.1016/B978-0-12-803581-8.01477-6.
- [20] K.P. Karunakaran, A. Bernard, S. Suryakumar, L. Dembinski, G. Taillandier, Rapid manufacturing of metallic objects, *Rapid Prototyp. J.* 18 (2012) 264–280. doi:10.1108/13552541211231644.
- [21] W.W. Wits, S.J. Weitkamp, J. Van Es, Metal additive manufacturing of a high-pressure micro-pump, in: *Procedia CIRP*, Elsevier, 2013: pp. 252–257. doi:10.1016/j.procir.2013.05.043.
- [22] Masterclass: Advanced aviation - | GE Look ahead | The Economist, (n.d.). <http://gelookahead.economist.com/slideshow/look-ahead-master-class-advanced-aviation/> (accessed November 15, 2017).
- [23] J.M. Flynn, A. Shokrani, S.T. Newman, V. Dhokia, Hybrid additive and subtractive machine tools - Research and industrial developments, *Int. J. Mach. Tools Manuf.* 101 (2016) 79–101. doi:10.1016/j.ijmachtools.2015.11.007.
- [24] Z. Zhu, V. Dhokia, S.T. Newman, The development of a novel process planning algorithm for an unconstrained hybrid manufacturing process, *J. Manuf. Process.* 15 (2013) 404–413. doi:10.1016/j.jmapro.2013.06.006.
- [25] S. Yi, F. Liu, J. Zhang, S. Xiong, Study of the key technologies of LOM for functional metal parts, *J. Mater. Process. Technol.* 150 (2004) 175–181. doi:10.1016/j.jmatprotec.2004.01.035.
- [26] R.N. Raoelison, C. Verdy, H. Liao, Cold gas dynamic spray additive manufacturing today: Deposit possibilities, technological solutions and viable applications, *Mater. Des.* 133 (2017) 266–287. doi:10.1016/j.matdes.2017.07.067.
- [27] Additive manufacturing | TRUMPF, (n.d.). https://www.trumpf.com/en_INT/applications/additive-manufacturing/ (accessed September 19, 2017).
- [28] Be Additive Manufacturing, (n.d.). <http://beam-machines.fr/en/about> (accessed

- September 19, 2017).
- [29] 3D Printing Electronics Laser Additive Manufacturing Systems, (n.d.). <https://www.optomec.com/> (accessed September 19, 2017).
- [30] Coaxial laser wire cladding head COAXwire - Fraunhofer IWS, (n.d.). https://www.iws.fraunhofer.de/en/business_fields/surface_treatment/laser_cladding/system_technology/COAXwire.html (accessed September 19, 2017).
- [31] Wire feed Additive Manufacturing vs. Powder Methods | Sciaky, (n.d.). <http://www.sciaky.com/additive-manufacturing/wire-am-vs-powder-am> (accessed September 19, 2017).
- [32] GEFERTEC, (n.d.). <http://gefertec.scansonic.de/> (accessed September 19, 2017).
- [33] 金属3Dプリンタ「Value Arc MA5000-S1」を新発売, (n.d.). http://www.mutoh-hd.co.jp/pdf/20150721_MA5000-S1.pdf (accessed January 19, 2018).
- [34] H. Zhang, J. Xu, G. Wang, Fundamental study on plasma deposition manufacturing, *Surf. Coatings Technol.* 171 (2003) 112–118. doi:10.1016/S0257-8972(03)00250-0.
- [35] F. Le, O. Kerbrat, L. Dembinski, J. Hascoet, P. Mognol, Predictive model for environmental assessment in additive manufacturing process, *Procedia CIRP.* 15 (2014) 26–31. doi:10.1016/j.procir.2014.06.031.
- [36] H. Canady, Optomec Improves Additive Repair Technique | Advanced Machines for Aerospace Manufacturing content from Aviation Week, *Aviat. Week.* (2016). <http://aviationweek.com/advanced-machines-aerospace-manufacturing/optomec-improves-additive-repair-technique> (accessed September 19, 2017).
- [37] S.H. Mok, G. Bi, J. Folkes, I. Pashby, Deposition of Ti – 6Al – 4V using a high power diode laser and wire , Part I : Investigation on the process characteristics, 202 (2008) 3933–3939. doi:10.1016/j.surfcoat.2008.02.008.
- [38] F. Brueckner, M. Riede, F. Marquardt, R. Willner, A. Seidel, S. Thieme, C. Leyens, E. Beyer, A.E. Seidel, Process characteristics in high-precision laser metal deposition using wire and powder, *J. Laser Appl.* 29 (2017). doi:10.2351/1.4983237doi.org/10.2351/1.4983237.
- [39] M.S. Węglowski, S. Błacha, A. Phillips, Electron beam welding - Techniques and trends - Review, *Vacuum.* 130 (2016) 72–92. doi:10.1016/j.vacuum.2016.05.004.
- [40] D. Ding, C. Shen, Z. Pan, D. Cuiuri, H. Li, N. Larkin, S. Van Duin, Towards an automated robotic arc-welding-based additive manufacturing system from CAD to finished part, *CAD Comput. Aided Des.* 73 (2016) 66–75. doi:10.1016/j.cad.2015.12.003.
- [41] S. Suryakumar, K.P. Karunakaran, A. Bernard, U. Chandrasekhar, N. Raghavender, D. Sharma, Weld bead modeling and process optimization in Hybrid Layered Manufacturing, *CAD Comput. Aided Des.* 43 (2011) 331–344. doi:10.1016/j.cad.2011.01.006.
- [42] K.M. Taminger, R.A. Hafley, Electron Beam Freeform Fabrication for Cost Effective Near-Net Shape Manufacturing, *Nato Unclassif.* (2004) 19. <https://ntrs.nasa.gov/archive/nasa/casi.ntrs.nasa.gov/20080013538.pdf> (accessed September 18, 2017).
- [43] K.P. Karunakaran, S. Suryakumar, V. Pushpa, S. Akula, Low cost integration of additive and subtractive processes for hybrid layered manufacturing, *Robot. Comput. Integr. Manuf.* 26 (2010) 490–499. doi:10.1016/j.rcim.2010.03.008.
- [44] Have we 3d printed the biggest metal part ever? — WAAMMat, (n.d.). <https://waammat.com/blog/have-we-3d-printed-the-biggest-metal-part-ever> (accessed September 20, 2017).

- [45] W.U.H. Syed, A.J. Pinkerton, L. Li, A comparative study of wire feeding and powder feeding in direct diode laser deposition for rapid prototyping, *Appl. Surf. Sci.* 247 (2005) 268–276. doi:10.1016/j.apsusc.2005.01.138.
- [46] K. Zhang, S. Wang, W. Liu, X. Shang, Characterization of stainless steel parts by Laser Metal Deposition Shaping, *Mater. Des.* 55 (2014) 104–119. doi:10.1016/j.matdes.2013.09.006.
- [47] A.G. Demir, Micro laser metal wire deposition for additive manufacturing of thin-walled structures, *Opt. Lasers Eng.* 100 (2017) 9–17. doi:10.1016/j.optlaseng.2017.07.003.
- [48] P. Wanjara, M. Brochu, M. Jahazi, Electron beam freeforming of stainless steel using solid wire feed, *Mater. Des.* 28 (2007) 2278–2286. doi:10.1016/j.matdes.2006.08.008.
- [49] G. Xu, M. Kutsuna, Z. Liu, K. Yamada, Comparison between diode laser and TIG cladding of Co-based alloys on the SUS403 stainless steel, *Surf. Coatings Technol.* 201 (2006) 1138–1144. doi:10.1016/j.surfcoat.2006.01.040.
- [50] D. Lineberry, Electron Beam Freeform Fabrication, *Res. News, NASA Langley Res. Cent.* (2011). <http://www.nasa.gov/topics/technology/features/ebf3.html>.
- [51] LASERTEC- AdditiveManufacturing series by DMG MORI, (n.d.). <http://us.dmgmori.com/products/lasertec/lasertec-additivemanufacturing/lasertec-65-3d> (accessed September 21, 2017).
- [52] Matsuura Lumex Avance 25 - Additive Manufacturing Machine - Innovate Technologies, (n.d.). <http://innovatetec.com/matsuura-lumex-avance-25-additive-manufacturing-machine/> (accessed September 21, 2017).
- [53] New VARIAXIS j-600AM Grows the Mazak Additive Series, (n.d.). <https://www.mazakusa.com/news-events/news-releases/new-variaxis-j-600am-grows-the-mazak-additive-series/> (accessed September 21, 2017).
- [54] News about DMG MORI, (n.d.). <http://se.dmgmori.com/technical-press/news/metallloobrabotka/440598> (accessed September 21, 2017).
- [55] T. Yamazaki, Development of A Hybrid Multi-tasking Machine Tool: Integration of Additive Manufacturing Technology with CNC Machining, *Procedia CIRP.* 42 (2016) 81–86. doi:10.1016/j.procir.2016.02.193.
- [56] I. Taberero, A. Lamikiz, E. Ukar, L.N. Lopez De Lacalle, C. Angulo, G. Urbikain, Numerical simulation and experimental validation of powder flux distribution in coaxial laser cladding, *J. Mater. Process. Technol.* 210 (2010) 2125–2134. doi:10.1016/j.jmatprotec.2010.07.036.
- [57] VARIAXIS j-600 AM - YouTube, (n.d.). <https://www.youtube.com/watch?v=IqCeJwIWU1s&t=27s> (accessed September 21, 2017).
- [58] Multi-dimensional rolling — WAAMMat, (n.d.). <https://waammat.com/projects/multi-dimensional-rolling> (accessed September 22, 2017).
- [59] P.A. Colegrove, H.E. Coules, J. Fairman, F. Martina, T. Kashoob, H. Mamash, L.D. Cozzolino, Microstructure and residual stress improvement in wire and arc additively manufactured parts through high-pressure rolling, *J. Mater. Process. Technol.* 213 (2013) 1782–1791. doi:10.1016/j.jmatprotec.2013.04.012.
- [60] Hybrid Manufacturing Technologies - Home, (n.d.). <http://www.hybridmanutech.com/> (accessed September 22, 2017).
- [61] LASIMM, (n.d.). <http://www.lasimm.eu/about.html> (accessed September 22, 2017).

- [62] Y. Bandari, S. Williams, J. Ding, F. Martina, Additive Manufacture of Large Structures: Robotic or Cnc Systems, 26th Int. Solid Free. Fabr. Symp. (2015) 17–25. doi:10.1017/CBO9781107415324.004.
- [63] J.. Lancaster, The physics of welding, 1984.
- [64] F. Martina, J. Mehnen, S.W. Williams, P. Colegrove, F. Wang, Investigation of the benefits of plasma deposition for the additive layer manufacture of Ti-6Al-4V, *J. Mater. Process. Technol.* 212 (2012) 1377–1386. doi:10.1016/j.jmatprotec.2012.02.002.
- [65] F. Wang, S. Williams, M. Rush, Morphology investigation on direct current pulsed gas tungsten arc welded additive layer manufactured Ti6Al4V alloy, *Int. J. Adv. Manuf. Technol.* 57 (2011) 597–603. doi:10.1007/s00170-011-3299-1.
- [66] G. Sierra, P. Peyre, F. Deschaux Beaume, D. Stuart, G. Fras, Galvanised steel to aluminium joining by laser and GTAW processes, *Mater. Charact.* 59 (n.d.) 1705–1715. doi:10.1016/j.matchar.2008.03.016.
- [67] B. Baufeld, O. Van der Biest, R. Gault, Additive manufacturing of Ti-6Al-4V components by shaped metal deposition: Microstructure and mechanical properties, *Mater. Des.* 31 (2010) S106–S111. doi:10.1016/j.matdes.2009.11.032.
- [68] B. Baufeld, E. Brandl, O. Van Der Biest, Wire based additive layer manufacturing: Comparison of microstructure and mechanical properties of Ti-6Al-4V components fabricated by laser-beam deposition and shaped metal deposition, *J. Mater. Process. Technol.* 211 (2011) 1146–1158. doi:10.1016/j.jmatprotec.2011.01.018.
- [69] B.A. Szost, S. Terzi, F. Martina, D. Boisselier, A. Prytuliak, T. Pirling, M. Hofmann, D.J. Jarvis, A comparative study of additive manufacturing techniques: Residual stress and microstructural analysis of CLAD and WAAM printed Ti-6Al-4V components, *Mater. Des.* 89 (2016) 559–567. doi:10.1016/j.matdes.2015.09.115.
- [70] C. Shen, Z. Pan, D. Cuiuri, D. Ding, H. Li, Influences of deposition current and interpass temperature to the Fe3Al-based iron aluminide fabricated using wire-arc additive manufacturing process, *Int. J. Adv. Manuf. Technol.* 88 (2017) 2009–2018. doi:10.1007/s00170-016-8935-3.
- [71] H. Geng, J. Li, J. Xiong, X. Lin, F. Zhang, Optimization of wire feed for GTAW based additive manufacturing, *J. Mater. Process. Technol.* 243 (2017) 40–47. doi:10.1016/j.jmatprotec.2016.11.027.
- [72] R. Singh, 2-3. Welding and Joining Processes, in: *Appl. Weld. Eng. - Process. Codes Stand.*, 2012: pp. 147–170. doi:10.1016/B978-0-12-391916-8.00015-7.
- [73] J. Norrish, D. Cuiuri, The controlled short circuit GMAW process: A tutorial, *J. Manuf. Process.* 16 (2014) 86–92. doi:10.1016/j.jmapro.2013.08.006.
- [74] D. Ding, Z. Pan, D. Cuiuri, H. Li, A multi-bead overlapping model for robotic wire and arc additive manufacturing (WAAM), *Robot. Comput. Integr. Manuf.* 31 (2015) 101–110. doi:10.1016/j.rcim.2014.08.008.
- [75] Y. Cao, S. Zhu, X. Liang, W. Wang, Overlapping model of beads and curve fitting of bead section for rapid manufacturing by robotic MAG welding process, (2011). doi:10.1016/j.rcim.2010.11.002.
- [76] J. Xiong, G. Zhang, H. Gao, L. Wu, Modeling of bead section profile and overlapping beads with experimental validation for robotic GMAW-based rapid manufacturing, *Robot. Comput. Integr. Manuf.* 29 (2012) 417–423. doi:10.1016/j.rcim.2012.09.011.
- [77] J. Mehnen, J. Ding, H. Lockett, P. Kazanas, Design for Wire and Arc Additive Layer Manufacture, in: A. Bernard (Ed.), *Proc. 20th CIRP Des. Conf.*, Springer Berlin

- Heidelberg, Berlin, Heidelberg, 2011: pp. 721–727. doi:10.1007/978-3-642-15973-2_73.
- [78] G. Venturini, F. Montecvecchi, A. Scippa, G. Campatelli, Optimization of WAAM Deposition Patterns for T-crossing Features, in: *Procedia CIRP*, 2016: pp. 95–100. doi:10.1016/j.procir.2016.08.043.
- [79] D. Ding, Z. Pan, D. Cuiuri, H. Li, A tool-path generation strategy for wire and arc additive manufacturing, *Int. J. Adv. Manuf. Technol.* 73 (2014) 173–183. doi:10.1007/s00170-014-5808-5.
- [80] J. Xiong, Z. Yin, W. Zhang, Forming appearance control of arc striking and extinguishing area in multi-layer single-pass GMAW-based additive manufacturing, *Int. J. Adv. Manuf. Technol.* 87 (2016) 579–586. doi:10.1007/s00170-016-8543-2.
- [81] D. Ding, Z. Pan, D. Cuiuri, H. Li, N. Larkin, Adaptive path planning for wire-feed additive manufacturing using medial axis transformation, *J. Clean. Prod.* 133 (2016) 942–952. doi:10.1016/j.jclepro.2016.06.036.
- [82] J.N. Dupont, A.R. Marder, Thermal Efficiency of Arc Welding Processes, *Weld. Res. Suppl.* (1995) 406s–416s.
- [83] P.K. Ghosh, L. Dorn, S. Kulkarni, F. Hofmann, Arc characteristics and behaviour of metal transfer in pulsed current GMA welding of stainless steel, *J. Mater. Process. Technol.* 209 (2009) 1262–1274. doi:10.1016/j.jmatprotec.2008.03.049.
- [84] J. Ding, Thermo-mechanical Analysis of Wire and Arc Additive Manufacturing Process, 2012.
- [85] H. Geng, J. Li, J. Xiong, X. Lin, Optimisation of interpass temperature and heat input for wire and arc additive manufacturing 5A06 aluminium alloy, *Sci. Technol. Weld. Join.* 0 (2016) 1–12. doi:10.1080/13621718.2016.1259031.
- [86] M.P. Mughal, H. Fawad, R. a Mufti, M. Siddique, Deformation modelling in layered manufacturing of metallic parts using gas metal arc welding: effect of process parameters, *Model. Simul. Mater. Sci. Eng.* 13 (2005) 1187–1204. doi:10.1088/0965-0393/13/7/013.
- [87] H. Zhao, G. Zhang, Z. Yin, L. Wu, Effects of Interpass Idle Time on Thermal Stresses in Multipass Multilayer Weld-Based Rapid Prototyping, *J. Manuf. Sci. Eng.* 135 (2013) 11016. doi:10.1115/1.4023363.
- [88] E.R. Denlinger, P. Michaleris, Mitigation of distortion in large additive manufacturing parts, *Proc. Inst. Mech. Eng. Part B J. Eng. Manuf.* (2015) 1–11. doi:10.1177/0954405415578580.
- [89] H. Search, C. Journals, A. Contact, M. Iopscience, I.P. Address, Mechanical properties of Ti-6Al-4V specimens produced by shaped metal deposition, 15008 (n.d.). doi:10.1088/1468-6996/10/1/015008.
- [90] E. Brandl, B. Baufeld, C. Leyens, R. Gault, Additive manufactured Ti-6Al-4V using welding wire: Comparison of laser and arc beam deposition and evaluation with respect to aerospace material specifications, *Phys. Procedia.* 5 (2010) 595–606. doi:10.1016/j.phpro.2010.08.087.
- [91] X. Zhang, F. Martina, J. Ding, X. Wang, S.W. Williams, Fracture toughness and fatigue crack growth rate properties in wire + arc additive manufactured Ti-6Al-4V, *Fatigue Fract. Eng. Mater. Struct.* 40 (2017) 790–803. doi:10.1111/ffe.12547.
- [92] J.F. Wang, Q.J. Sun, H. Wang, J.P. Liu, J.C. Feng, Effect of location on microstructure and mechanical properties of additive layer manufactured Inconel 625 using gas tungsten arc welding, *Mater. Sci. Eng. A.* 676 (2016) 395–405. doi:10.1016/j.msea.2016.09.015.

- [93] T. Abe, H. Sasahara, Dissimilar metal deposition with a stainless steel and nickel-based alloy using wire and arc-based additive manufacturing, *Precis. Eng.* 45 (2016) 387–395. doi:10.1016/j.precisioneng.2016.03.016.
- [94] J. Xiong, G. Zhang, Z. Qiu, Y. Li, Vision-sensing and bead width control of a single-bead multi-layer part: Material and energy savings in GMAW-based rapid manufacturing, *J. Clean. Prod.* 41 (2013) 82–88. doi:10.1016/j.jclepro.2012.10.009.
- [95] C. Doumanidis, Y.M. Kwak, Multivariable adaptive control of the bead profile geometry in gas metal arc welding with thermal scanning, *Int. J. Press. Vessel. Pip.* 79 (2002) 251–262. doi:10.1016/S0308-0161(02)00024-8.
- [96] G. Saeed, Y.M. Zhang, Weld pool surface depth measurement using a calibrated camera and structured light, *Meas. Sci. Technol.* 18 (2007) 2570–2578. doi:10.1088/0957-0233/18/8/033.
- [97] Roland MDX-40 - Modela, (n.d.). http://www.engraving.com/machines/roland/Roland_MDX-40_Modela.htm (accessed October 13, 2017).
- [98] Benchtop CNC Mill | MDX-40A Specifications | Roland DGA, (n.d.). <https://www.rolanddga.com/products/3d/mdx-40a-benchtop-cnc-mill/specifications> (accessed October 13, 2017).
- [99] Project Name, (n.d.). <http://www.machsupport.com/> (accessed October 13, 2017).
- [100] A.R. Doodman Tipi, S.K.H. sani, N. Pariz, Improving the dynamic metal transfer model of gas metal arc welding (GMAW) process, *Int. J. Adv. Manuf. Technol.* 76 (2015) 657–668. doi:10.1007/s00170-014-6307-4.
- [101] J.. Lancaster, *The physics of welding*, 1984. doi:10.1088/0305-4624/15/2/I05.
- [102] Y. Wang, L. Wang, X. Lv, Simulation of Dynamic Behavior and Prediction of Optimal Welding Current for Short-Circuiting Transfer Mode in GMAW, *J. Manuf. Sci. Eng.* 138 (2016) 061011–061011. doi:10.1115/1.4032259.
- [103] Y. Zhang, Y. Chen, P. Li, A.T. Male, Weld deposition-based rapid prototyping: A preliminary study, *J. Mater. Process. Technol.* 135 (2003) 347–357. doi:10.1016/S0924-0136(02)00867-1.
- [104] M. Hermans, G. Den Ouden, Process behavior and stability in short circuit gas metal arc welding, *Weld. Journal-New York-*. (1999) 137–141. <https://app.aws.org/wj/supplement/Hermans/ARTICLE4.pdf> (accessed October 18, 2017).
- [105] L.-E. (Lars-E. Lindgren, *Computational welding mechanics : thermomechanical and microstructural simulations*, CRC Press, 2007. doi:10.1533/9781845693558.
- [106] M. Lin, T.W. Eagar, Influence of Arc Pressure on Weld Pool Geometry, *Weld. J.* (1985) 163–169.
- [107] H.G. Fan, R. Kovacevic, Droplet formation, detachment, and impingement on the molten pool in gas metal arc welding, *Metall. Mater. Trans. B.* 30 (1999) 791–801. doi:10.1007/s11663-999-0041-6.
- [108] J.H. Cho, S.J. Na, Three-dimensional analysis of molten pool in GMA-laser hybrid welding, *Weld. J.* 88 (2009) 35s–43s.
- [109] J. Hu, H.L. Tsai, Heat and mass transfer in gas metal arc welding. Part II: The metal, *Int. J. Heat Mass Transf.* 50 (2007) 808–820. doi:10.1016/j.ijheatmasstransfer.2006.08.026.
- [110] J. Ding, P. Colegrove, J. Mehnen, S. Ganguly, P.M.S. Almeida, F. Wang, S. Williams, Thermo-mechanical analysis of Wire and Arc Additive Layer Manufacturing process on large multi-layer parts, *Comput. Mater. Sci.* 50 (2011)

- 3315–3322. doi:10.1016/j.commat.2011.06.023.
- [111] Z.H. Rao, J. Zhou, H.L. Tsai, Determination of equilibrium wire-feed-speeds for stable gas metal arc welding, *Int. J. Heat Mass Transf.* 55 (2012) 6651–6664. doi:10.1016/j.ijheatmasstransfer.2012.06.074.
- [112] M. Chiumenti, M. Cervera, A. Salmi, C. Agelet de Saracibar, N. Dialami, K. Matsui, Finite element modeling of multi-pass welding and shaped metal deposition processes, *Comput. Methods Appl. Mech. Eng.* 199 (2010) 2343–2359. doi:10.1016/j.cma.2010.02.018.
- [113] J. Hu, H.L. Tsai, Heat and mass transfer in gas metal arc welding. Part I: The arc, *Int. J. Heat Mass Transf.* 50 (2007) 833–846. doi:10.1016/j.ijheatmasstransfer.2006.08.025.
- [114] P. Nie, O.A. Ojo, Z. Li, Modeling analysis of laser cladding of a nickel-based superalloy, *Surf. Coatings Technol.* 258 (2014) 1048–1059. doi:10.1016/j.surfcoat.2014.07.030.
- [115] M. Vogel, M. Khan, J. Ibara-medina, A. Pinkerton, N. N'Dri, M. Megahed, A coupled approach to weld pool, phase and residual stress modelling of laser direct metal deposition (LDMD) processes, in: *Proc. 2nd World Congr. Integr. Comput. Mater. Eng.*, Springer, 2013: pp. 231–236.
- [116] R. Martukanitz, P. Michaleris, T. Palmer, T. DebRoy, Z.K. Liu, R. Otis, T.W. Heo, L.Q. Chen, Toward an integrated computational system for describing the additive manufacturing process for metallic materials, *Addit. Manuf.* 1 (2014) 52–63. doi:10.1016/j.addma.2014.09.002.
- [117] F. Kreith, R.M. Manglik, M.S. Bohn, *Principles of Heat Transfer*, Cengage learning, Mason, OH, United States, 2010.
- [118] O.C. Zienkiewicz, R.L. Taylor, D. Fox, *The Finite Element Method for Solid and Structural Mechanics*, 2014. doi:10.1016/B978-1-85617-634-7.00007-7.
- [119] Q. Yang, P. Zhang, L. Cheng, Z. Min, M. Chyu, A.C. To, Finite element modeling and validation of thermomechanical behavior of Ti-6Al-4V in directed energy deposition additive manufacturing, *Addit. Manuf.* 12 (2016) 169–177. doi:10.1016/j.addma.2016.06.012.
- [120] X.K. Zhu, Y.J. Chao, Effects of temperature-dependent material properties on welding simulation, *Comput. Struct.* 80 (2002) 967–976. doi:10.1016/S0045-7949(02)00040-8.
- [121] J. Goldak, M. Bibby, J. Moore, R. House, B. Patel, Computer modeling of heat flow in welds, *Metall. Trans. B.* 17 (1986) 587–600. doi:10.1007/BF02670226.
- [122] P. Michaleris, Modeling metal deposition in heat transfer analyses of additive manufacturing processes, *Finite Elem. Anal. Des.* 86 (2014) 51–60. doi:10.1016/j.finel.2014.04.003.
- [123] J.O. Hallquist, *LS-DYNA® Keyword User's Manual: Volumes I, II, and III LSDYNA R7.1*, 2014.
- [124] P. Lindström, B. Josefson, M. Schill, T. Borrvall, Constitutive Modeling and Finite Element Simulation of Multi Pass Girth Welds, in: *Proc. NAFEMS Nord. Conf.*, Gothenburg, 2012: pp. 22–23.
- [125] M. Schill, E. Odenberger, Simulation of Residual Deformation from a Forming and Welding Process using LS-DYNA®, in: *13th Int. LS-DYNA Conf.*, Detroit, 2014: pp. 1–10.
- [126] EPRI, *Carbon Steel Handbook*, Palo Alto (CA), 2007. doi:1014670.
- [127] P. Michaleris, a Debicari, Prediction of welding distortion, *Weld. J.* Miami Fla. 76

- (1997) 172–s. doi:10.1016/j.jmatprotec.2007.10.009.
- [128] E.J. Soderstrom, K.M. Scott, P.F. Mendez, Calorimetric Measurement of Droplet Temperature in GMAW, *Weld. J.* 90 (2011) 77S–84S.
- [129] T. Kargul, E. Wielgosz, J. Falkus, Application of Thermal Analysis Tests Results in the Numerical Simulations of Continuous Casting Process, *Arch. Metall. Mater.* 60 (2015). doi:10.1515/amm-2015-0035.
- [130] T. Klöppel, T. Loose, Recent developments for thermo-mechanically coupled simulations in LS-DYNA with focus on welding processes, in: 10th Eur. LS-DYNA Conference, 2015.
- [131] E.R. Denlinger, P. Michaleris, Effect of stress relaxation on distortion in additive manufacturing process modeling, *Addit. Manuf.* 12 (2016) 51–59. doi:10.1016/j.addma.2016.06.011.
- [132] H. Zhao, G. Zhang, Z. Yin, L. Wu, Three-dimensional finite element analysis of thermal stress in single-pass multi-layer weld-based rapid prototyping, *J. Mater. Process. Technol.* 212 (2012) 276–285. doi:10.1016/j.jmatprotec.2011.09.012.
- [133] D. Rosenthal, The Theory of Moving Sources of Heat and Its Application to Metal Treatments.pdf, *Trans. ASME.* 68 (1946) 849–866.
- [134] V. Pavelic, R. Tanbakuchi, O.A. Uyehara, P.S. Myers, Experimental and computed temperature histories in gas tungsten-arc welding of thin plates, *WELD J.* 48 (1969) 295.
- [135] J. Goldak, A. Chakravarti, M. Bibby, A new finite element model for welding heat sources, *Metall. Trans. B.* 15 (1984) 299–305. doi:10.1007/BF02667333.
- [136] M. Hao, Y. Sun, A FEM model for simulating temperature field in coaxial laser cladding of Ti6AL4V alloy using an inverse modeling approach, *Int. J. Heat Mass Transf.* 64 (2013) 352–360. doi:10.1016/j.ijheatmasstransfer.2013.04.050.
- [137] A. Hussein, L. Hao, C. Yan, R. Everson, Finite element simulation of the temperature and stress fields in single layers built without-support in selective laser melting, *Mater. Des.* 52 (2013) 638–647. doi:10.1016/j.matdes.2013.05.070.
- [138] J. Ding, P. Colegrove, J. Mehnen, S. Williams, F. Wang, P.S. Almeida, A computationally efficient finite element model of wire and arc additive manufacture, *Int. J. Adv. Manuf. Technol.* 70 (2014) 227–236. doi:10.1007/s00170-013-5261-x.
- [139] J.Y. Shanghvi, P. Michaleris, Thermo-elasto-plastic finite element analysis of quasi-state processes in Eulerian reference frames, *Int. J. Numer. Methods Eng.* 53 (2002) 1533–1556. doi:10.1002/nme.345.
- [140] O.C. Zienkiewicz, R.L. Taylor, J.Z. Zhu, *The Finite Element Method: Its Basis and Fundamentals*, Sixth edition, Elsevier Butterworth-Heinemann, 2005.
- [141] L. Zhang, E.W. Reutzel, P. Michaleris, Finite element modeling discretization requirements for the laser forming process, *Int. J. Mech. Sci.* 46 (2004) 623–637. doi:10.1016/j.ijmecsci.2004.04.001.
- [142] E.R. Denlinger, J. Irwin, P. Michaleris, Thermomechanical Modeling of Additive Manufacturing Large Parts, *J. Manuf. Sci. Eng.* 136 (2014) 61007. doi:10.1115/1.4028669.
- [143] P. Michaleris, Modelling welding residual stress and distortion: current and future research trends, *Sci. Technol. Weld. Join.* 16 (2011) 363–368. doi:10.1179/1362171811Y.0000000017.
- [144] B. Schoinochoritis, D. Chantzis, K. Salonitis, Simulation of metallic powder bed additive manufacturing processes with the finite element method: A critical review, *Proc. Inst. Mech. Eng. Part B J. Eng. Manuf.* (2015).

- doi:10.1177/0954405414567522.
- [145] E.R. Denlinger, J.C. Heigel, P. Michaleris, Residual stress and distortion modeling of electron beam direct manufacturing, (2016). doi:10.1177/0954405414539494.
- [146] G. Zhao, C. Cho, J.-D. Kim, Application of 3-D finite element method using Lagrangian formulation to dilution control in laser cladding process, *Int. J. Mech. Sci.* 45 (2003) 777–796. doi:10.1016/S0020-7403(03)00140-1.
- [147] N. Grossi, F. Monteverchi, A. Scippa, G. Campatelli, 3D finite element modeling of holder-tool assembly for stability prediction in milling, in: *Procedia CIRP*, Elsevier, 2015: pp. 527–532. doi:10.1016/j.procir.2015.03.031.
- [148] V. Coskun, E. Ozkokdemir, B. Acar, Modelling of Heat Transfer across Bolted Joints in Abaqus / CAE, in: *SIMULIA Community Conf.*, 2015: pp. 1–11.
- [149] X. Bai, H. Zhang, G. Wang, Improving prediction accuracy of thermal analysis for weld-based additive manufacturing by calibrating input parameters using IR imaging, *Int. J. Adv. Manuf. Technol.* 69 (2013) 1087–1095. doi:10.1007/s00170-013-5102-y.
- [150] H. Zhao, G. Zhang, Z. Yin, L. Wu, A 3D dynamic analysis of thermal behavior during single-pass multi-layer weld-based rapid prototyping, *J. Mater. Process. Technol.* 211 (2011) 488–495. doi:10.1016/j.jmatprotec.2010.11.002.
- [151] Y. Ma, D. Cuiuri, C. Shen, H. Li, Z. Pan, Effect of interpass temperature on in-situ alloying and additive manufacturing of titanium aluminides using gas tungsten arc welding, *Addit. Manuf.* 8 (2015) 71–77. doi:10.1016/j.addma.2015.08.001.
- [152] J.D. Spencer, P.M. Dickens, C.M. Wykes, Rapid prototyping of metal parts by three-dimensional welding, *Proc. Inst. Mech. Eng. Part B J. Eng. Manuf.* 212 (1998) 175–182. doi:10.1243/0954405981515590.
- [153] M. Liberini, A. Astarita, G. Campatelli, A. Scippa, F. Monteverchi, G. Venturini, M. Durante, L. Boccarusso, F.M.C. Minutolo, A. Squillace, Selection of Optimal Process Parameters for Wire Arc Additive Manufacturing, in: *Procedia CIRP*, 2017. doi:10.1016/j.procir.2016.06.124.
- [154] H. Takagi, T. Abe, P. Cui, H. Sasahara, Mechanical properties evaluation of metal components repaired by direct metal lamination, *Key Eng. Mater.* 656–657 (2015) 440–445. doi:10.4028/www.scientific.net/KEM.656-657.440.
- [155] T. Abe, M. Katagiri, H. Sasahara, Accurate fabrication by improvement of lamination path on direct metal lamination using arc discharge, *Proc. - ASPE 2012 Annu. Meet.* 54 (2012) 269–299.
- [156] D. Babic, D.B. Murray, A.A. Torrance, Mist jet cooling of grinding processes, *Int. J. Mach. Tools Manuf.* 45 (2005) 1171–1177. doi:10.1016/j.ijmachtools.2004.12.004.
- [157] B. Yalçın, A.E. Özgür, M. Koru, The effects of various cooling strategies on surface roughness and tool wear during soft materials milling, 2009. doi:10.1016/j.matdes.2008.05.037.
- [158] N. Zuckerman, N. Lior, Jet impingement heat transfer: Physics, correlations, and numerical modeling, *Adv. Heat Transf.* 39 (2006) 565–631. doi:10.1016/S0065-2717(06)39006-5.
- [159] T.S. O'Donovan, D.B. Murray, Jet impingement heat transfer - Part I: Mean and root-mean-square heat transfer and velocity distributions, *Int. J. Heat Mass Transf.* 50 (2007) 3291–3301. doi:10.1016/j.ijheatmasstransfer.2007.01.044.
- [160] R.J. Goldstein, M.E. Franchett, Heat Transfer From a Flat Surface to an Oblique Impinging Jet, *J. Heat Transfer.* 110 (1988) 84. doi:10.1115/1.3250477.
- [161] R.J. Goldstein, K. a. Sobolik, W.S. Seol, Effect of Entrainment on the Heat Transfer

- to a Heated Circular Air Jet Impinging on a Flat Surface, *J. Heat Transfer*. 112 (1990) 608. doi:10.1115/1.2910430.
- [162] R.J. Goldstein, A.I. Behbahani, K.K. Heppelmann, Streamwise distribution of the recovery factor and the local heat transfer coefficient to an impinging circular air jet, *Int. J. Heat Mass Transf.* 29 (1986) 1227–1235. doi:10.1016/0017-9310(86)90155-9.
- [163] B.R. Hollworth, S.I. Wilson, Entrapment effects on impingement heat transfer: Part I — Measurements of heated jet velocity and temperature distributions and recovery temperatures on target surface, *J. Heat Transfer*. 106 (1984) 797–803.
- [164] M. Masoomi, S.M. Thompson, N. Shamsaei, Laser powder bed fusion of Ti-6Al-4V parts: Thermal modeling and mechanical implications, *Int. J. Mach. Tools Manuf.* 118–119 (2017) 73–90. doi:10.1016/j.ijmactools.2017.04.007.
- [165] I.A. Choudhury, M.A. El-Baradie, Machinability assessment of inconel 718 by factorial design of experiment coupled with response surface methodology, (n.d.). https://ac.els-cdn.com/S0924013699000850/1-s2.0-S0924013699000850-main.pdf?_tid=c4de4fe6-be2e-11e7-b8f4-00000aacb35e&acdnat=1509449554_73fe73dab0ea4ea1ac937d6900a9c425 (accessed October 31, 2017).
- [166] B.M. Kramer, P.D. Hartung, Theoretical considerations in the machining of nickel-based alloys, *Cut. Tool Mater.* (1980) 57–74.
- [167] A. Bordin, A. Ghiotti, S. Bruschi, L. Facchini, F. Bucciotti, Machinability Characteristics of Wrought and EBM CoCrMo Alloys, *Procedia CIRP*. 14 (2014) 89–94. doi:10.1016/j.procir.2014.03.082.
- [168] A. Bordin, S. Bruschi, A. Ghiotti, P.F. Bariani, Analysis of tool wear in cryogenic machining of additive manufactured Ti6Al4V alloy, (2015). doi:10.1016/j.wear.2015.01.030.
- [169] N. Grossi, L. Sallese, A. Scippa, G. Campatelli, Speed-varying cutting force coefficient identification in milling, *Precis. Eng.* 42 (2015) 321–334. doi:10.1016/j.precisioneng.2015.04.006.
- [170] A. Scippa, N. Grossi, G. Campatelli, Milled surface generation model for chip thickness detection in peripheral milling, in: *Procedia CIRP*, Elsevier, 2013: pp. 450–455. doi:10.1016/j.procir.2013.06.132.
- [171] A. Scippa, N. Grossi, G. Campatelli, FEM based cutting velocity selection for thin walled part machining, in: *Procedia CIRP*, Elsevier, 2014: pp. 287–292. doi:10.1016/j.procir.2014.03.023.
- [172] Y. Altintas, S. Engin, Generalized modeling of mechanics and dynamics of milling cutters, *CIRP Ann. Technol.* 50 (2001) 25–30.
- [173] P. Farahmand, P. Balu, F. Kong, R. Kovacevic, Investigation of Thermal Cycle and Hardness Distribution in the Laser Cladding of AISI H13 tool steel produced by a High Power Direct Diode Laser, in: *Proc. ASME 2013 Int. Mech. Eng. Congr. Expo.*, ASME, 2015: pp. 1–12. doi:10.1115/IMECE2013-62193.
- [174] N. Grossi, A. Scippa, L. Sallese, R. Sato, G. Campatelli, Spindle speed ramp-up test: A novel experimental approach for chatter stability detection, *Int. J. Mach. Tools Manuf.* 89 (2015) 221–230. doi:10.1016/j.ijmactools.2014.11.013.
- [175] A. Scippa, L. Sallese, N. Grossi, G. Campatelli, Improved dynamic compensation for accurate cutting force measurements in milling applications, (2014). doi:10.1016/j.ymsp.2014.08.019.
- [176] J.P. Davim, *Machining of Complex Sculptured Surfaces*, (2012). doi:10.1007/978-1-4471-2356-9.

- [177] G. Quintana, J. Ciurana, Chatter in machining processes: A review, *Int. J. Mach. Tools Manuf.* 51 (2011) 363–376. doi:<http://dx.doi.org/10.1016/j.ijmachtools.2011.01.001>.
- [178] H. Ning, W. Zhigang, J. Chengyu, Z. Bing, Finite element method analysis and control stratagem for machining deformation of thin-walled components, *J. Mater. Process. Technol.* 139 (2003) 332–336. doi:[10.1016/S0924-0136\(03\)00550-8](https://doi.org/10.1016/S0924-0136(03)00550-8).
- [179] V. Thevenot, L. Arnaud, G. Desein, G. Cazenave–Larroche, Influence of Material Removal on the Dynamic Behavior of Thin-Walled Structures in Peripheral Milling, *Mach. Sci. Technol.* 10 (2006) 275–287. doi:[10.1080/10910340600902082](https://doi.org/10.1080/10910340600902082).
- [180] S. Bolsunovskiy, V. Vermel, G. Gubanov, I. Kacharava, A. Kudryashov, Thin-walled part machining process parameters optimization based on finite-element modeling of workpiece vibrations, in: *Procedia CIRP*, 2013: pp. 276–280. doi:[10.1016/j.procir.2013.06.102](https://doi.org/10.1016/j.procir.2013.06.102).
- [181] S. Seguy, F.J. Campa, L.N.L. de Lacalle, L. Arnaud, G. Desein, G. Aramendi, Toolpath dependent stability lobes for the milling of thin-walled parts, *Int. J. Mach. Mach. Mater.* 4 (2008) 377. doi:[10.1504/IJMMM.2008.023720](https://doi.org/10.1504/IJMMM.2008.023720).
- [182] O. Tuysuz, Y. Altintas, Frequency Domain Prediction of Varying Thin-Walled Workpiece Dynamics in Machining, *J. Manuf. Sci. Eng.* 139 (2017) 1–16. doi:[10.1115/1.4036124](https://doi.org/10.1115/1.4036124).
- [183] L. Arnaud, O. Gonzalo, S. Seguy, H. Jauregi, G. Peigné, Simulation of low rigidity part machining applied to thin-walled structures, *Int. J. Adv. Manuf. Technol.* 54 (2011) 479–488. doi:[10.1007/s00170-010-2976-9](https://doi.org/10.1007/s00170-010-2976-9).
- [184] F. Montevecchi, N. Grossi, H. Takagi, A. Scippa, H. Sasahara, G. Campatelli, Cutting Forces Analysis in Additive Manufactured AISI H13 Alloy, in: *Procedia CIRP*, 2016: pp. 476–479. doi:[10.1016/j.procir.2016.04.034](https://doi.org/10.1016/j.procir.2016.04.034).
- [185] F. Montevecchi, N. Grossi, A. Scippa, G. Campatelli, Improved RCSA technique for efficient tool-tip dynamics prediction, *Precis. Eng.* 44 (2016). doi:[10.1016/j.precisioneng.2015.11.004](https://doi.org/10.1016/j.precisioneng.2015.11.004).
- [186] T. Davis, K. Sigmon, *MATLAB Primer*, Seventh Edition, 2004. doi:[10.1201/9781420034950](https://doi.org/10.1201/9781420034950).
- [187] F. Montevecchi, A. Scippa, N. Grossi, G. Campatelli, Thin Walled Machining Optimization for Additive Manufactured Components, in: *Proc. MTTRF 2017 Annu. Meet.*, 2017.